

Multi-Wavelength Imaging of Cortical Activity  
Patterns in V1 of Alert Monkeys

Yevgeniy Borisovich Sirotin

Submitted in partial fulfillment of the  
requirements for the degree  
of Doctor of Philosophy  
in the Graduate School of Arts and Sciences

COLUMBIA UNIVERSITY

2008

© 2008

Yevgeniy Borisovich Sirotin

All Rights Reserved

## ABSTRACT

### Multi-Wavelength Imaging of Cortical Activity Patterns in V1 of Alert Monkeys

Yevgeniy Borisovich Sirotin

Optical imaging of intrinsic signals in alert animals can provide unprecedented insight into cortical function for issues of both neurovascular coupling and neuronal processing. However, few studies to date have used this technique and it remains poorly understood. In the course of studies, carried out together with my advisor Aniruddha Das, we have implemented a method for spectroscopic optical imaging in alert macaques and used it to investigate the function of the primary visual cortex (V1).

Spectroscopic optical imaging consists of separately recording optical signals corresponding to blood volume (total hemoglobin; HbT) and oxygenation (oxyhemoglobin, HbO; deoxyhemoglobin, HbR) and relating changes in these signals to underlying neuronal activity. This thesis reveals that these signals can be decomposed into two components: those specific to stimulus properties versus those related to trial structure. The stimulus-related HbT signals, which are not used extensively in functional research, are shown to have many advantages over the HbR signals, including higher signal to noise (SNR) and

ease of interpretation. A linear relationship between stimulus evoked HbT and neuronal activity in the alert animal is demonstrated, showing that it is a good functional signal.

The finding of large trial-related signals was unexpected and novel. These hemodynamic signals are comparable in amplitude to stimulus driven activity, but unrelated to neuronal spiking and appear timed to deliver fresh arterial blood to cortex in anticipation of task onsets. Surprisingly, classical neurovascular relationships that hold for stimulus-related hemodynamics, cannot explain the ongoing trial-related dynamics. The implications of this finding to the processing and interpretation of hemodynamic signals are discussed.

In the final section of this thesis, the stimulus-related HbT signal is used as a proxy for neuronal activity to demonstrate population level interactions in V1 tuned for stimulus geometry. There is a considerable body of evidence that suggests that contour extraction may start at the level of V1. Psychophysical investigations and theoretical models suggest that elements are grouped according to a set of orientation tuned co-axially elongated interaction fields between elements implemented at the level of cortical circuitry. However, these have not been functionally demonstrated. Investigations herein demonstrate that short ( $0.25^\circ$ ) line elements have co-axially elongated and orientation tuned

interaction fields over the retinotopic map of V1, which have been posited on theoretical grounds. Further, responses to groups of line elements sum nonlinearly according to the geometry of their configuration, corresponding well to Gestalt notions of contour grouping and the subjects' perception.

# TABLE OF CONTENTS

<b>CHAPTER 1.</b>	<b>1</b>
1.1. PERCEPTION FROM PATTERNS OF ACTIVITY ACROSS CORTEX?	1
1.2. OPTICAL IMAGING AS A MEASURE OF NETWORK ACTIVITY.	2
1.3. THE SCOPE OF THIS THESIS	3
<b>CHAPTER 2.</b>	<b>6</b>
2.1. SEARCHING FOR A MARKER OF SPATIAL PATTERNS OF NEURONAL ACTIVITY	6
2.1.1. <i>The Development of Optical Imaging as a Tool in Neurobiology</i>	6
2.1.2. <i>BOLD: An Unambiguous Marker of Neuronal Activity?</i>	8
2.1.3. <i>Developing Blood Volume as a Spatial Marker of Metabolic Demand</i>	14
2.1.4. <i>Remote Sources of Vascular Signals</i>	15
2.1.5. <i>Blood Volume vs. Spiking</i>	16
2.1.6. <i>Prior Work Using Optical Imaging</i>	18
2.2. RESULTS FROM SIMULTANEOUS OPTICAL IMAGING OF INTRINSIC SIGNALS AT TWO WAVELENGTHS AND ELECTROPHYSIOLOGY IN ALERT BEHAVING MONKEYS:	20
2.2.1. <i>Vascular Contributions to the Initial Dip</i>	20
2.2.2. <i>Oxygenation signals feature clear and opposite contributions from arteriolar and venous compartments</i>	24
2.2.3. <i>Changes in Blood Volume have Better Signal to Noise and Spatial Precision than the hyper-oxygenation rebound</i>	27
2.2.4. <i>Linear Temporal Summation of HbT Responses</i>	40
2.2.5. <i>Changes in HbT are a Linear Function of Neuronal Activity in the Fixating Animal</i>	42
2.3. DISCUSSION:	45
2.3.1. <i>Blood volume is a robust, spatially precise, and tuned indicator of neuronal activity.</i>	45
2.3.2. <i>The spatial extent of the pointspreads measured across imaging wavelengths do not differ.</i>	45
2.3.3. <i>Blood volume likely contributes to the optically measured initial dip.</i>	46
2.3.4. <i>Blood Volume Likely Accounts for the Post-Stimulus Undershoot</i>	48
2.3.5. <i>The Push-Pull Nature of the Initial Dip</i>	48
2.3.6. <i>Distinguishing Stimulus-triggered from Trial-related signals</i>	49
2.4. METHODS	51
2.4.1. <i>Optical imaging: Surgery, recording chambers, artificial dura:</i>	51
2.4.2. <i>Optical imaging: Data acquisition</i>	51
2.4.3. <i>Optical Imaging: General Data Analysis Steps</i>	52
2.4.4. <i>Optical Imaging: Regression Analysis of Response Timecourse</i>	53
2.4.5. <i>Electrophysiology: Hardware, electronics and analysis:</i>	54
2.4.6. <i>Electrophysiology: Data processing:</i>	55
2.4.7. <i>Electrophysiology: Fitting to Haemodynamics:</i>	55
2.4.8. <i>Stimuli</i>	56
3.1. INTRODUCTION TO THE CHAPTER	58
3.2. UNEXPECTED DISCOVERY OF TRIAL-LINKED ANTICIPATORY SIGNALS IN V1	59
3.2.1. <i>V1 responds to periodic fixation task in the dark.</i>	64
3.2.2. <i>Dark room signals are not predicted by local neuronal activity in V1.</i>	65
3.2.3. <i>V1 signal reflects trial-locked arterial dilation.</i>	69
3.2.4. <i>Predictive timing anticipates trial onsets; amplitude correlates with trial performance.</i>	75
3.2.5. <i>General autonomic response vs. specific V1 arterial rhythm</i>	81
3.3. DISCUSSION	84
3.3.1. <i>Comparison with fMRI Studies of Anticipatory Signals</i>	86

3.3.2. <i>Comparison with Other Anticipatory Signals</i>	87
3.3.3. <i>Sources of Anticipatory Timing in V1</i>	88
3.3.4. <i>Possible Mechanisms Underlying Preparatory Hemodynamic Signals</i>	89
3.3.5. <i>Functional Implications of Anticipatory Hemodynamics in Cortex</i>	90
3.4. METHODS:	91
3.4.1. <i>Summary:</i>	91
3.4.2. <i>Tasks: Visual fixation:</i>	92
3.4.3. <i>Tasks: Auditory control:</i>	93
3.4.4. <i>Optical imaging: Surgery, recording chambers, artificial dura:</i>	93
3.4.5. <i>Optical imaging: Hardware, electronics and imaging routines:</i>	94
3.4.6. <i>Optical imaging: Image processing:</i>	95
3.4.7. <i>Electrophysiology: Hardware, electronics and analysis:</i>	98
3.4.8. <i>Electrophysiology: Data processing:</i>	99
3.4.9. <i>Electrophysiology: Fitting to Haemodynamics:</i>	99
3.4.10. <i>Additional Figures:</i>	101
<b>CHAPTER 4.</b>	<b>116</b>
4.1. INTRODUCTION TO THE CHAPTER	116
4.2. THE ANATOMY AND PHYSIOLOGY OF V1 THAT LIKELY UNDERLIE CONTOUR GROUPING	117
4.2.1. <i>Psychophysical Investigations of Contour Grouping</i>	117
4.2.2. <i>The Architecture of V1 is Consistent with a Role in Contour Grouping</i>	118
4.2.3. <i>Physiology of V1 and Perception</i>	119
4.3. EXPERIMENTAL EVIDENCE FOR COLLINEAR INTERACTIONS AND FILL-IN BETWEEN ORIENTED LINES IN PRIMARY VISUAL CORTEX	120
4.3.1. <i>Psychophysics of collinear grouping is similar between monkeys and humans</i>	120
4.3.2. <i>Responses to isolated short lines are elongated collinearly</i>	124
4.3.3. <i>Nonlinear interactions between lines are tuned for smooth contours</i>	130
4.3.4. <i>Collinear interactions are chained along elongated contours</i>	134
4.4. DISCUSSION:	137
4.5. ADDITIONAL FIGURES:	141
4.6. METHODS	144
4.6.1. <i>Psychophysics</i>	144
4.6.2. <i>Stimuli (for both psychophysics and optical imaging)</i>	145
4.6.3. <i>Optical imaging: tasks:</i>	146
4.6.4. <i>Optical imaging: Surgery, recording chambers, artificial dura:</i>	146
4.6.5. <i>Optical imaging: Data acquisition</i>	147
4.6.6. <i>Optical Imaging: General Data Analysis Steps</i>	147
<b>CHAPTER 5.</b>	<b>151</b>
5.1. THE SCIENTIFIC CONTRIBUTIONS OF THIS THESIS	151
5.2. FUTURE DIRECTIONS	154
<b>APPENDIX I.</b>	<b>159</b>
A. THE PHYSICS OF MEASURING INTRINSIC SIGNALS	159
B. ILLUMINATING THE CORTEX HOMOGENEOUSLY	160
C. IMPORTANT DETAILS OF ILLUMINATOR DESIGN	162
<b>APPENDIX II.</b>	<b>164</b>
A. THE THREADS AND THEIR FUNCTIONALITY	165
1. <i>Main Thread – I/O, Timing</i>	165
2. <i>Experiment Thread – Experiment Specifics (Object Based)</i>	167
3. <i>GUI Thread – User Interface, Stimulus Presentation and Configuration, Manual Controls, Data Recording</i>	168

B. BEHAVCTRL OBJECTS	171
C. C++ WRAPPERS FOR VSG GRAPHICS OBJECTS	172
1. CVSG	172
2. <i>VsgScene</i>	173
3. <i>VsgObject</i>	174
<b>BIBLIOGRAPHY</b>	<b>176</b>

## LIST OF FIGURES

FIGURE 2.1. THE INITIAL DIP IS NOT SOLELY A MEASURE OF DEOXYHEMOGLOBIN.	22
FIGURE 2.2. THE EVOLUTION OF HEMODYNAMIC RESPONSES AT 605 AND 530 NM HIGHLIGHTS THE ROLE OF DIFFERENT VASCULAR COMPARTMENTS IN GENERATING THE OXYGENATION RESPONSE.	27
FIGURE 2.3. BLOOD VOLUME SIGNALS HAVE A HIGHER STIMULUS DRIVEN VARIANCE THAN OXYGENATION SIGNALS.	29
FIGURE 2.4. THE BLOOD VOLUME POINTSPREAD HAS A SIMILAR SPATIAL PROFILE AS THE INITIAL DIP, BUT IS NARROWER THAN THE HYPEROXYGENATION REBOUND.	31
FIGURE 2.5. THE HEMODYNAMIC POINT-SPREAD AT 530 NM IS ELONGATED ACROSS OCULAR DOMINANCE COLUMNS.	33
FIGURE 2.6. BLOOD VOLUME IS A BETTER SPATIAL MARKER OF NEURONAL ACTIVITY THAN THE HYPEROXYGENATION REBOUND.	35
FIGURE 2.7. THE BLOOD VOLUME SIGNAL SHOWS MORE ROBUST ORIENTATION TUNING THAN OXYMETRIC SIGNALS.	37
FIGURE 2.8. BLOOD VOLUME RESPONSES SHOW HIGH SPATIAL SPECIFICITY AND MONO-PHASIC TIME-COURSE.	39
FIGURE 2.9. CHANGES IN BLOOD VOLUME SUMMATE LINEARLY IN TIME.	42
FIGURE 2.10. STIMULUS-DRIVEN BLOOD VOLUME RESPONSES ARE LINEARLY RELATED TO UNDERLYING NEURONAL FIRING.	44
FIGURE 3.1. PERIODIC TRIALS EVOKE STIMULUS-INDEPENDENT, TRIAL-LINKED SIGNALS EVEN IN THE DARK.	61
FIGURE 3.2. TRIAL-LINKED SIGNALS IN DARK ROOM, UNLIKE VISUALLY EVOKED SIGNALS, ARE NOT PREDICTED BY LOCAL NEURONAL ACTIVITY.	67
FIGURE 3.3. OPTICAL IMAGES REVEAL TRIAL-LOCKED ARTERIAL CYCLE BRINGING FRESH BLOOD TO CORTEX BEFORE EACH TRIAL ONSET.	71
FIGURE 3.4. TRIAL-RELATED SIGNALS ARE GLOBAL OVER V1, UNLIKE STIMULUS-EVOKED SIGNALS.	73
FIGURE 3.5. TRIAL-RELATED SIGNAL ENTRAINs TO ANTICIPATED TRIAL ONSETS.	77
FIGURE 3.6. ARTERIAL CYCLE STRETCHES TO FIT TRIAL PERIOD, WITH MAXIMUM DILATION SHORTLY BEFORE ANTICIPATED ONSET OF NEXT TRIAL.	80
FIGURE 3.7. PERIODIC AUDITORY TASK ALSO ENTRAINs HÆMODYNAMIC SIGNALS IN V1 BUT WITHOUT ANY ARTERIAL CONTRACTION-DILATION CYCLE.	83
FIGURE 3.8. REPRESENTATIVE SET OF TRIAL DATA FROM MONKEY 'V' SHOWING BROAD SIMILARITY TO THE DATA FROM MONKEY 'S'.	101
FIGURE 3.9. REPRESENTATIVE SET OF IMAGES FROM MONKEY 'V' SHOWING ANTICIPATORY ARTERIAL CONTRACTION-DILATION CYCLE AS IN MONKEY 'S':	102
FIGURE 3.10. THE DAY-TO-DAY VARIATION (PARTICULARLY, LOW RECORDED AMPLITUDES) OF THE 530 NM SIGNAL IS LIKELY AN ARTIFACT OF DAY-TO-DAY VARIABILITY IN DEGREE OF SCATTER IN THE RECORDING CHAMBER MEDIUM (AGAR + ARTIFICIAL CSF).	103
FIGURE 3.11. SUPPLEMENTARY FIGURES ON ELECTRODE RECORDING.	104
FIGURE 3.12. BRIGHTENING / DARKENING ARTERY WALLS IMPLY ARTERIAL CONTRACTION / DILATION.	105
FIGURE 3.13. CORTICAL SIGNAL DOES NOT SYNCHRONIZE WITH ACQUIRING FIXATION AT THE START OF THE TRIAL:	107
FIGURE 3.14. CORTICAL SIGNAL DOES NOT SYNCHRONIZE WITH BREAKING FIXATION AT TRIAL END.	108
FIGURE 3.15. SIGNAL PERIODICITY IS NOT TRIGGERED BY THE FLASH OF INCREASED LIGHT INPUT ON PUPIL DILATION.	109
FIGURE 3.16. CORTICAL SIGNALS ARE INDEPENDENT OF THE BRIGHTNESS OF THE TRIAL ONSET CUE:	110

FIGURE 3.17. PERIODICITY OF TRIAL-TRIGGERED SIGNAL IS NOT DUE TO THE ACCIDENTAL ENTRAINMENT OF A TRIAL-INDEPENDENT INTRINSIC PERIODICITY.	111
FIGURE 3.18. TRIAL-RELATED V1 SIGNAL IS NOT TRIGGERED BY SIMPLY GIVING REGULAR JUICE OUTSIDE THE CONTEXT OF THE FIXATION TASK.	112
FIGURE 3.19. POWER SPECTRA.	113
FIGURE 3.20. CORTICAL SIGNAL AMPLITUDE CORRELATES WITH PERFORMANCE ON FIXATION TASK.	114
FIGURE 3.21. CORTICAL SIGNAL AND BEHAVIOURAL RESPONSE IN EXPERIMENT WHERE MONKEY S FIRST LEARNED THE TASK.	115
FIGURE 4.1. CONTOUR GROUPING IS SIMILAR FOR MONKEYS AND HUMANS.	122
FIGURE 4.2. SPATIAL EXTENT AND TIME COURSE OF THE CORTICAL POINTSPREAD (PS) IN V1.	126
FIGURE 4.3. POINTSPREADS OF SHORT SINGLE LINES SHOW ORIENTATION-TUNED COAXIAL MODULATION.	129
FIGURE 4.4. NONLINEAR INTERACTIONS BETWEEN ORIENTED LINES ARE TUNED FOR COLLINEAR CONFIGURATIONS.	131
FIGURE 4.5. NONLINEAR INTERACTIONS ARE TUNED TO NEARBY FLANK SEPARATIONS.	133
FIGURE 4.6. COLLINEAR INTERACTIONS ARE CHAINED ALONG SMOOTH CONTOURS.	136
FIGURE 4.7. THE POINTSPREAD TO A LINE SEGMENT SHOWS FINE RETINOTOPIC SHIFTS ON CORTEX.	141
FIGURE 4.8. POINTSPREADS ARE ELONGATED ORTHOGONAL TO LOCAL OCULAR DOMINANCE COLUMNS, INDEPENDENT OF LINE ORIENTATION, REFLECTING LOCAL ANISOTROPY IN CORTICAL MAGNIFICATION.	141
FIGURE 4.9. CO-AXIAL DIFFERENCES BETWEEN BARS ARE AN ORDER OF MAGNITUDE LARGER THAN ANY EXPECTED RETINOTOPIC DIFFERENCES.	142
FIGURE 4.10. ASYNCHRONOUS PRESENTATION DRAMATICALLY REDUCES THE INTERACTION BETWEEN LINES.	143
FIGURE 4.11. BAR INTERACTIONS ARE INVARIANT ACROSS CONTRAST.	144
FIGURE I.1: LED CIRCUIT FOR REAL-TIME SPECTROSCOPY AND STROBING	161

## ACKNOWLEDGMENTS

I would like to thank wholeheartedly all those that made this work possible either by direct contribution or by supporting me during my PhD.

First, none of this work would have been possible without the kind guiding hands of my advisor Dr. Aniruddha Das. Over the years he has been both a teacher and a friend to me and I could not wish for a better mentor. I would also like to thank him for the incredibly tasty Indian food that he has prepared for me on many occasions.

I would like to thank all of the people that were or are part of the Das lab and whom I consider my friends. Firstly, I would like to thank Karl Korinek for building and designing much of the equipment used in this thesis and for his humor and camaraderie. I would like to thank Gina Cantone helped perform many experiments and helped keep the world in order even when everything was wrong.

I also would like to thank the excellent high school and undergraduate students that have contributed to the lab during this thesis: Calvin Ma, Justine Ordinario, Soo Ryum Yang, and Elio Santos.

I would like to thank all of my classmates and coworkers with whom we have shared many celebrations and who have made it a pleasure to pursue my work.

I would like to thank my parents: Boris and Bertalina Sirotin. They brought me into this world and taught me how to live, how to love, and how to work. Throughout my life, they helped me find balance and provided me a center from which to measure all things.

I would also like to thank the rest of my family, especially my sister Marina Sun, who helped put my experiences in perspective.

Most of all, I would like to thank my wife Georgia Gleason, who has provided me with love, encouraged me during the low times, and shared my joy during the high times. I am lucky to have her in my life.

## Chapter 1.

### INTRODUCTION

#### *1.1. Perception from Patterns of Activity across Cortex?*

A major challenge in Neuroscience is to be able to understand how interactions between neural populations in primate sensory cortex give rise to complex perception. Much of our current understanding of sensory processing comes from the study of the visual system. Neuronal responses at different levels in this system show varying degrees of selectivity and complexity. A cell in V1, for example, may respond to any stimulus that shows a particular orientation and spatial frequency, whereas a cell in inferotemporal cortex may fire only in response to faces and not to any other similar non-face object. It is believed that the cortex gradually builds up the complicated stimulus preferences observed at the highest levels, from nonlinear interactions within and between visual areas, but the process is poorly understood.

As early as V1<sup>1</sup>[1], cells demonstrate nonlinear stimulus selectivity which has been implicated as a possible mechanism for the beginning stages of form perception: the extraction of smooth contours and object boundaries. Functional

---

<sup>1</sup> Early here relates to the nominal cortical hierarchy with V1 being the first cortical recipient of visual signals from the LGN.

properties of neurons in V1 are arranged so as to form several overlapping columnar maps of visual properties along its surface (retinotopy, orientation, ocular dominance, etc.). However, even simple visual stimuli, such as short lines or contours, activate many neurons over the extent of V1 which interact according to their underlying anatomical connectivity, and different stimuli may selectively recruit different networks. Classical electrophysiological approaches give a poor picture of such interactions because they rely on point-wise sampling of neuronal activity and are thus limited in what they may say about the recruited network. Further, though many investigations to date have used anesthetized preparations of several species to study the first-order properties of cells in V1, interactions related to form perception may be altered by the anesthetic. Thus, in order to understand the networks involved in processing even simple perceptual forms it is necessary to record simultaneously across extended regions of V1 of behaving animals.

### *1.2. Optical Imaging as a Measure of Network Activity.*

There are several candidate techniques for visualizing activity of extended neural populations, each with a specific spatiotemporal window [2]. Because stimulus-related activity may spread over several millimeters of V1 (via horizontal connections), but with spatial structure at a scale of hundreds of micrometers (orientation columns), only two techniques provide a reasonable fit: optical

imaging of intrinsic signals (OIS) and imaging of voltage sensitive dyes (VSD). Though VSD imaging offers millisecond temporal resolution, the dyes are still toxic and this limits the duration of the experiments and the lifetime of the preparation. Thus, OIS is the most practical technique for measuring population activity under normal physiological conditions.

Unlike electrophysiological techniques, intrinsic signal imaging is not a direct measure of neural activity, and instead typically measures hemodynamic changes that correlate with neuronal metabolic demand. While the technique has been widely used in anesthetized preparations, few studies have been undertaken to characterize these signals in the alert state. Thus, before using this method to make inferences about neuronal activity, it is first necessary to determine which components of the signals relate directly to stimulus-driven neuronal activity and which may have other origins.

### *1.3. The Scope of this Thesis*

The motivation behind this study – as indicated at the start of this chapter – is to study population level activity in V1 associated with form perception. This thesis describes a novel imaging system for spectroscopic optical imaging in alert behaving macaque monkeys. This system is then used to address two outstanding scientific issues: first, the origins of hemodynamic signals in V1 and

their relationship with neuronal activity; and next, how neural populations across V1 interact in grouping oriented line elements into contours, the first stage of form perception.

Chapter 2 discusses the nature of the metabolic markers of neuronal activity used in optical imaging and establishes the blood volume signal as a valid marker of the spatial patterns of neuronal activity with several advantages over the more commonly used blood oxygen level dependent signals.

The ultimate goal is to have a linear measure of stimulus-related neuronal activity and to be able to discount contributions from other sources. Thus, Chapter 3 characterizes baseline hemodynamic activity in V1 during basic behavioral tasks, across modalities, and in both the presence and absence of visual input. Surprisingly, we found the presence of task structure-related signals in V1 that are separable from those due to direct neural firing though comparable in magnitude. These signals likely reflect part of the subjects' physiological preparation for upcoming tasks which appears to direct resources to cortical areas likely involved in task performance. Uncorrected for, these signals would have produced interpretational errors about any underlying neuronal activation.

Having established the appropriate methods, Chapter 4 investigates how networks of neurons with identified tuning in V1 respond to individual line elements and whether the properties of these network responses can increase our understanding of the computations underlying visual processing. As previously mentioned, V1 has been implicated in the process of contour extraction: a fundamental step in object recognition. Experiments described in this chapter show that responses to small oriented line elements produce co-axially elongated cortical activity patterns that agree remarkably well with patterns of cortical activity predicted on psychophysical grounds and form the basis of many models of contour extraction. Responses to multiple, simultaneously presented, line elements sum nonlinearly. This nonlinearity, taken as an index of interaction, is greatest for elements positioned along smooth contours. Part of the interaction results from mutual suppression, but intriguingly, some can be explained by a 'fill-in' of activity between collinear elements which chains along elongated contours, suggesting an active process of contour completion operating in V1.

## Chapter 2.

### EVALUATION OF BLOOD VOLUME AS A MARKER OF SPATIAL NEURONAL ACTIVITY PROFILES IN ALERT MACAQUES: COMPARISON WITH OXYGENATION SIGNALS AND UNDERLYING NEURONAL ACTIVITY

The ultimate goal of this thesis involves measuring the spatial structure of neuronal activity across the cortical sheet. Earlier work on the subject has led to mixed results<sup>2</sup>. Therefore, it was first necessary to develop a detailed understanding of how any measured optical signal is linked with underlying neuronal activity and select the optical signal that is most clear and reliable. Though most work to date has focused on BOLD as an indicator of neuronal function, this chapter presents arguments for why it is not a clear marker of the underlying spatial activity profiles. Instead, experimental evidence in this chapter proposes that the blood volume signal is a better spatial marker with both a stronger signal and a clearer interpretation.

#### *2.1. Searching for a Marker of Spatial Patterns of Neuronal Activity*

##### **2.1.1. The Development of Optical Imaging as a Tool in Neurobiology**

There are two general types of optical imaging employed today. One is imaging of specific contrast enhancing agents and others that rely on using intrinsic

---

<sup>2</sup> Especially in the V1 of alert macaque monkeys.

markers. The use of extrinsic agents, specifically voltage sensitive dyes, was the first approach chosen to study the functional organization of the cortex. Voltage sensitive dyes were first developed for use *in vitro* to visualize the propagation of voltage changes along the membrane of individual cells. These lipophilic dyes wedge themselves into cell membranes and signal local changes in voltage by changing their conformation and thus optical properties such as fluorescence or absorption [3]. The potential to applying this technique to measuring population activity was quickly realized and successfully implemented to replace the method of cortical mapping with tracers (e.g. 2-deoxy-D-glucose) because it does not require sacrificing the animal.

However, Amiram Grinvald discovered, in 1986, that a reliable functional signal was measurable from cortex simply by imaging intrinsic changes in the intensity of light reflected off the cortical surface. These “intrinsic signal” changes, though far slower than the electrical signals recorded with dyes, have impressive stimulus specificity and comparably high signal to noise [4]. Whereas the interpretation of voltage sensitive dye signals was relatively straightforward (an average measure of the local membrane potentials), the exact nature of the link between neuronal activity and intrinsic signal responses remains a focus of current research.

Intrinsic signals can arise from changes in light scatter, blood volume, and oxygen concentration at the imaged location. Hemodynamic intrinsic signals are thought to result from local changes in blood delivery to activated neuronal populations. The largest absorber of visible light in brain tissue is hemoglobin; thus a local increase in hemoglobin would decrease the amount of light reflected from the cortical surface. Because oxy-hemoglobin (HbO) and deoxy-hemoglobin (HbR) have different absorption spectra, intrinsic signals measured at different wavelengths carry distinct types of information reflecting the different levels of contribution from the two species. Wavelengths falling on isosbestic<sup>3</sup> points (such as 530 nm: equal absorption in HbO and HbR) yield information about overall blood volume (HbT), whereas wavelengths at which the species absorb differentially (such as 605 nm: HbR absorbs ~ 5x more strongly than HbO) can yield information about the oxygenation state of the blood (blood-oxygen level dependent; BOLD).

### **2.1.2. BOLD: An Unambiguous Marker of Neuronal Activity?**

The classical theory linking neuronal activity to hemodynamic changes posits that active neuronal populations use up local energy resources and that the vascular system compensates by bringing fresh blood to the active area [5]. During activation, it is thought that neurons consume local oxygen, which is

---

<sup>3</sup> A specific wavelength at which two (or more) chemical species have the same molar absorptivity.

provided by HbO, thus converting it to HbR. The increase in local metabolism causes an increase in the local concentration of vasoactive second messengers (H<sup>+</sup>, K<sup>+</sup>, NO, Adenosine; [6]) which then act on the smooth muscle of local arterioles causing vasodilation that increases the influx of fresh blood to the area [5, 6]. The characteristics of this neurovascular response give rise to two general imaging signals: changes in total hemoglobin (HbT), and changes in the oxygenation state of the blood (BOLD) [4, 7]. Changes in HbT are brought about by changes in the net local concentration of either HbR or HbO due to dilation of local vasculature. The 'Oxygenation' signal (typically defined as the signal measured using wavelengths that are absorbed more strongly in HbR than in HbO) is thought to reflect changes in blood oxygenation due to changes in either the metabolic rate of oxygen consumption or flow. Changes in HbR are also the underpinning of the blood oxygen level dependent (BOLD) signal measured in fMRI and the two measures are expected to give similar results.

Functional signals measured at above 605 nm (wavelengths primarily absorbed by HbR) show biphasic response time-courses with an early and transient increase in local absorption ('initial dip'), followed by a larger and more spatially diffuse decrease in absorption relative to baseline ('rebound'). This 'initial dip' has been interpreted as being due to a transient increase in the relative local concentration of HbR reflecting a focal increase in oxygen consumption whereby local HbO gets converted to HbR (thus increasing absorption). Further, it was

proposed that this local increase in oxygen consumption was a direct measure of local neuronal activity. The later rebound was attributed to the less spatially precise action of the vasculature diffusely inundating the activated area with fresh oxygenated blood [7].

Because of its presumed link with local changes in oxygen metabolism, the optical imaging signal that measures this initial dip was proposed, by Grinvald in his pioneering work, as the most direct marker of neuronal activity. HbT was consequently lumped with the rebound and deemed a poorer indicator due to its indirect vascular nature. Over the number of years since Grinvald's groundbreaking work it has become clear, however, that there are several noteworthy problems with the interpretation of the initial dip as resulting specifically from changes in the oxygenation state of the blood and therefore as a direct marker of neuronal activity. The remainder of this section discusses these issues.

It is unclear exactly which aspects of stimulus-related metabolic changes contribute most to the early increase in HbR. Studies using oxygen electrodes find that local decreases in oxygen concentration correlate well with neuronal spiking [8]. However, even neurons that do not fire to a given stimulus still receive substantial subthreshold input, which causes large changes in ionic gradients across neural cell membranes. The restoration of such gradients is very

demanding metabolically, accounts for roughly 10% of the net energy budget of a human [9], and may be dissociated from spiking [10]. Further, it is known that a significant portion of the energy demands of neurons are met through glycolysis, which, though less efficient, is a faster means of energy production than aerobic respiration [11-13]. Neural tissue that resorts to glycolysis for energy may go into oxygen debt. Glycolysis produces pyruvate, which is eventually broken down aerobically, thus possibly incurring a greater oxygen cost at vigorously stimulated areas after stimulation. If different neuronal functions recruit aerobic vs. anaerobic processes to different extent, then local deoxygenation may in turn be more sensitive to only particular components of the neuronal response. For example if spiking correlates more tightly with local oxygen consumption, the early increase in HbR will reflect only changes in spiking neurons and not other neurons that are also metabolically active, but either at subthreshold levels or because they are receiving a balanced input of excitation and inhibition.

Even if all aspects of neuronal responses relied on aerobic respiration, there are still serious confounds in interpreting the optically measured initial dip as the veridical localizer of oxygenation changes [14]. Though absorption at 605 nm is dominated by HbR there is significant absorption by HbO, with roughly 1/5 the absorption coefficient of HbR. Either conversion of HbO to HbR or an increase in either HbO or HbR (resulting in an increase in HbT) would lead to increases in

absorption at these wavelengths. If local increases in blood volume are approximately simultaneous with changes in the local HbO/HbR ratio, then at least part of the signal is due to changes in volume, versus any true changes in oxygenation [15, 16]. In fact, recognition of the putative contribution of blood volume to the initial dip has led to considerable revision of the appropriate time window to use for observing changes in oxygenation alone (from 3-4 sec post stimulus [17], to 0.4-1.2 sec post stimulus [18]).

The temporal structure of the signal also underscores the difficulty of its interpretation. During the rebound phase, incoming arterial blood increases the HbO/HbR ratio enough to decrease the net absorption at typically used oxymetric wavelengths, thus giving the signal its biphasic nature. This means that during the response, there is a push-pull relationship between changes due to increases in HbR that increase absorption in proportion to neuronal activity and the influx of highly oxygenated arterial blood, also in proportion to neuronal activity, which serves to decrease absorption. The exact crossover point could therefore have a complex relationship with the intensity and duration of the local stimulation. Any estimates of the HbR concentration that depend on using a single wavelength will suffer from this confound. Any reliable estimate of the changes in HbR distinct from changes in HbO can only come with simultaneous measurements at multiple wavelengths that can independently measure these species.

To simplify analysis, early studies adopted the practice of focusing the imaging camera below the cortical surface, thus mixing contributions from the different vascular compartments. However, different vascular compartments in the brain have different resting state oxygen saturation. The typical oxygen content of arterial blood is ~98% and it reduces to about 60% in veins [19, 20]. Thus, although 80% of the signal at 610 nm comes from HbR, this species only makes up 2-40% of the absorber (depending on the vascular compartment), and changes in its concentration can produce a range of fractional changes in absorption in different compartments. Thus, even though changes in neuronal activity may be neatly linked to oxygen consumption, oxygen consumption is not directly linked to fractional changes in absorption at HbR weighted wavelengths, which could differ drastically depending on the local vascular makeup.

Compounding all these ambiguities is the additional fact that signals obtained at wavelengths measuring HbR (typically longer than 605 nm) are overall absorbed more poorly by hemoglobin and give low fractional signals relative to changes in HbT, which can be measured at wavelengths absorbed strongly [14, 16, 21, 22]. For all of these reasons, the traditional interpretation of the 'initial dip' signal as a reliable marker of neuronal activity is problematic.

### 2.1.3. Developing Blood Volume as a Spatial Marker of Metabolic Demand

Despite plausibly direct links with neuronal energy metabolism and widespread use, the BOLD signal may not have the necessary qualities that make it the unambiguous choice for probing spatial structure of neuronal responses. An alternative, but less common technique focuses on changes in blood volume (HbT) that also accompany neuronal activation (see 2.1.1; [14, 16, 21-24]). Several studies have suggested that, due to its vascular nature, the HbT signal is a poorer marker of neuronal activity ([7, 18, 25] **but see** [24]). However, as discussed above, the signal measured at any one single (HbR-sensitive) wavelength cannot be interpreted as a measure of HbR concentration alone due to the confounding contributions from changes in the overall blood volume and flow. This section argues that the HbT signal is a more reliable measure of neuronal activity. Nevertheless, before proceeding further, it is important to address some of the major issues in interpreting a purely vascular signal.

The major caveat regarding HbT as a marker of neuronal activity is its clear link with the dilation of vascular compartments, which are arguably more decoupled than BOLD from local metabolic changes resulting from increased neuronal activity. In addition to direct action of metabolism-related second messengers, dilation of arteriolar smooth muscle is also affected by calcium influx into neurons and astrocytes via release of the second messenger nitric oxide (NO) [26]. Large increases in intracellular  $\text{Ca}^{2+}$  in both cell types can be triggered by

glutamate. Thus, it is possible that the amount of local glutamate may directly cause vasodilation of arterioles in parallel with, and not in response to, increases in neuronal activity [10]. This is not a problem, *per-se*, because activation by this pathway would be proportional to the local glutamatergic input which is likely closely related to neuronal activity.

Again, because of their relationship with vasculature, it has been suggested that HbT signals are biased away from the actual site of neuronal activity or glutamate release toward larger arterial compartments (e.g. [7, 18, 22, 25]).

However, capillaries, which have no smooth muscle, may also dilate, resulting in an increase in HbT. These finer vessels penetrate deep into cortical tissue and are finely spaced. Their contraction and dilation may be controlled by pericytes in a transmitter dependent manner [27]. Thus, the resolution of the vascular signals may be much better than the granularity of large arterioles and this can account for their successful use as mapping signals [23], a question addressed directly later in this chapter.

#### **2.1.4. Remote Sources of Vascular Signals**

A further source of complexity in interpreting HbT signals is that not all vascular changes are local in nature. Firstly, pial arteries are densely innervated by perivascular nerves originating from autonomic and sensory ganglia. These

nerves may release several neuromodulators and peptides that may cause either contraction or dilation of arteries (including Noradrenalin, Acetylcholine, Substance P, and Vasoactive Intestinal Peptide). Dopaminergic axons, commonly associated with neuromodulation, directly innervate intraparenchymal vessels and may regulate local vasomotion [28]. However, efferent connections from autonomic ganglia are often diffuse across the entirety of the cortical regions they target and therefore should not directly alter the spatial profile of activity due to spatially specific thalamic input. Further, neuromodulatory afferents often terminate diffusely (on neurons, glia, and vasculature) and therefore the release of neuromodulatory substances may simultaneously affect both the neurons and vasculature (see Chapter 3), thus potentially yielding important information about the state of the neural network.

### **2.1.5. Blood Volume vs. Spiking**

Because of the complexity of the blood volume signal, it is worthwhile to highlight cases where there should be clear differences between these signals and spiking activity. Spiking responses result from an increase of membrane voltage to some threshold. Thus, decreases in membrane potential will not result in changes in spiking activity in a cell that maintains no baseline firing. However, the blood volume signal is believed not to directly measure changes in membrane voltage, but rather the metabolic correlates of those changes. Thus,

both positive and negative modulations of membrane voltage can, in principle, give rise to increases in metabolic demand [10, 29]. Further, even if membrane voltage stays constant, but there is an increase in membrane conductance, this would also cause high metabolic activity while not affecting the mean rate of discharge. Thus, it is important not to infer changes in neuronal firing directly from either the sign or the amplitude of the optical signal. Only in cases where the metabolic load and spike rate are proportional should the two signals show a clear relationship. The above caveats, however, apply to both the HbT and HbR signals.

As discussed earlier, the hemodynamic signal can result either from direct action of neurotransmitters on local astrocytes and pericytes or from response to local metabolic demands of neurons. The nature of these sources suggests that the signal carries information about the level of input into and net impact on the local network. Thus, the signal is likely generally more related to the input rather than output (spiking) of the local neurons. Far from being a disadvantage, this shows that hemodynamic signals allow examination of many aspects of cortical processing that may not change the output such as balanced changes in excitation and inhibition, effects of neuromodulators, or subthreshold inputs.

### 2.1.6. Prior Work Using Optical Imaging

There is a rich history of experiments comparing hemodynamic responses at several wavelengths in rats ([14, 16, 21, 22, 24, 30-34] and many others) and monkeys, both awake and anesthetized [7, 17, 18, 25, 35, 36]. These studies have pioneered the use of optical imaging as an experimental tool for mapping fine scale cortical organization.

Much of what we know about the spatial structure of hemodynamic response comes from work in the cortex of the anesthetized rat. These studies suggest that all three hemodynamic response components (HbT, HbO, and HbR) colocalize to individual barrels during single whisker stimulation. Changes in HbR and HbT appear to have similar spatial spread with a larger spread for HbO [16, 22], but with different levels of signal to noise ([22]; HbT appears to have the highest and HbR the lowest). Changes in HbT appear most prominent in arterial compartments [24, 33], whereas changes in HbO are biased towards draining veins [24]. Despite general agreement in this literature that HbT is a highly localized and sensitive signal [24], some studies suggest that several seconds post stimulus, HbT localizes in arterial compartments away from the stimulated neuronal population [22]. If this holds in the visual cortex of the monkey, it may significantly reduce the value of this signal as a marker of neuronal activity.

The studies in rats are typically carried out in somatosensory or barrel cortex and stimuli range from relatively natural whisker deflection to highly unnatural electrical shocks to different parts of the body. Thus it is important to determine whether the results of these studies apply to responses from the V1 of alert macaques. Only studies in monkeys were carried out in visual cortex. And these studies focused on measuring responses to large visual stimuli and considered as mapping signals only those that reveal functional architecture (e.g. orientation columns). In considering the applicability of these different signals to mapping cortical architecture, these studies have neglected to examine the spatial structure of responses recorded at different wavelengths to retinotopically isolated stimuli. **In fact, no studies to date have rigorously compared cortical activity profiles in V1 to focal stimulation at multiple wavelengths.**

The search for the most appropriate mapping signal has led some to conclude that early increases in deoxyhemoglobin at the loci of neuronal activity are the best markers of neuronal activity. Though both wavelengths measuring blood volume and those measuring oxygenation carry mapping signals (e.g. difference signals between stimuli of two orientations; [7, 18, 25, 35]), signals from wavelengths absorbed primarily in HbR can be used to obtain single-condition maps (i.e. a larger fractional signal change in functionally tuned cortex than in un-tuned cortex). This observation, by itself, has largely been used to support the above argument. However, such single condition signals have obtained with

full-field visual stimulation and it appears premature to conclude that the initial dip is the most reliable signal in general.

## ***2.2. Results from Simultaneous Optical Imaging of Intrinsic Signals at Two Wavelengths and Electrophysiology in Alert Behaving Monkeys:***

Since it is necessary to determine the appropriate signal to use for mapping spatial patterns of neuronal activity, and since signals at different imaging wavelengths provide different information, we set up an imaging system to simultaneously acquire signals at several wavelengths. We chose one wavelength centered on an isosbestic point between HbR and HbO (530 nm) and one primarily measuring HbR (605 nm). What follows is a direct comparison between the fine spatial structure of responses at 530 nm ('HbT') and at 605-630 nm ('HbR', 'BOLD') to visual stimuli and their relationship with underlying neuronal activity in V1 in fixating macaques showing that HbT may be a better marker of the spatial pattern of neuronal activity in the V1 of macaques. I will begin by demonstrating the ambiguity of the signals obtained at 605 nm by showing that changes in blood volume are a significant component of functional signal changes this wavelength.

### **2.2.1. Vascular Contributions to the Initial Dip**

One of the major ambiguities of the source of the initial dip is its variable manifestation. Using a variety of techniques, some labs reliably report its presence and prominence while others hardly detect it at all ([37] and refs therein). In the course of our investigations, we could reliably detect an initial increase in absorption at long wavelengths, but its prominence was variable, and it was typically small relative to the subsequent decrease in absorption at the same wavelength (rebound). To understand the origin of the measured signal, we asked whether the variability in the initial dip is attributable to the

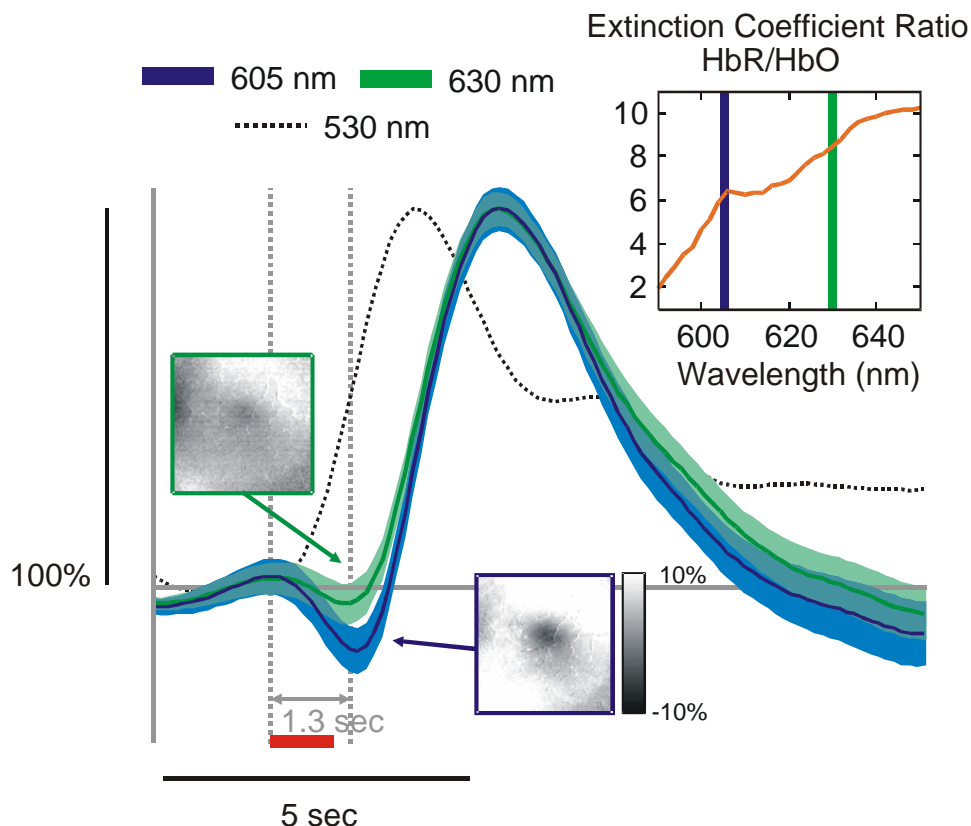


**Figure 2.1. The initial dip is not solely a measure of deoxyhemoglobin.**

The stimulus response timecourses to small retinotopically isolated line segments were examined at two wavelengths primarily absorbed by deoxyhemoglobin (HbR). The main panel plots response timecourses at 605 nm (blue), 630 nm (green) and, for reference, 530 (an isosbestic point) scaled to maximum response. The ratio of the dip to rebound is smaller at 630 nm even though HbR accounts for more of the absorption at that wavelength (top-right inset; data from [38]). Inset images show the image of the initial dip. Note the weaker initial dip pattern at 630 nm and a large value of blood volume at the peak of the initial dip. Red bar marks stimulus presentation. Color bars denote percent maximum response. Shaded error is SEM.

relative contribution of changes in HbT as versus changes in HbR at the imaged wavelength. If the initial dip is due to an increase of local HbR, independent of

changes in HbT, then at wavelengths that absorb relatively more in HbR, we should see an enhanced initial dip relative to the rebound. Surprisingly, however, we found that wavelengths with a higher relative absorption in HbR actually showed weaker initial dips (Figure 2.1). If the initial dip was measuring solely the increase in HbR due to neuronal activity, then it should have been stronger, relative to the rebound, at 630 nm. We suggest that the initial dip observed in alert monkeys at typical imaging wavelengths originates largely from changes in blood volume and not oxygenation [15, 16, 24].

Our observation that the 'initial dip' is not a reliable measure of HbR but, rather, likely contains a significant contribution from HbO is also suggested by a closer reading of the literature that uses the 'initial dip' in imaging. Detailed studies of the initial dip consistently show increases in HbR after the onset of neuronal activity, however, these studies do not show concomitant decreases in HbO ([15, 39]; interestingly some studies report delayed changes in HbT (e.g. [40])). Signals measured at this time must carry a contribution from the overall blood volume signal, which we find to be halfway to its peak at the time of the initial dip (see Figure 2.1). Thus, early changes in blood volume are contemporaneous with any presumed early changes in oxygenation.

### **2.2.2. Oxygenation signals feature clear and opposite contributions from arteriolar and venous compartments**

To gain a better understanding of the contribution of individual vascular compartments to changes in HbT and oxygenation, we imaged the pointspread to a small visual stimulus at a resolution that allowed us to identify small vascular compartments. Individual arterioles and venules were identified based on differential absorption at 530 vs. 605 nm. Arteries and arterioles, carrying oxygenated blood absorb well at 530, but little at 605, whereas veins and venules with a larger concentration of deoxyhemoglobin, absorb well at both wavelengths (Figure 2.2b). On the basis of these vessel absorption patterns and sizes we identified arteries, arterioles, venules, veins, and parenchyma (cortical portions with no resolvable vessels) about the stimulated cortical location. Next, we examined the stimulus driven pattern of absorption changes in the different compartments (Figure 2.2c,d).

At 605 nm, we found that we could detect early (by 1.1 sec) increased absorption in arterioles, parenchyma, and some venules which was followed by a later (>2 sec) decrease in absorption primarily in venules and veins (Figure 2.2c).

Interestingly, at ~2.3 sec after stimulus onset, the overall signal intensity was near zero, but this is due to increased absorption in arterial compartments being balanced by a decreased absorption in venous compartments. At 530 nm, we also saw the early increase in absorption, primarily in arterioles and

parenchyma, with a pattern that corresponded well to that seen early (<2.3 sec) at 605 nm. Unlike at 605 nm, however, the response pattern remained largely invariant across the first 4 seconds of the response (with progressively greater arteriolar dilation and an increase in absorption in some small venules localized around the stimulated area) despite large changes in signal amplitude (Figure 2.2a,d). Later (>4 sec) in the response at 530 nm, we could also detect increases in absorption in the larger arteries (data not shown).

These data demonstrate that the initial dip (at ~1.5 sec) has a significant vascular component likely due to changes in local blood volume. Further, oxygenation increases (decreases in absorption at 605 nm) appear largely in the venous network (probably due to late changes in blood flow) even while the arterial network still shows a larger absorption (likely due to increased blood volume). The blood volume pointspread pattern at 530 nm is most similar to that observed during the initial dip at 605 nm, but shows a much larger signal which is largely temporally invariant. Thus, the blood volume signal is as good a marker of the locus of neuronal activity as the initial dip, but retains spatial specificity over much longer duration (also see below).

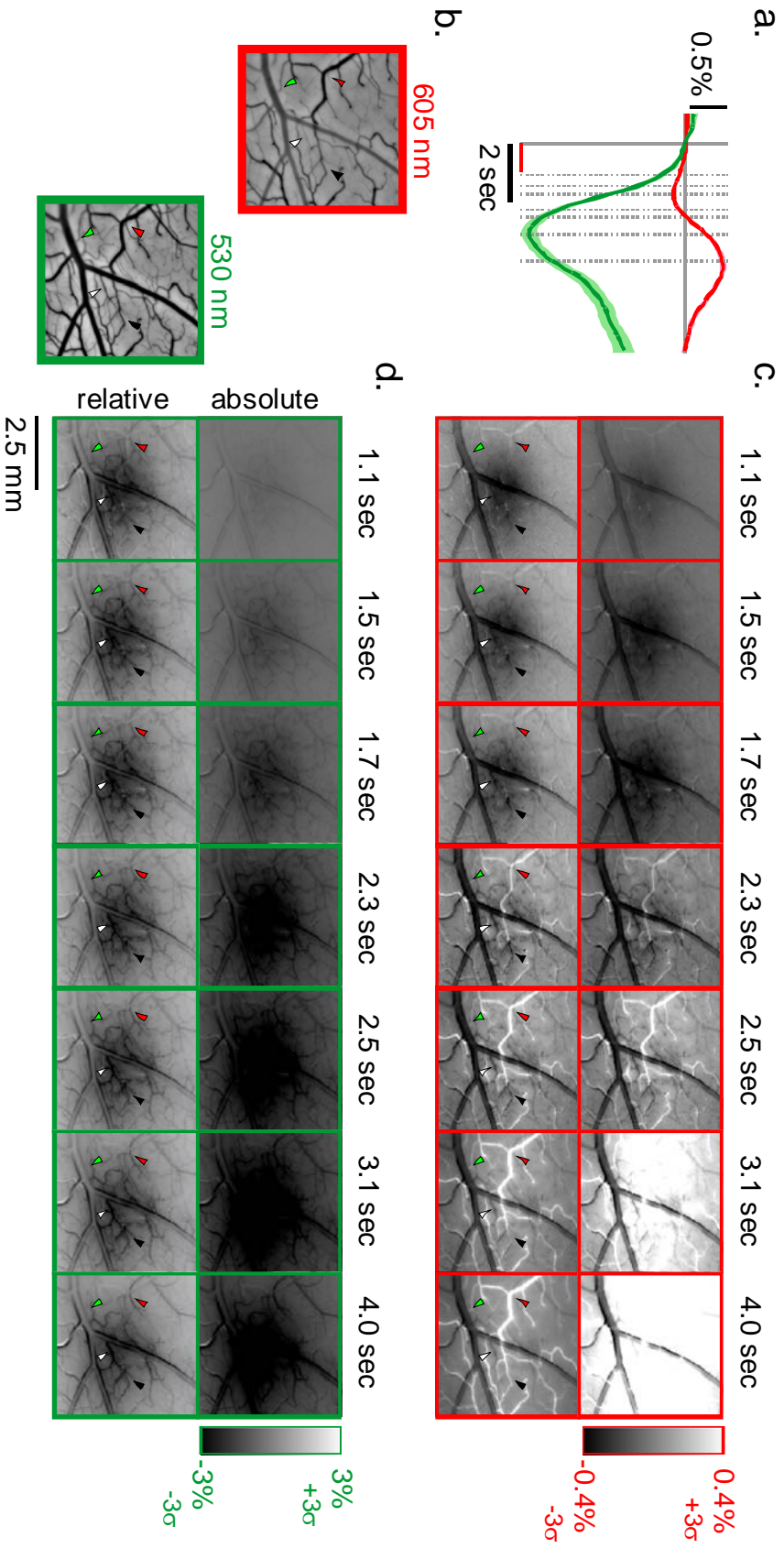


**Figure 2.2. The evolution of hemodynamic responses at 605 and 530 nm highlights the role of different vascular compartments in generating the oxygenation response.**

**a.** The time-course of the mean imaging signal across the ROI for 605 nm (red) and 530 nm (green) light in response to a one second presentation of a 0.25 deg bar. Dotted lines represent time-points shown in c and d. Red bar is stimulus duration. **b.** Pictures of vasculature imaged at 605 nm and 530 nm identify different vascular compartments: vein (red arrow); artery (green arrow); arteriole (white arrow); venule (black arrow). **c-d.** Images taken at different post stimulus time-points. Arrows as in b. The top row of images has a fixed clip indicated on the colorbar (to show the mean response). The bottom row has a clip equal to  $\pm 3$  standard deviations of responses across the image (to enhance identification of vascular patterns). Note the early and largely invariant response at 530 nm compared to the rapidly reversing response at 605 with contributions of opposite sign from arterial and venous compartments.

**2.2.3. Changes in Blood Volume have Better Signal to Noise and Spatial Precision than the hyper-oxygenation rebound**

To determine which signal offers better stimulus driven signal-to-noise, we took, as our estimate of the noise, the baseline signal strength on “blank” trials (trials where the animal fixated, on normal schedule, but with a blank gray screen, no stimulus. These ‘blank-trials’ were used to estimate the magnitude of the non-stimulus driven component of the signal. The average response at peak to the stimulus at 530 nm was 4.2%, whereas at 605, the peak response was only 0.4%

(Figure 2.3a; an order of magnitude smaller than expected simply from a decrease in absorption at 605 nm<sup>4</sup>).

To quantify how much of the signal at each wavelength is due to the stimulus and how much due to ongoing hemodynamic fluctuations, we computed, trial-by-trial, the standard deviation at each wavelength over the trial period. The signal at 530 nm had much larger overall variance on stimulated than blank trials, but it was difficult to tell the two apart at 605 nm suggesting a larger stimulus driven contribution to the overall variance at 530 nm (Figure 2.3b). The overall variance at 530 should be larger than that at 605 because of the increased absorption. On blank trials, the variance at 530 was indeed 2.29 times larger than the variance at 605; however, stimulation increased this ratio almost twofold to 3.94 demonstrating that visual drive increased the variance disproportionately more at 530 nm (Figure 2.3c). Thus, as suggested on the basis of prior work in anesthetized rodents, blood-volume signals measured at 530 nm have a larger amplitude and signal-to-noise than simultaneously acquired oxygenation signal at 605 nm [24].

---

<sup>4</sup> The overall absorption by haemoglobin at 530 nm is about 5 times larger ( $\epsilon_{\text{Hb}_{530}} = 39036.4$ ;  $\epsilon_{\text{HbO}_{530}} = 39956.8$ ;  $\epsilon_{\text{Hb}_{605}} = 12567.6$ ;  $\epsilon_{\text{HbO}_{605}} = 2128 \text{ cm}^{-1}/(\text{moles/liter})$ ) than the absorption at 605 nm.

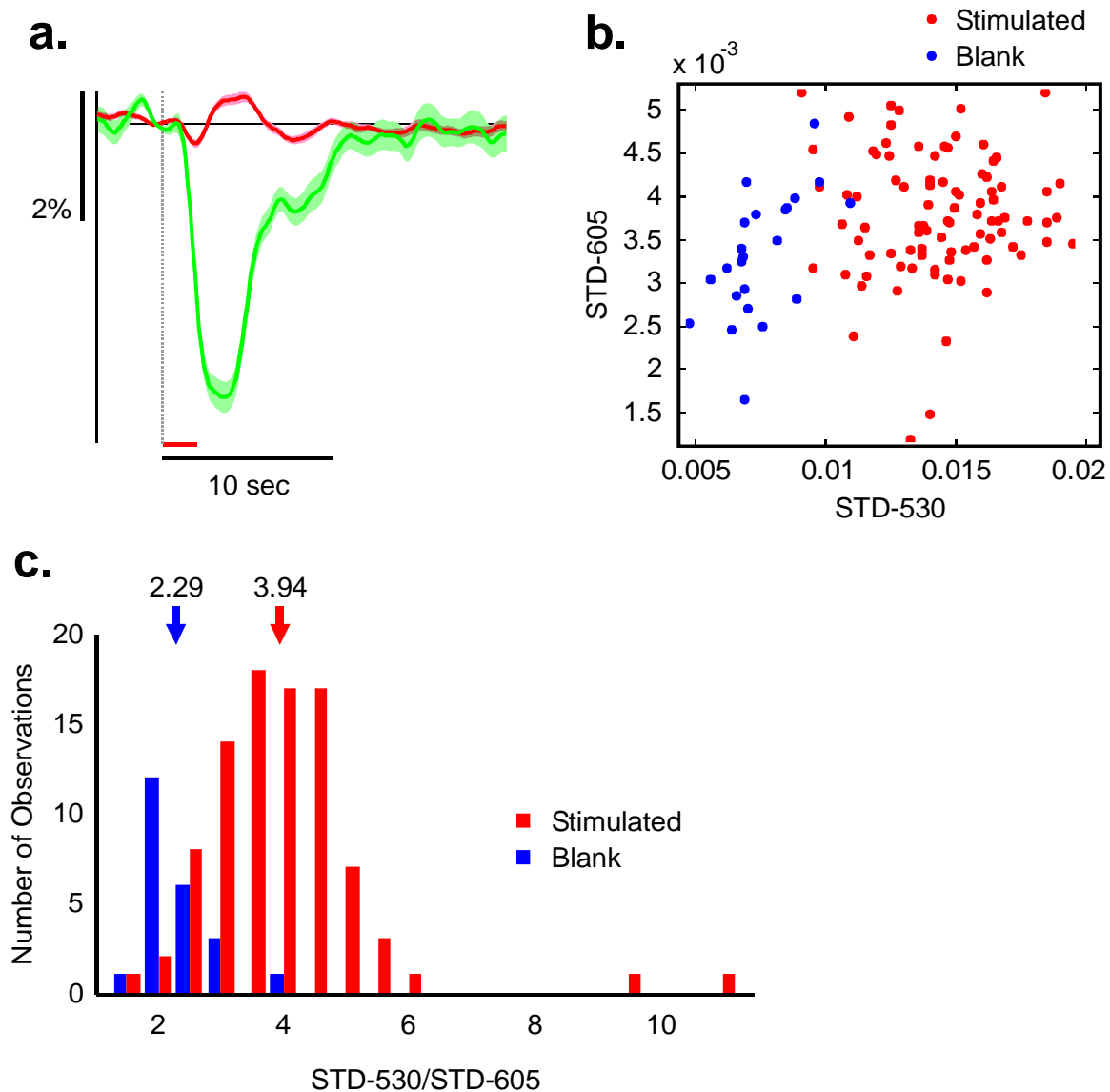


**Figure 2.3. Blood volume signals have a higher stimulus driven variance than oxygenation signals.**

**a.** Average responses recorded at 530 (green) and 605 (red) wavelengths to a full-field grating presented for 2 seconds (red bar). **b.** The trial-by-trial standard deviation of signals measured at 530 compared to 605 for stimulated (red) and blank (blue) trials. Note how easy it is to separate stimulated from blank trials at 530, but not at 605. **c.** Histogram showing the ratio of the standard deviation at 530 vs. 605 nm for stimulated (red) and blank (blue) trials. Note that the ratio for stimulated trials is almost two-fold larger than for blank trials.

Despite being a larger signal, we found little difference in the size of the pointspread at 530 and the size measured during the 'initial dip' phase at 605 or 630 nm (Figure 2.4). For each wavelength, we computed timecourses of activity in radial ROIs centered on the pointspread. For each timepoint, the profile of activity across the ROIs represents the average shape of the pointspread. To compare across wavelengths and signal intensities, we normalized all profiles from 0 to 1. Specifically we looked at the shape of the response at the peak of the initial dip and the peak of the rebound (Figure 2.4, i-k). We found that the shapes of the normalized profiles of the initial dip at either 605 or 630 nm matched those observed at 530 nm. The signal at 630 nm was noisier due to a significantly lower overall absorption and the smaller initial dip at that wavelength (Figure 2.1). The profile of the rebound, on the other hand, was significantly wider than that of either the dip at the same wavelength or the pointspread at 530 nm. Notably, the peak of the rebound was often away from and surrounding the center of the stimulated area. This may be due to the large contribution of draining vessels to the rebound or to opposing influences of blood volume and oxygenation (due to flow) on the signals at 605 nm (Figure 2.2, c; Figure 2.4, d).

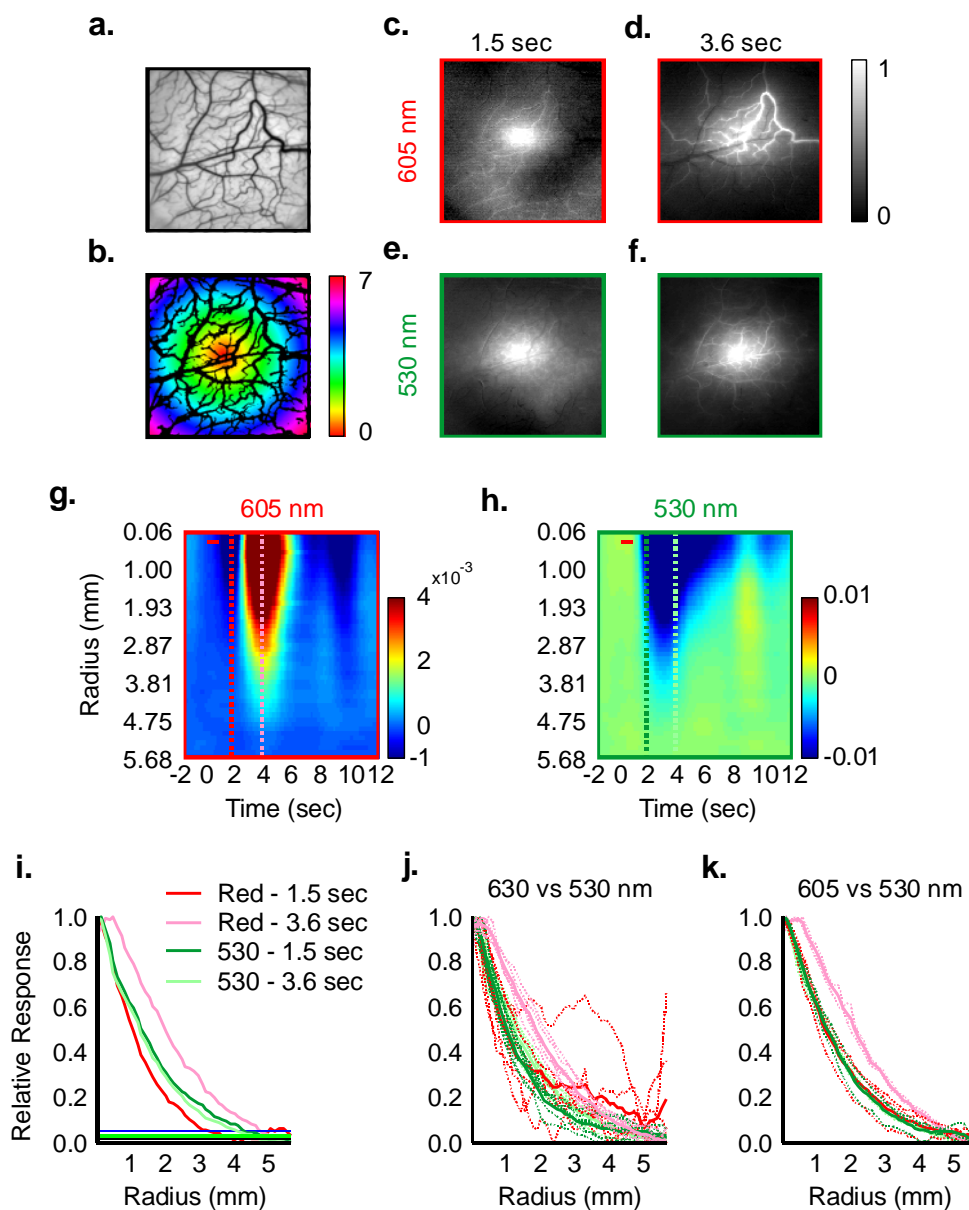


**Figure 2.4. The blood volume pointspread has a similar spatial profile as the initial dip, but is narrower than the hyperoxygenation rebound.**

a. The vascular map over V1 at 530 nm. b. Radial ROIs, centered on the pointspread and avoiding the vasculature. The colorbar codes distance. c-d. Images of the pointspread at 605 nm during the dip (c) and rebound (d). For ease of spatial comparison, the images were scaled from 0-1. e-f. The pointspread measured at 530 nm at the same timepoints as c-d. g-h. Pointspread amplitude as a function of distance from center and time at 605 (g) and 530 (h) nm. Red bar

represents stimulus presentation. **i.** Pointspread amplitude as a function of distance during the dip and rebound at 605 and 530 nm. Data are the same as in a-h. **j-k.** Same as i, but across experiments comparing 630 and 530 nm (j) and 605 and 530 nm (k). Dotted lines are individual experiments. Solid lines are averages. Note the similarity between the spatial spread of the dip and the blood volume signal but increased width with a peak away from the center for the rebound.

The HbT signal is a good indicator of the spatial profile and location of neuronal activity. There are several properties of the HbT signal that suggest that it has a fine-scale relationship to neural activity. Voltage sensitive dye recordings have previously shown that a small retinotopically isolated stimulus evokes a wide profile of electrical activity across cortex (the pointspread; [41, 42]). To determine whether the physical dimensions of the blood volume pointspread match those from electrophysiological recordings, we measured the profile of activity to small  $0.25^\circ$  bars. To compare with prior data, we fit our responses with two dimensional exponential and Gaussian functions. We found that the dimensions of our measured response matched perfectly those derived using VSD (Table 2.1).

<b>Group:</b>	<b>Major Axis:</b>	<b>Minor Axis:</b>
<b>Sirotnin and Das (HbT)</b>	2.5 mm, (2.17 mm)	1.2 mm, (1.60 mm)
<b>Grinvald et al. 1994 (VSD; only Exponential)</b>	2.9 mm	1.5 mm

Chen et al. 2006 (VSD; only Gaussian)	(1.97 mm)	(1.34 mm)
---------------------------------------	-----------	-----------

**Table 2.1. Dimensions of cortical point-spreads obtained from blood volume vs. voltage sensitive dye measurements.** 2D exponentials or Gaussians (in parenthesis) were used to fit the shape of the observed point-spread and the major and minor axis space constants are reported here. Note the general agreement between the spatial scale of VSD and HbT responses.

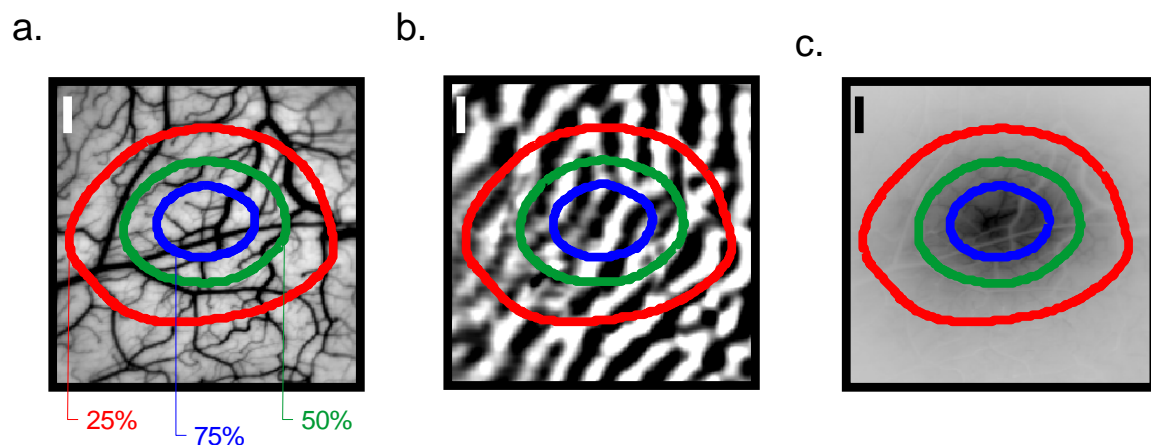


**Figure 2.5. The hemodynamic point-spread at 530 nm is elongated across ocular dominance columns.**

**a-c.** The 25, 50, and 75% response contours superimposed on the local vascular map (a), the ocular dominance map obtained using eye shutters (b) and the image of pointspread itself (c). Note the elongation across ocular dominance columns in b and the lack of contribution by large vessels in c in shaping the response profile.

This correspondence between the HbT pointspread and those observed using VSD is likely due to neuronal synaptic input [13, 43]. Firstly, consistent with prior results from anesthetized animals [35], the HbT pointspread is elongated across ocular dominance columns (Figure 2.5), which is consistent with the architecture of LGN input and long-range connections in V1 [44]. Further, the pointspread is not a result of slow hemodynamic changes and remains largely invariant across the signal's rise-time when the amplitude of the signal changes

rapidly (Figure 2.2; Figure 2.4; Figure 2.6). Unlike the rebound observed in the oxygenation signal, the HbT pointspread remains well centered throughout its lifetime (even as late as 12 seconds after stimulation and well after the end of the rebound at 605 nm), thus areas with increased oxygenation during the rebound, do not directly correspond to areas of increased blood volume because large difference in the vascular compartments from which the signals originate (HbT from arterioles and HbO from large veins; Figure 2.6, Bottom).

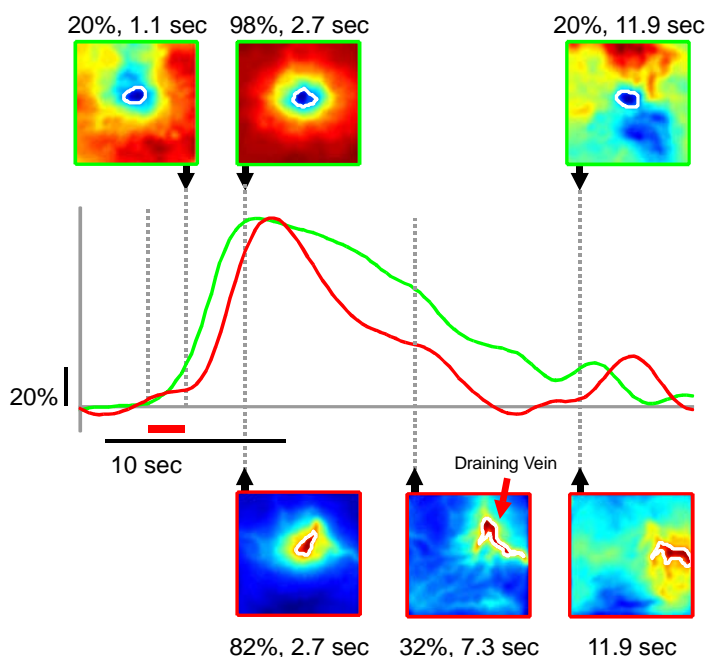


**Figure 2.6. Blood volume is a better spatial marker of neuronal activity than the hyperoxygenation rebound.**

**Middle:** The time-course of the stimulus response measured at 530 nm (green) and 630 nm (red).

**Top:** The profiles of the 530 nm pointspread (scaled from 0 to 1 and low pass filtered ( $\sigma=390\mu\text{m}$ )) at the indicated timepoints corresponding to the indicated relative signal intensity. The white contours correspond to 75% of the maximum response at each timepoint. Note that despite a relative increase in background noise, the location and size of the response remains largely invariant. **Bottom:** same as top but for the signal at 530 nm. Note that the 75% contour shifts progressively toward a nearby draining vein. Red bar denotes stimulus presentation.

Despite the large extent of its pointspread, the HbT signal shows remarkable spatial specificity throughout its lifetime. Unlike the initial dip, the HbT signal is long lived (Figure 2.3, Figure 2.6). To determine the relationship of the signal to the underlying neuronal activity throughout its full lifetime of  $\sim 15$  seconds we

calculated the orientation tuning of the signal at different timepoints after stimulus onset. We found that the tuning for such stimulus features persists throughout the full lifetime of the stimulus response at 530 nm and difference maps for orientation can be obtained at any point along the response. Thus, relative increases in neuronal activity at activated orientation domains recruit additional blood volume that persists for the full 15 seconds.

To compare this with oxygenation signals, we performed the same analysis on the simultaneously acquired signals at 605 nm. If the oxygenation rebound were proportional to the initial dip, the 605 nm signal should have flipped polarity during the rebound phase (i.e. dark patches turn bright and vice versa). Surprisingly, we found that despite the presence and magnitude of the oxygenation rebound relative to the dip, the tuning for orientation remained invariant along the full duration of the response and, furthermore, had a similar temporal profile to that observed at 530 nm (Figure 2.7). These data suggest that, on the spatial scale of cortical columns, the oxygenation rebound signal at 605 nm is either not proportional to the underlying metabolic demand, which is unlikely [23, 24] or is interfered with by the increased absorption due to HbT and by similar mechanisms that cause the mislocalization of its center in the pointspread from an isolated stimulus (Figure 2.4).

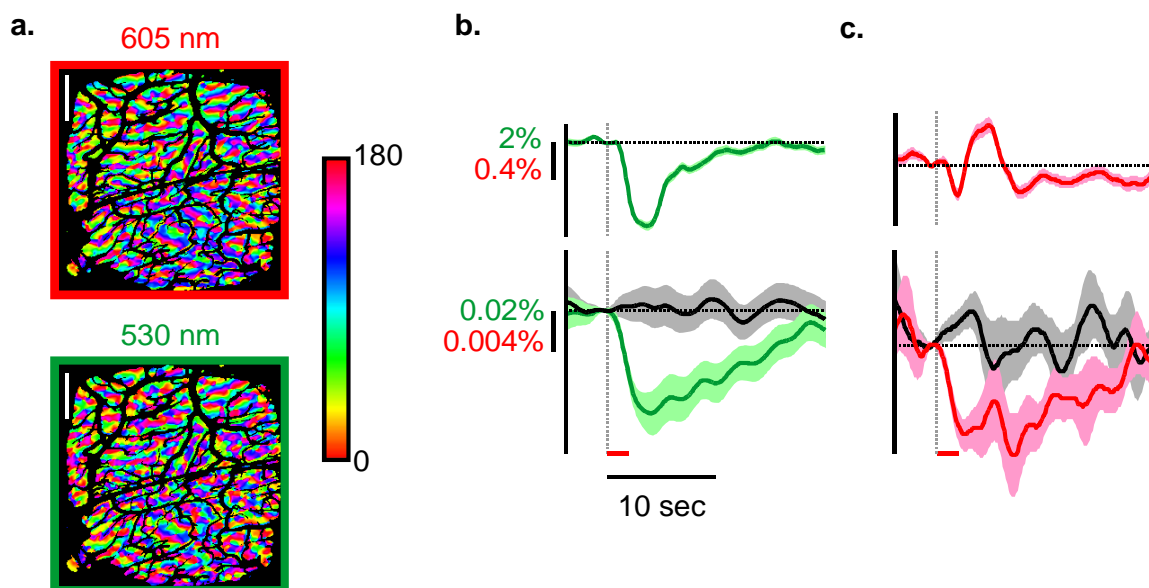


**Figure 2.7. The blood volume signal shows more robust orientation tuning than oxymetric signals.**

a. Orientation maps obtained using 605 and 530 nm are consistent across the extent of the ROI. Blood vessels and regions of poor illumination have been masked. Scale bar is 2mm. **b. Top.** The time-course of the mean stimulus triggered response at 530 nm. We measured the timecourse of orientation tuning at 530 nm as the difference between responses in the stimulated orientation columns versus orthogonally tuned columns (mapping signal). As a control, we also measured the difference between the orthogonal set of columns (gray traces). **c.** Same as a, but at 605 nm. Note the relatively poorer tuning as well as inconsistency in the time-courses of the mean and the mapping signal. Error is SEM. Red bar represents stimulus presentation.

We further measured the limit of the spatial resolution for the blood volume signal. Using controlled retinotopic shifts of the visual stimulus, it is possible to arbitrarily specify any cortical shift expected according to the local cortical magnification factor. We presented small spots of light ( $0.04^\circ \times 0.04^\circ$ ) shifted, on different trials, in  $0.04^\circ$  steps (Figure 2.8). We found that the HbT signal could be

used to distinguish retinotopic shifts leading to displacements of only ~80 microns on cortex. This suggests that, using blood volume, it is possible to discern the locus of neuronal activation on a scale even finer than the average spacing between cortical columns (~300 microns).

As expected, whereas the HbT signal maintained the same phase throughout the response duration as it did with orientation tuning (Figure 2.7), the signal at 605 nm reversed phase during the rebound (Figure 2.8b). The presence of this reversal is highly problematic to the interpretation of oxygenation changes as markers for the spatial profile of metabolic demand (see below).

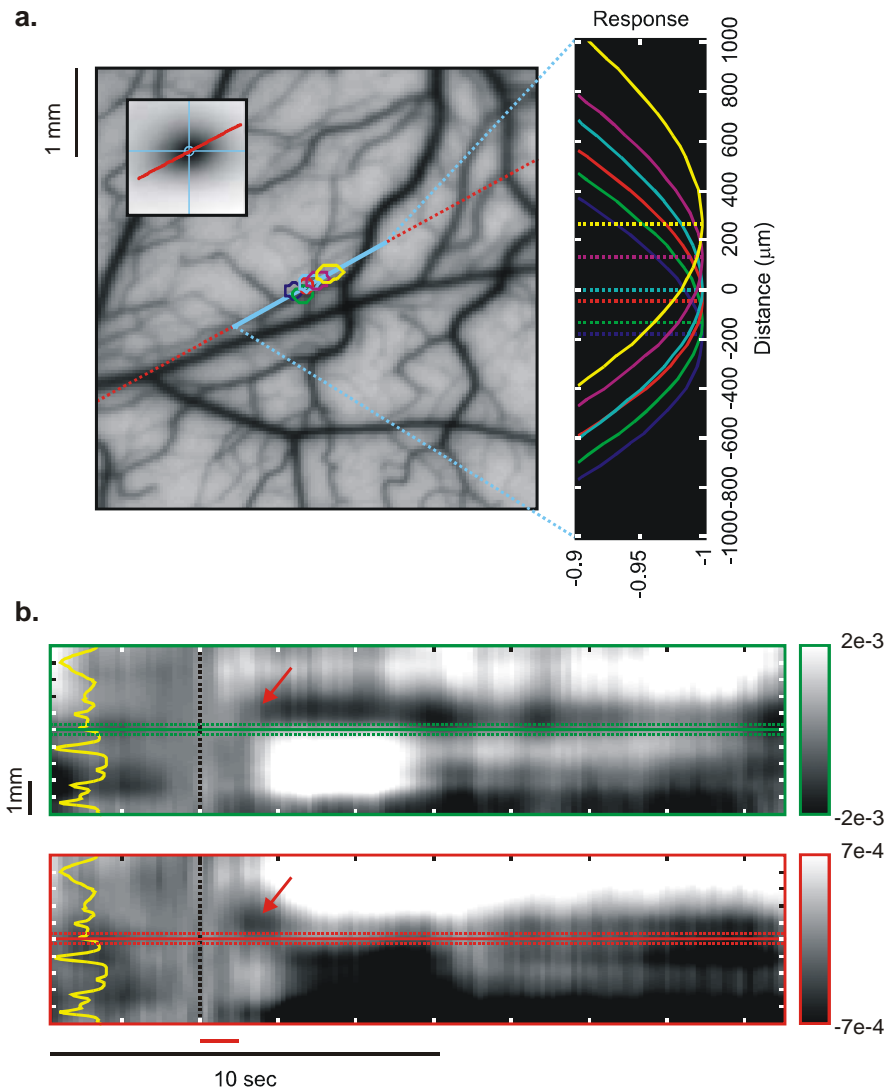


**Figure 2.8. Blood volume responses show high spatial specificity and mono-phasic time-course.**

**a. Left:** Responses to six spots of light presented in alternate trials with  $0.04^\circ$  spacing moving along the horizontal (blue line). The outlines are 99.5% contours obtained from smoothed responses (example in inset). Blue is the leftmost and yellow is the rightmost retinotopic position. **Right:** Response profiles along the retinotopic path corresponding to the direction of spot displacement (blue line) for the six positions. Note the center of the responses moves progressively along the path. **b.** Response profiles along the path connecting response center-points for spots separated by  $0.12^\circ$ . Responses to spots at the two positions were subtracted and

the profile was taken over the difference image. Darker vs. lighter colors illustrate higher responses to one vs. the other spot. **Top:** the signal at 530 nm maintains position tuning throughout its lifetime. **Bottom:** the signal at 605 nm shows initially (initial dip) the same phase as the signal at 530 (arrow) and then reverses during the rebound. The yellow trace on the left marks vasculature along the profile (deflections toward the left are blood vessels). Dashed lines are the center-points of each spot along the profile.

#### 2.2.4. Linear Temporal Summation of HbT Responses

In addition to its excellent spatial localization, the HbT responses to temporally asynchronous stimuli sum linearly. Since the HbT response originates from the dilation of vascular compartments with physical limits, we asked whether the presence pre-existing blood volume caused by stimulation interfered with the response to additional stimulation requiring a further increase in blood volume. While the animal maintained fixation, we flashed short 0.25° bars for 500 msec at various inter-stimulus-intervals (ISIs). To remove any stimulus-independent response components, we linearly regressed the average response point-spread for single bars flashed at different times during the trial across time (see methods). The slope of the regression represents the amplitude of the stimulus specific component and is independent of any fluctuations in the mean signal intensity over time (see Chapter 2.4). We quantified the timecourse of the stimulus response for the different ISIs and compared it to the sum of the responses to individual bars presented at the appropriate timepoints (Figure 2.9).

We found excellent linearity of response summation for all ISIs. Thus, despite already elevated levels of blood volume, additional stimulation was able to recruit further volume increases in a linear manner. Though blood volume cannot be expected to increase indefinitely, this suggests that the hemodynamic system operates within a linear range.

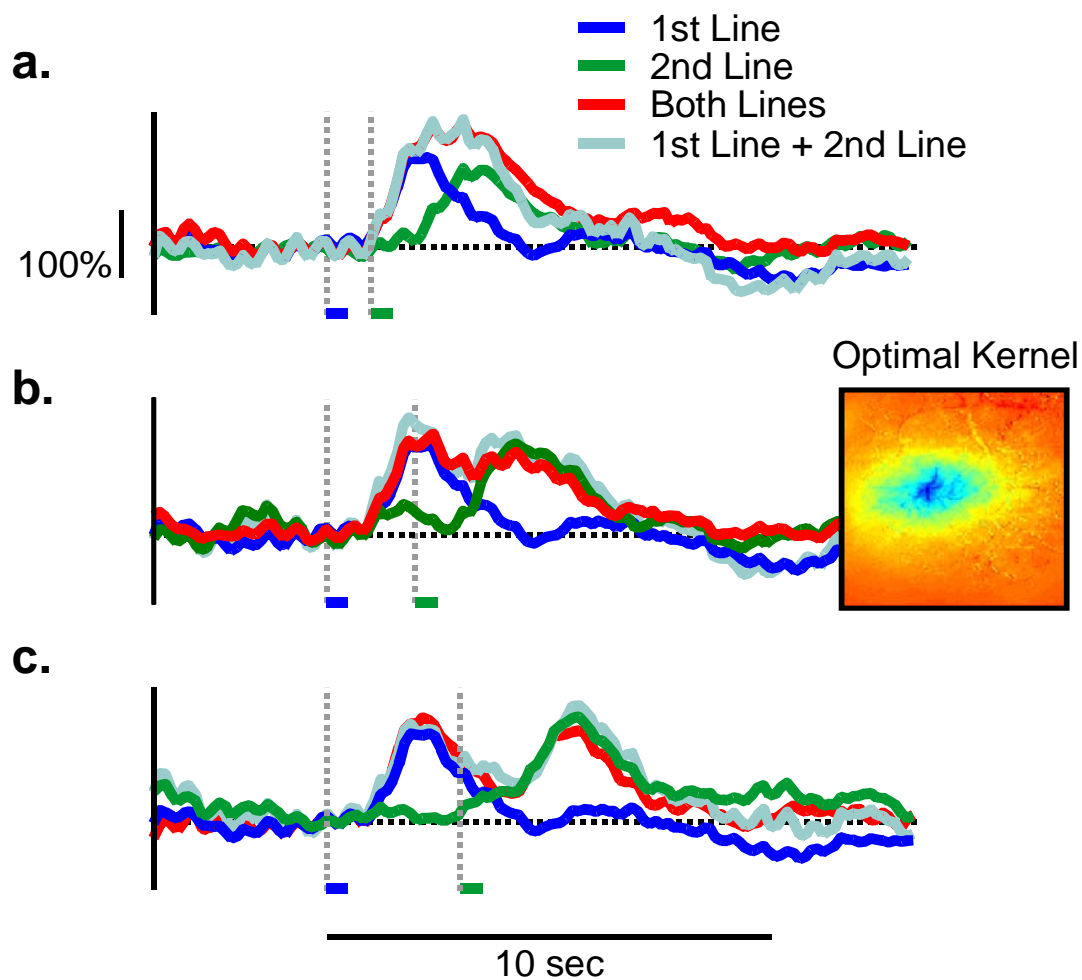


**Figure 2.9. Changes in blood volume summate linearly in time.**

Short  $0.25^\circ$  lines were flashed for 500 msec with different inter-stimulus-intervals (ISIs) and alone at the different times. **a-c.** Regression slope for the optimal response kernel (inset) as a function of time as the ISI increases from 1 to 2 to 3 seconds respectively. Note the close correspondence between response when both lines were flashed (red) and the sum of responses to the individual lines (gray).

### **2.2.5. Changes in HbT are a Linear Function of Neuronal Activity in the Fixating Animal**

Recently, we started doing experiments with simultaneous optical imaging and electrophysiological recordings. This allowed us to examine whether stimulus-driven HbT responses are linearly correlated with the underlying neuronal activity. We found that neuronal responses to full-field gratings generate predictable trial-by-trial patterns of HbT responses with high  $R^2$  values (Figure 2.10a). A small visual stimulus centered at the electrode recording site generated a broad response profile with a high  $R^2$  value at the electrode tip and progressively weaker  $R^2$  values at locations away from the locus of neuronal activity.

In the anesthetized rat somatosensory cortex, HbT signals are linearly related to changes in neuronal activity evoked by electrical stimulation [24]. To examine the linearity of HbT across different levels of spiking activity in the alert monkey V1, we presented the animal with full-field gratings of varying contrast ( $4 \log_2$  units + zero) across trials. Both multiunit (MUA) and HbT responses initially increased with contrast, but saturated at higher levels (Figure 2.10b). Plotting MUA vs. HbT showed a good linear relationship between the two signals (Figure 2.10c,d).

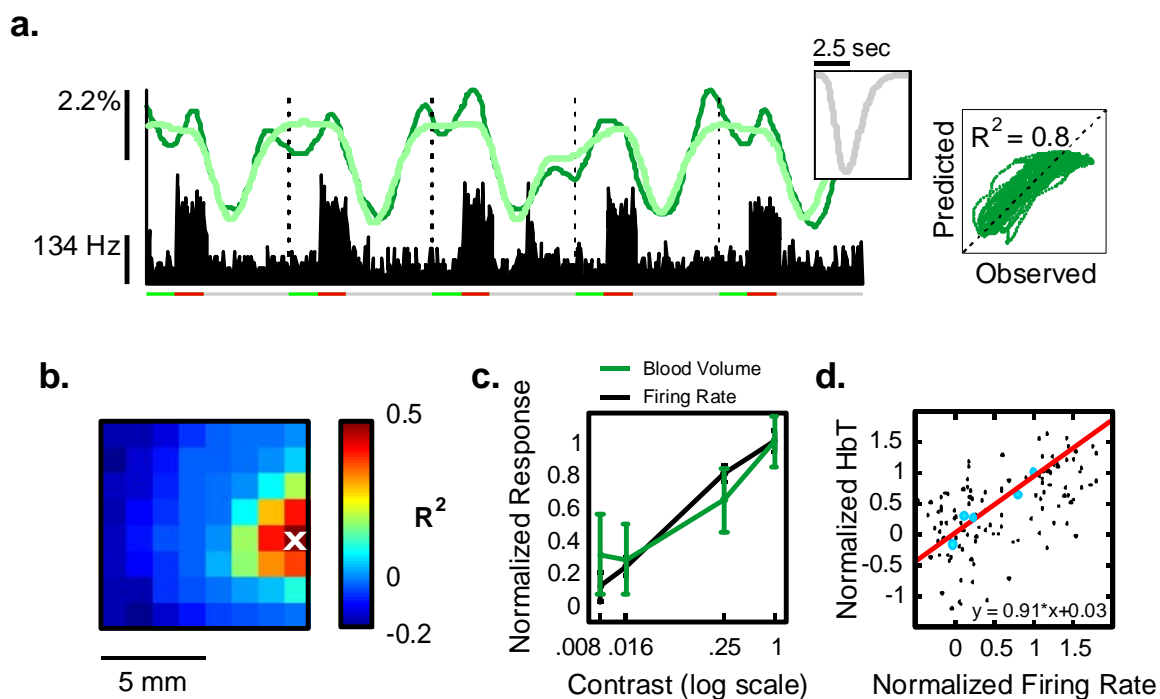


**Figure 2.10. Stimulus-driven blood volume responses are linearly related to underlying neuronal firing.**

**a.** Simultaneously acquired multiunit spike activity (histogram below; MUA) was used to predict the blood volume response (dark green; 530 nm). An optimal kernel (inset; see methods) was fitted and convolved with the neuronal trace to generate a prediction of the hemodynamic response (light green). The prediction captured most of the variance in the hemodynamic response assessed by regression (high  $R^2$ ; inset far left). **b.** For a short line ( $0.25^\circ$ ) presented at the retinotopic position corresponding to the recording site (white cross), the  $R^2$  between blood volume and spiking fell off with cortical distance. **c.** Both spiking and blood volume responses grow log-linearly as grating contrast was varied across 4-log units. **d.** Trial-by-trial scatter plot of spiking vs. blood volume responses (black circles) and the mean responses for each contrast (blue circles). Red line: the best linear fit to the data shows a good linear relationship between neuronal and blood volume responses with a slope near one and an intercept near zero.

### **2.3. Discussion:**

#### **2.3.1. Blood volume is a robust, spatially precise, and tuned indicator of neuronal activity.**

To establish an appropriate spatial marker of neuronal activity to assay cortical function in alert animals we compared the fine spatial response characteristics of two intrinsic optical signals (blood volume and oxygenation changes) for the first time in alert primates. Investigations using full-field stimuli in anesthetized preparations have suggested that the initial dip present at 605 nm may be a better marker of neuronal activity due to its presumed direct link with local changes in neuronal respiration. We found that despite vascular origins, the blood volume signal appears to be tightly linked with underlying neuronal activity in alert animals as evidenced from its accurate functional localization, fine spatial tuning, linear temporal summation, and a linear relationship with underlying neuronal activity.

#### **2.3.2. The spatial extent of the pointspreads measured across imaging wavelengths do not differ.**

We find that the spatial extent of the pointspread measured at 530, 605, and 630 nm are the same in the early phase of the responses (at the time of the initial dip). On the basis of some prior work [22, 25], we may have expected significant worsening in the spatial specificity in HbT several seconds after stimulus presentation due to non-specific recruitment of large arterioles. However, we

find that the shape of the spread at 530 nm remains invariant for at least 4 seconds after the stimulus and stays highly localized for the full duration of the response (15 sec). At later times we do see a larger recruitment in arteriolar and venous compartments, however, these increases in absorption do not distort the overall pattern and any effects in larger venous and arterial compartments can be removed by masking out large vascular compartments (Figure 2.4b).

Our results also demonstrate that the choice of wavelength to use for spatially localizing neuronal activation should depend largely on the expected signal to noise (which is higher at 530 nm) because of the similarity in the pointspreads across wavelengths. If imaging is undertaken at a single wavelength, given the relative weakness of the initial dip observed at 605-630nm and the reduced spatial specificity of the rebound, we suggest that isosbestic wavelengths measuring HbT are a better choice for localizing neuronal activity.

### **2.3.3. Blood volume likely contributes to the optically measured initial dip.**

We found that optically measured oxygenation signals at 605 nm are substantially influenced by local changes in blood volume. The size of the initial dip was larger, relative to the rebound, at 605 nm as compared to 630 nm even though at 630 nm HbR accounts for a larger fraction of the total absorption. At the peak of the initial dip measured at 605 nm (just 1 second after stimulus

presentation) we could reliably detect increased absorption in local arterioles that agreed well with concurrent absorption increases at 530 nm and were a sizeable fraction of the overall absorption at 605 nm. Given that the spatial extent of the pointspread during the initial dip at both 605 and 630 nm was similar to the pointspread measured at 530 nm, it is likely that a large part of the initial dip measured at 605-630 nm results from concurrent increases in local blood volume [15].

Given the short-lived nature of the initial dip, it is surprising that functional tuning for both oxygenation differences [8] and signals measured at long wavelengths [35] maintain the same phase throughout the response time-course, even during the rebound. This phenomenon has been interpreted as “watering the garden,” *i.e.* that the vascular system does not provide spatially specific resources in response to spatially specific demand.

In agreement with past results, we find that the rebound is more spatially distributed than the initial dip (Figure 2.4, j-k). However, there is confusion about the relationship between the spatially specific dip and the diffuse rebound. Unlike rebounds measured using optical imaging, rebounds measured using fMRI (the primary BOLD signals measured using MR, [45]), show proportional increases with increased neuronal activity even for individual orientation domains [23]. This is in direct conflict with the “watering the garden”

hypothesis. We found that, unlike the initial-dip or blood volume, the rebound signal actually peaked away from the center of the pointspread. This would be expected if the rebound signal was a combination of increased absorption due to increased blood volume and a decreased absorption due to the increased flow-through of oxygenated blood. We believe, therefore, that the long-lasting increase in absorption at 605-630 nm wavelengths results from local increases in blood volume.

#### **2.3.4. Blood Volume Likely Accounts for the Post-Stimulus Undershoot**

As observed commonly in fMRI and in some optical imaging studies [46], in addition to the initial-dip and rebound, BOLD signals can show a prominent post-stimulus undershoot. The origins of this undershoot are debated in the literature [47, 48]. In signals at both 605 and 630 nm, we commonly observed a post-stimulus undershoot localized to the stimulated site though the phenomenon was stronger and more common at 605 nm. Our finding of a long-lasting focal increase in at 530 nm and the demonstrated contribution of this signal to signals gathered at 605 nm is consistent with the idea that this post-stimulus undershoot is due to residual blood volume at the activated area [47] and not increased oxygen metabolism [48].

#### **2.3.5. The Push-Pull Nature of the Initial Dip**

As demonstrated above, the size of the initial dip is dependent on the spatial distribution of stimulus driven activity and how well it can be compensated for by the rebound. Oriented gratings evoked prolonged 'dips' at iso-oriented columns that lasted as long as the blood volume responses (Figure 2.7) whereas small points, adequately spaced, generated spatially discernable rebounds and short-lived dips (Figure 2.8) even when the distance between the stimulated cortical areas was less than 300  $\mu\text{m}$ .

These properties make it difficult to compare the profiles of activity evoked by spatially restricted stimuli because the magnitude of the 'initial dip' at each point is increased by the local metabolic demand but decreased in proportion to a broader spatial average of the demand, thus acting as a sort-of high-pass filter (underlying metabolic activity convolved with the relatively fatter rebound kernel subtracted from the same activity convolved with the relatively thinner dip or volume kernel).

### **2.3.6. Distinguishing Stimulus-triggered from Trial-related signals**

As demonstrated, the blood volume signal carries a larger stimulus-related signal than signals at 605 nm, but a large fraction of the variance in both signals cannot be attributed to visual stimulation (Figure 2.3). In alert animals engaged in tasks, there are confounding signals that simply reflect the hemodynamic activity patterns associated with performing the task.

For example, an animal sitting in a dark recording booth may be required to periodically fixate on a dim monitor. Fixating a relatively bright object may, in itself, act as a stimulus, produce a response in V1 and confound any interpretation of responses to visual stimuli subsequently displayed on the monitor. In order to account for these confounds, it is important to measure responses on trials when no stimulus is presented. The difference in the activity patterns between trials with *vs.* without a stimulus presented are a better measure of the stimulus-specific response and we will use these responses whenever we refer to stimulus-related activity in Chapter 4.

In addition to extrinsic sources of trial-related variability, even in anesthetized animals, there is ongoing vascular activity with a typical frequency of 0.1 Hz. Such oscillations in blood volume and oxygenation have been associated with *vasomotor activity* observed in peripheral vessels [34, 49]. Vasomotor activity has been observed in many preparations; including rats, awake monkeys, and humans. This activity pattern is of large amplitude, comparable to stimulus-evoked signals, and confounds stimulus-triggered averages. However, as discussed in detail in the next chapter, in the alert animal, the vascular activity plausibly underlying these signals have a constant relationship to the temporal structure of trials, making it possible to remove them using the aforementioned procedure.

## **2.4. Methods**

Results were obtained using continuous, intrinsic-signal optical imaging at two wavelengths in two monkeys engaged in a visual fixation task. On each trial, the animals were simply required to hold fixation on a small fixation point (0.08-0.15 deg, fixation window 0.75 deg) over a cued duration (at least 4 sec) for a juice reward, ignoring any visual stimuli shown during the cued fixation period. Eye position was monitored with an infrared tracker[50]. Note that all the optical imaging data reported here were obtained in the naive animals, prior to psychophysical testing.

### **2.4.1. Optical imaging: Surgery, recording chambers, artificial dura:**

After the monkeys were trained on visual fixation tasks, craniotomies were performed over the animals' V1 and glass-windowed stainless steel recording chambers were implanted, under surgical anaesthesia, using standard sterile procedures[17]. The exposed dura was resected and replaced with a soft, clear silicone artificial dura. After the animals had recovered from the surgery, cortical activity from their V1 was optically imaged through this recording window, routinely, while the animals engaged in relevant behavioural tasks. Recording chambers and artificial dura were fabricated in our lab using published methods[51].

### **2.4.2. Optical imaging: Data acquisition**

Standard alert-monkey optical imaging techniques[17] were used. Images were acquired on a Dalsa 1M30P camera (1024 x 1024, 30 frames / sec, but typically binned to 256 x 256, 15 frames / sec), through a Optical PCI Bus Digital Frame Grabber (Coreco Imaging, Boston MA) imaging board, using software developed in our lab based on a system by V. Kalatsky[52]. Illumination was provided by high-intensity LEDs (Agilent Technologies, Purdy Electronics), synchronized to the camera acquisition frames (Appendix I). We used LEDs centred at 530 nm (close to an isosbestic point for Haemoglobin, i.e. absorbed equally in oxygenated and deoxygenated Haemoglobin) acquiring images at a frame rate of 7.5 frames / sec. The light from the LEDs was filtered through small individual interference filters (Omega Optical) mounted on each LED. A 'macroscope' of back-to-back camera lenses[53] (Nikon, assorted fixed focal lengths), focused on the cortical surface, was used for imaging. Images of the cortex were acquired at 7.5 Hz and combined into movies.

The monkeys were trained to maintain fixation for at least 4 seconds, during which, line stimuli were presented for 1-1.5 seconds at  $\sim 3^\circ$  eccentricity in the lower visual field (inter-stimulus-interval  $\geq 18$  seconds).

### **2.4.3. Optical Imaging: General Data Analysis Steps**

The images were processed using custom software written in MATLAB (Image Processing Toolbox). All images were first 'shift-corrected' to correct for any residual movement of the cortical surface that remained despite the specially

designed camera mount, animal head post and overall structural framework.

This 'shift-correction' consisted of aligning each image frame to the first frame of a given experimental session, using the imaged blood vessels as references. Each image frame was cross-correlated with the reference frame, and a gradient descent method used to maximize this correlation value as a function of lateral shifts in the image position, frame by frame. These 'shift-corrected' images were then used for all subsequent processing.

The functional data was analyzed as follows. For each stimulus condition and trial, we generated a movie of the average cortical activity changes triggered on the onset of the stimulus. The data were temporally low-pass filtered (cut-off frequency of 1Hz) to remove the pulse artefact. To compensate for the uneven illumination over cortex each image frame was divided by a spatially low-pass filtered image of the overall cortical reflectance. The pre-stimulus period was then subtracted on a trial-by-trial basis (5 frames immediately prior to stimulus onset), thus giving us a measure of percent signal change. From each stimulus-triggered movie, we subtracted the blank trial average movie to remove non-stimulus related hemodynamic patterns. To generate images of activity patterns associated with each stimulus, we averaged 10 frames around the peak of the stimulus related activity (typically 3 seconds after stimulus onset).

#### **2.4.4. Optical Imaging: Regression Analysis of Response Timecourse**

Since the stimulus driven response at 530 nm is largely invariant in shape across its timecourse, it is possible to remove noise from the image timeseries via regression. The average stimulus-triggered response is first computed at a point with maximal signal to noise (i.e. at the peak of the response ~3 sec after stimulus onset). This image is then used as a regressor across the full timeseries. The slope of this regression indicates how well the pattern observed at any point during the movie matches the average stimulus-triggered response (Figure 2.9).

#### **2.4.5. Electrophysiology: Hardware, electronics and analysis:**

All spiking and LFP data were acquired using a Plexon data acquisition system (Plexon Inc.) with either plastic coated tungsten electrodes (FHC Inc.) or, for Monkey V, homemade glass coated tungsten electrodes with impedances ranging from 300 K $\Omega$  to 800 K $\Omega$ . Penetrations were made through a small hole drilled in the glass cover of the imaging chamber allowing for simultaneous acquisition of electrophysiological and imaging data. Recordings were made sampling depths ranging from most superficial to ~1500 microns below the pial surface ('blindly' by advancing the electrode in 200 - 400 micron steps after first encountering multiunit 'hash') over multiple V1 location at an average visual eccentricity of ~2 degrees. Recording was run continuously and was aligned to the imaging data using custom software (written using MATLAB).

We contrasted the visually driven responses with dark-room responses quantitatively by comparing, in each case, the measured haemodynamic signal with a signal predicted using the corresponding MUA response. For each recording site we first fit the stimulus-driven haemodynamic response to the MUA, trial by trial, by calculating the optimal haemodynamic kernel for the pair using a simplex-based algorithm (see later Section 3.4.9: Fitting to Haemodynamics). We then convolved the kernel with the stimulus-evoked MUA and the dark-room MUA to calculate, in each case, a “predicted” haemodynamic signal. For visually driven trials the predicted haemodynamic signal fit the measured signal very closely, trial by trial, with high values of  $R^2$ .

#### **2.4.6. Electrophysiology: Data processing:**

All spiking data was binned into 16 msec bins (the frame period for the imaging camera) and aligned to the haemodynamic traces using simultaneously recorded synch events. LFP data was spectrally decomposed using `mtspecgramc` (Chronux Toolbox for MATLAB; sliding window of 1 sec, a step size of 250 msec, frequency range from 10 to 130 Hz) and interpolated into a continuous power spectrum aligned to the haemodynamic traces. Frequencies from 56 to 64 Hz were excluded from analysis to avoid any artefacts due to line noise.

#### **2.4.7. Electrophysiology: Fitting to Haemodynamics:**

For each recording site, we obtained simultaneous spiking and haemodynamic responses to trials on which a visual stimulus was presented as well as trials

done in complete darkness. Correct trials were extracted from the continuous time series and concatenated into a synthetic series with only correct trials. We modelled the haemodynamic response function (HRF) with a gamma kernel of the form:  $HRF(t, T, W, A) = A * \left(\frac{t}{T}\right)^\alpha * \exp\left(\frac{t-T}{-\beta}\right)$ ; where  $\alpha = (T/W)^2 * 8.0 * \log(2.0)$ ,  $\beta = W^2 / T / 8.0 / \log(2.0)$ , and  $K$  is the amplitude,  $T$  is the time to peak, and  $W$  is the full width and half maximum. We fit the kernel parameters using a downhill simplex algorithm (fminsearch, MATLAB) by comparing the actual haemodynamic response obtained during stimulated trials to that predicted from a convolution of the HRF with the corresponding spike trace. The algorithm reliably converged to similar temporal HRF parameters across all days ( $T=2.50$  (0.08) sec,  $W = 1.68$  (0.06) sec). The proportion of the variance in the haemodynamic responses explained by neuronal activity was quantified using the  $R^2$  statistic from linear regression of the predicted haemodynamic trace to the observed trace for both the stimulated and the dark room trials (Figure 2.12).

#### **2.4.8. Stimuli**

Stimuli were composed using custom software written in MATLAB (MathWorks, Natick MA) and presented using custom software (BehavCtrl; Appendix II) written for use with the VSG (Cambridge Research Systems, Kent England) graphics co-processor and an A-D board (National Instruments, Austin TX). During optical imaging, to assure that the long-lived hemodynamic response to a stimulus from the preceding trial does not interact with future responses we

interjected a 6 second inter-trial interval along with blank trials (trials with no stimulus presented) between each stimulus-containing trial. During the course of any experiment, we also included additional blank trials on which a stimulus was not presented that were likewise flanked on either side by blank trials. These were used to compensate for the overall trial-related pattern of the hemodynamic response (see below).

All experimental procedures were performed in accordance with the NIH Guide for the Care and Use of Laboratory Animals and were approved by the Institutional Animal Care and Use Committees (IACUC) of Columbia University and the New York State Psychiatric Institute.

## Chapter 3.

### ANTICIPATORY VASCULAR SIGNALS IN SENSORY CORTEX

#### *3.1. Introduction to the Chapter*

In functional brain imaging the underlying haemodynamic signals are typically assumed to reflect local cortical metabolic demand correlated with neuronal activity. As described earlier, our dual-wavelength optical imaging technique allows us to simultaneously measure cortical oxygenation and blood volume in alert behaving monkeys. To our surprise, we found a large hemodynamic signal in V1 present even on trials when no stimuli were presented to the animal. To understand the relationship of this signal to local neuronal activity, we conducted experiments combining optical imaging with simultaneous electrophysiology.

This chapter characterizes, in detail, our observed signal. We find that the signal, comparable in amplitude to vigorous visual stimulation, is present even in total darkness. The signal amplitude reflects the animals' behaviour, being correlated with fixation performance. Further, the signal provides evidence of anticipatory timing in the brain. Given a predicted event, the brain prepares for action by pumping in fresh arterial blood in anticipation of the upcoming event, before any increased spiking or metabolic demands. Our findings reveal a

predictive, modality-specific arousal mechanism in the brain and challenge the current understanding of brain haemodynamics.

### ***3.2. Unexpected Discovery of Trial-Linked Anticipatory Signals in V1***

As mentioned earlier, functional brain imaging is based on the assumption that cerebral blood volume (CBV) and oxygenation levels reliably measure the metabolic demand from local neuronal activation [5, 39, 54-56]. Most current imaging techniques have not tested this assumption because they cannot measure CBV and oxygenation independently (except in anesthetized animals [14, 57]). Thus functional magnetic resonance imaging (fMRI) commonly uses the blood oxygen level dependent (BOLD) signal [58] which correlates with changes in deoxyhaemoglobin ('HbR') concentration. This signal is widely understood to reflect local changes in blood oxygenation, i.e. the ratio of HbR to the concentration of oxygenated haemoglobin ('HbO') even though, as discussed in Chapter 2, it is recognized that the signal results from a complex interplay of changes in oxygenation, volume, and blood flow[5] (which BOLD fMRI cannot measure independently). Similar caveats apply to imaging techniques that measure early stimulus-triggered increases in HbR concentration ('initial dip') on the premise that this reflects a rapid local conversion of HbO to HbR at foci of neuronal activity[59, 60].

To probe the links between blood oxygenation, blood volume and neuronal activity we developed a technique for independently measuring cortical HbO

and HbR concentrations in alert, behaving macaque monkeys. The technique is based on imaging the cortical surface using two sets of light emitting diodes (LEDs) at two spectral wavelengths (Figure 2.11a). One wavelength, 530 nm (green), an isosbestic point for haemoglobin (Hb)[38], i.e. absorbed equally by HbO and HbR, measures the total haemoglobin concentration ('HbT' = HbO + HbR, proportional to local CBV, assuming a constant haematocrit). The other wavelength, 605 nm (red), being absorbed ~ 5-fold more strongly in HbR than HbO gives a measure of blood deoxygenation, albeit combined with changes in HbT concentration. By switching between the two sets of LEDs in alternate frames of our imaging camera (15 Hz), much faster than mean haemodynamic responses, this method images the cortex in effect simultaneously at both wavelengths (at 7.5 Hz. **Methods**). Further, by imaging continuously it monitors changes in local HbT concentration and oxygenation state through all phases of behavioural tasks and changes of brain state.

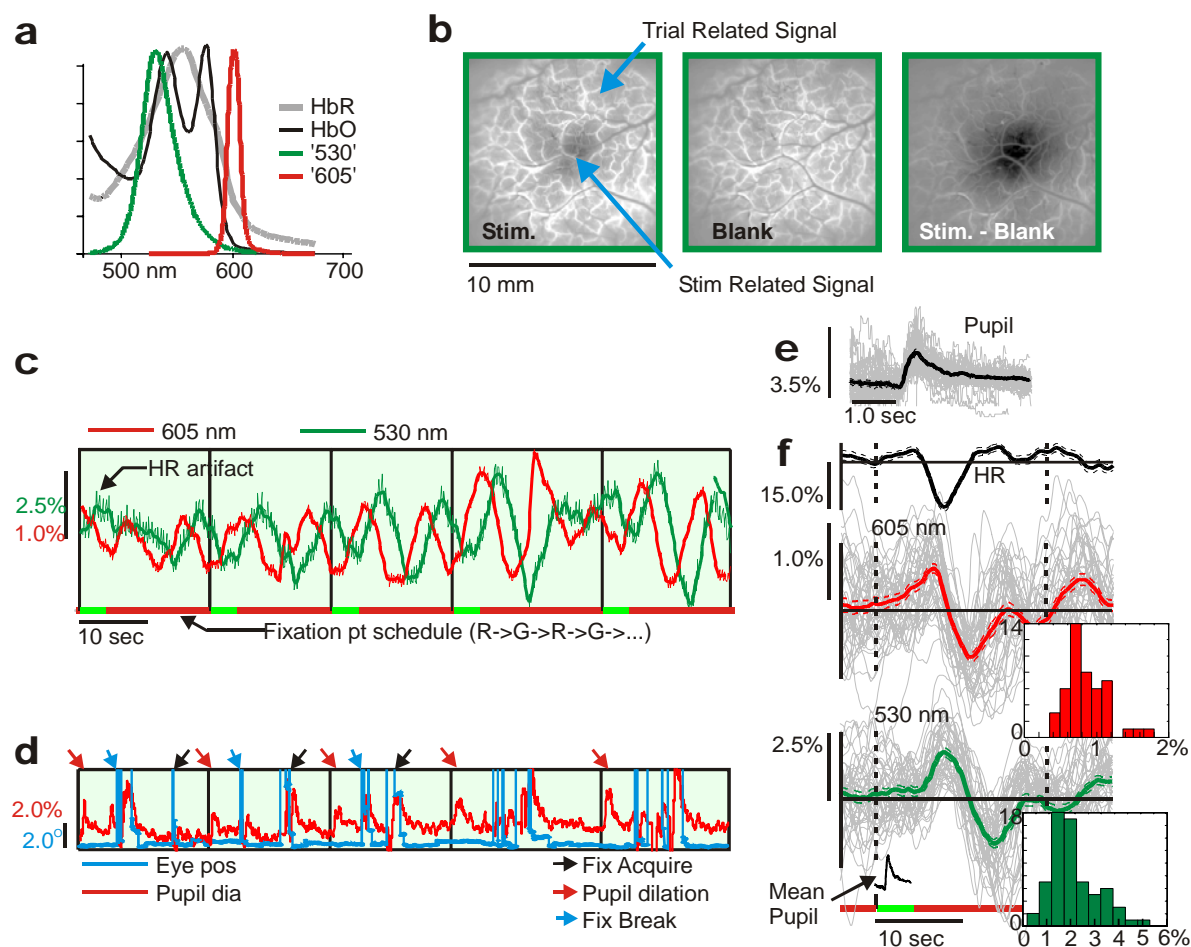


**Figure 2.11. Periodic trials evoke stimulus-independent, trial-linked signals even in the dark.**

**a:** Normalized emission spectra of the 2 LEDs used for dual-wavelength optical imaging, superimposed on standard [38] *in vitro* absorbance spectra for HbR and HbO (units of  $10^4 \text{ cm}^{-1}/\text{M}$ ). **b:** 'Stim': Imaged (530 nm) V1 response to a small flashed visual stimulus ( $0.25^\circ$  bar, 1 sec). Showing image frame 3.3 sec post stim onset); 'Blank': Same, in blank trial showing stim-independent response (same time point post 'blank' stim). 'Stim-Blank' reveals retinotopically localized stim-specific response. (Imaged V1 area covers visual eccentricity  $\sim 1^\circ$  to  $5^\circ$ ). **c:** Continuous recording of the mean cortical signals in the dark-room task. 'Fixation pt schedule' indicates fixation cue: red: 'intertrial interval'; green: 'trial on' i.e. 'fixate'. Vertical black lines: trial onsets. Colour coding (green=530 nm, red=605 nm). Same conventions used in all figures. HR (heart rate) artifact. There was an intentional 20% jitter in trial timings, to prevent coinciding

accidentally with any intrinsic signal periodicity. (See Figure 2.27, Methods). **d**: Continuous recording of eye position (radial distance from fixation, deg) and pupil diameter (% change around mean diameter), aligned in time with the cortical signals in c. Note the pupil dilations (red arrows) at trial onsets. Only first three sets of fixation break / acquire marked with arrows, to avoid clutter. In c, d: scales colour-coded. **e**: Pupil traces, aligned to trial onsets: gray: individual traces; black: trial-triggered mean. Note expanded time scale. **f**: HR and cortical responses aligned to trial onsets (dashed vertical lines) shown for same experiment as in c, d: correct trials only (i.e. maintained fixation: n=51 out of 102 total). Gray lines: individual trials; thick lines: trial-triggered mean, +/- 1 SEM (605 nm: peak to peak amplitude: mean 1.19% +/- 0.08 SEM; 530 nm: 3.47% +/- 0.21 SEM). The mean pupil dilation shown inset, aligned on fixation schedule. Inset histograms: population distributions of mean peak to peak amplitudes (605 nm: mean=0.86%, std=0.29, N=47 experiments. 530 nm: mean=2.17%, std=0.97, N=66. Higher number of experiments at 530 nm than at 605 nm since most of the simultaneous electrophysiology and optical imaging was done at 530 nm. Smaller signal values, particularly at 530 nm, could be an artefact: see Figure 2.20; See Methods for more details).

While our purpose in developing dual-wavelength optical imaging was to better quantify the links between local neuronal activity and haemodynamics (see Chapter 2) we discovered a novel trial-linked haemodynamic response apparently not driven by local neuronal activity through any presumed metabolic mechanisms (e.g. [55]). We saw evidence for this novel response on first imaging V1 in alert monkeys using our dual-wavelength technique. There were two distinct components to signals recorded during any periodic visual task (Figure 2.11, b). One component was restricted spatially to the retinotopic

location of the visual stimulus on V1 and synchronized to stimulus onset. The other component – consistently present on every trial whether with a visual stimulus or a blank screen (Figure 2.11, b, 'Blank') – activated the entire imaged area of V1 and synchronized with trial onset rather than the stimulus.

To study this trial-related signal we then developed a periodic dark-room task that eliminated any confounding visual drive. In a completely dark room, with a mask covering even the background glow of the stimulus presentation monitor, the animal had to attend to a tiny fixation point visible through a pinhole in the mask (pinhole size  $\sim 0.5$  mm diameter, corresponding to 1-2 arc min, i.e. about 1-2 cone diameters. The stimulus was akin to seeing nothing besides one single twinkling star in an otherwise black night sky. We confirmed that nothing else was visible by dark adapting in the room as long as the animal). The fixation point stayed on continuously, cueing trials by switching periodically between equiluminant red ('intertrial interval') and green ('trial on;' Figure 2.11, c). The animal's task was simply to maintain fixation (window radius  $0.5^\circ$ ) while the trial was on, for a juice reward. Eye position and pupil diameter were monitored using infrared eye trackers. Two rhesus macaque monkeys ('V' and 'S') were trained on the dark-room task in addition to their full repertoire of visually stimulated tasks. We imaged the animals' V1 continuously while they performed this task.

### 3.2.1. V1 responds to periodic fixation task in the dark.

Once the animals had learned the dark-room task, we consistently saw prominent trial-linked V1 signals during periodic fixation trials (Figure 2.11, c). Despite being in virtually total darkness, signal amplitudes were comparable to those evoked by powerful visual stimuli that vigorously activate a large fraction of V1 neurons. (e.g. optimal grating-evoked signal amplitudes of ~2-3% at 530 nm in anesthetized cat V1 [7], ~1% at 605 nm in alert monkey [17]). The animals' eye fixation routine showed that they had learned the task correctly (Figure 2.11, d). Both monkeys would perform long sequences of correct trials, consistently holding fixation during the cued trial period and taking fixation breaks, if any, only during inter-trial intervals. This was accompanied by a sharp dilation of the animals' pupils on trial onsets (Figure 2.11, d, e) further suggesting a rhythmic state of alertness synchronized finely with each trial [61].

All measured signals synchronized well with the trial onsets, trial by trial, giving robust trial-triggered averages. This can be seen for the pupil dilation (Figure 2.11, e), for the cortical signals measured at 530 and 605 nm (Figure 2.11, f), as well as for the animal's heart rate (HR, Figure 2.11, f) measured off a heart beat artefact in the optical signal (see Figure 2.11, c). This basic finding – of systematic prominent cortical, HR and pupil signals synchronized to trial onset – was seen in every experiment conducted in either animal once they started performing reliably (Figure 2.11: N=66 experiments total: 54 in monkey 'S', R hemisphere; 12

in monkey 'V': 11 in L hemisphere + 1 in R hemisphere. Data from monkeys V and S were statistically indistinguishable and thus combined in the population data in Figure 2.11. See Figure 2.18, Figure 2.19 at the end of the chapter).

### **3.2.2. Dark room signals are not predicted by local neuronal activity in V1.**

Electrode recordings made simultaneously with the optical imaging (Figure 2.21, a; Section 3.4) failed to reveal any V1 neuronal activity in the dark room that could underlie the trial-related haemodynamic signals. Multi unit spiking activity [54, 57] (MUA) and local field potentials (LFP - whether in the gamma frequency band [54, 62], or rectified and integrated overall [14, 57]) have variously been shown to be good predictors of haemodynamic signals evoked by local neuronal activity. We therefore recorded MUA and LFP concurrently with optical signals from 24 sites sampling a range of cortical depths in 9 separate penetrations across imaged V1. All signals were recorded while the animal performed simple cued periodic fixation tasks. In alternating blocks - as the animal fixated - he got either vigorous visual stimulation (gratings optimized to evoke maximal neuronal firing; filling the imaged region unless otherwise specified) or just the fixation cue in the dark room.

At each recording site, despite robust dark-room haemodynamic responses, the concurrently recorded electrophysiological signals were weak and, at best, poorly correlated with haemodynamics - dramatically unlike visually stimulated signals (Figure 2.12, a, b). The visually driven MUA at each site reliably predicted

the simultaneously recorded haemodynamics and fits between the two signals yielded consistent haemodynamic kernels (Figure 2.12, b). Convolving the dark-room MUA with the same kernels, on the other hand, generated very poor predictors of the dark-room haemodynamic responses, low in amplitude and temporally uncorrelated with the measured signal ( $R^2 \sim 0$ ; Figure 2.12, b, c; Section 3.4). Kernels derived from the dark-room response did not improve the match significantly (Figure 2.21, b). At a fine spatial scale, dark-room haemodynamic signals measured locally over V1 were uniformly poorly correlated with the dark-room predictor, with weak  $R^2$  overall and no hot spot around the electrode recording site (Figure 2.12, d). By contrast, visual stimulation (a small grating stimulus centred at the electrode) gave high  $R^2$  sharply peaked around the recording site.

The poor prediction of the dark-room signal cannot be due to nonlinearities in the spike-to-haemodynamics transfer function. Such nonlinearity – while arguably explaining the weak amplitude – cannot account for the poor temporal correlation. Further, independent recordings using grating stimuli ranging over 5 log units of contrast, made specifically to test for linearity of the transfer function, gave haemodynamic signals that were linearly correlated with MUA over the entire recorded range (figure not shown).

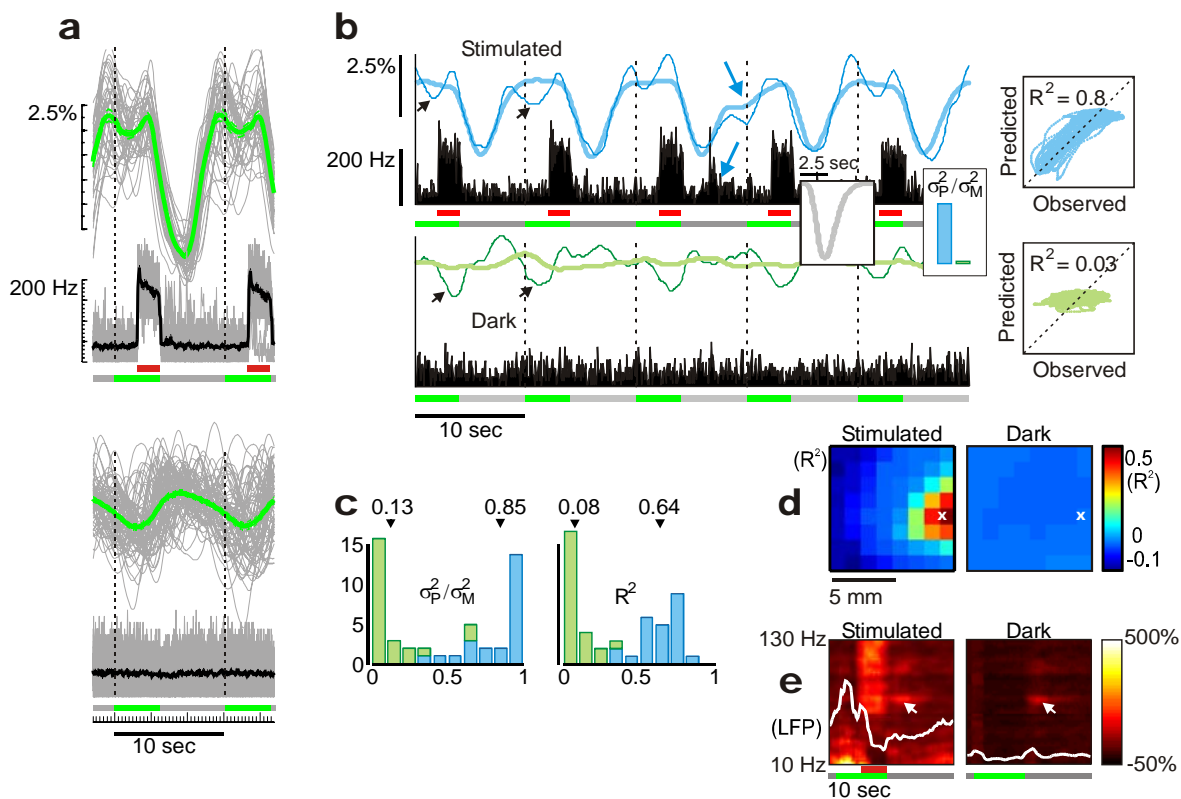


**Figure 2.12. Trial-linked signals in dark room, unlike visually evoked signals, are not predicted by local neuronal activity.**

**a: Top:** 530 nm signal (green) and MUA (black) evoked by strong visual stimulation (100% contrast sine grating, 4 deg/cycle, 2 deg diameter, drift speed = 4 deg/sec. N=42 trials). Green line below the MUA trace: fixation on; red: stimulus on. **Bottom:** same, for dark-room fixation task. (N=73 trials). **b: Top:** a sequence of spiking (black: bin = 66.7 msec) and measured hemodynamic responses (thin blue) during visually driven trials. Same experiment as part a. Thick blue: predicted hemodynamic response, calculated by convolving spike response with optimal hemodynamic kernel calculated for this recording site (inset, gray. The fit at each recording site yielded hemodynamic kernels that were similar in latency, shape and duration. See methods). Good tracking overall between predicted and measured hemodynamic signals, including deviations due to unexpected bursts of spiking (blue arrows); but poor tracking near the start of each trial (black arrows).  $\sigma_P^2 / \sigma_M^2$ : ratio of the variance of the predicted hemodynamic signal / variance of the recorded hemodynamic signal, as a measure of the

goodness of amplitude prediction ( $=1.1$  for the visually driven signal). **Box:** scatter plot of predicted vs. measured haemodynamic signal, showing regression line and  $R^2$  ( $=0.8$ ). **Bottom:** same, for dark room trials: Thin green: measured haemodynamic; thick green: predicted haemodynamic, calculated by convolving the same kernel over the dark-room MUA. Note the prominent trial-linked fluctuations (black arrows) that line up well, in trial phase, with regions of poor prediction for the visually driven signal above.  $\sigma_P^2 / \sigma_M^2 = 0.013$ ,  $R^2 = 0.03$ . **c:** Population histograms of  $\sigma_P^2 / \sigma_M^2$  and  $R^2$  ( $N=24$  recording sites) showing means for visually stimulated (blue) and dark-room trials (green). **d:**  $R^2$  calculated as a function of position on cortex after subdividing the imaged area into  $8 \times 8$  identical squares. **Left:** visual stimulation (100% contrast sine grating,  $0.5^\circ$  diameter centred around electrode location 'X'; different experiment from parts a, b). The optimal haemodynamic kernel obtained by fitting the recorded MUA to the haemodynamic signal in the square containing the electrode recording site was used to estimate a predictor as in part b. This predictor was then correlated with the haemodynamic signals measured in each of the squares tiling imaged V1. Note sharp peak of  $R^2$  near the electrode (related to - but distinct from - any peak in signal amplitude), and antiphase ('negative'  $R^2$ ) in the surround. **Right:** same, for dark-room: predictor estimated by convolving the recorded MUA with the same optimal kernel as for visual stimulation (left). Note the low  $R^2$  uniform over imaged V1 with no hot spot around 'X'. **e:** Power spectrum density of the LFP, 10 Hz - 130 Hz (roughly, gamma band) normalized to a common pre-trial baseline (dark-room) for the same experiment as in parts a, b. White trace: LFP power integrated over gamma band. White arrow: artefact from licking reward tube at trial end (also seen outside trial context).

Recorded LFPs failed to give a better prediction of the dark-room haemodynamic response. This was true whether we considered the power in any of the standard frequency bands after spectrally decomposing the LFP (e.g. gamma: Figure 2.12,

e; 'delta' (0.05-3Hz), 'theta' (3-8Hz), 'alpha' (8-12Hz) or 'beta' (12-20Hz)) or simply rectified and integrated the full LFP (figures not shown); we consistently failed to find any transfer function that could reliably predict haemodynamic signals from electrophysiology for both visual stimulation and dark-room trials. These simultaneous electrophysiological and imaging results were obtained from monkey 'S.' They were corroborated by electrophysiological measurements from monkey 'V' using a similar recording regimen (Figure 2.18, f, g).

### **3.2.3. V1 signal reflects trial-locked arterial dilation.**

Visualizing the cortical distribution of the measured trial-related signals revealed a dramatic arterial contraction-dilation cycle that appeared timed to bring fresh arterial blood to cortex before each trial onset - i.e. before any trial-related neuronal spiking or metabolic demand (Note: veins and arteries are distinguished by differential absorption at 530 nm and 605 nm [18]; Figure 2.13, a, b). This arterial contraction-dilation cycle - and the cyclic change in the HbT signal ('blood volume') - can be seen by imaging the fractional change in the 530 nm signal intensity over the cortical surface as a function of time after trial onset (Figure 2.13, c, d upper row, green). Note the prominent whitening of the artery walls while the overall image is lightening (i.e. reducing HbT concentration) shortly after the end of the fixation cue (see frames at 8.0 and 10.7 sec post trial onset) followed by an equally prominent darkening of the artery walls during the darkening phase of the image (increasing HbT; frames at 13.3 and 16 sec).

The brightening and darkening artery walls reflect consecutive contraction and dilation of the artery relative to the trial mean (Figure 2.22).

At a higher magnification – in the image profile measured along a test line sampling a vein, an artery and the intervening cortex – the arterial contraction-dilation is seen riding prominently over a cyclic change in the baseline HbT signal. Both signals are synchronized to the trial period, reaching their peak – i.e. bringing a peak of fresh arterial blood to cortex – into the next trial (Figure 2.13, e, f). We consistently saw similar trial-entrained arterial contraction-dilation cycles in every dark-room imaging session, in both animals (n=66 experiments in 2 monkeys. Monkey V: see Figure 2.19).

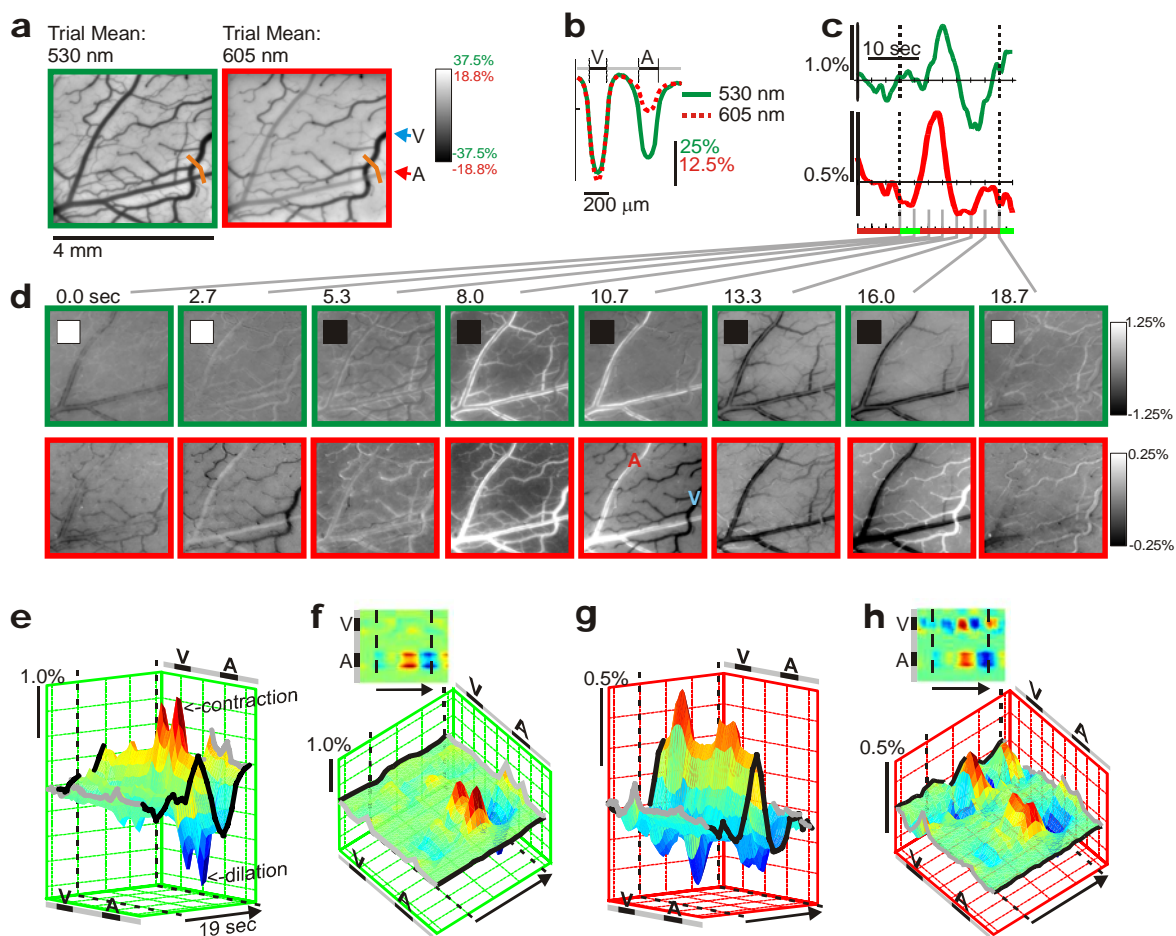


**Figure 2.13. Optical images reveal trial-locked arterial cycle bringing fresh blood to cortex before each trial onset.**

**a:** Trial mean images of cortical surface, i.e. averaged over the full 18.67-sec trial, ( $n=15$  trials  $\times$  140 frames each trial at 7.5 Hz). Arteries (e.g. 'A') identifiable as light at 605 nm, dark at 530 nm; veins ('V') as equally dark at both; 'parenchyma': rest of cortical tissue. Orange line: test line for image profiles. Greyscale: % signal deviation from the image mean. Note different scales for 530 nm (green) and 605 nm (red). **b:** Profiles of trial mean images along the test line, showing alignment with vein ('V') and artery ('A'). **c:** Mean cortical signals ( $n=15$  trials). **d:** Individual frames of image (fractional change in signal relative to trial mean: greyscale centred around individual image means) at selected time points relative to trial onset (marked on top). Small inset square at the top left corner of each frame indicates trial phase: fixation period (white) or intertrial interval (black). **e:** Image profile along the test line at 530 nm. Vertical axis: fractional

signal change; arrow: time axis (trial period: ~19 sec); 'V', 'A': mark alignment with vein, artery along test line, as in b. The same symbols used in the next 4 panels. Heavy black outline: time course of parenchyma baseline (**Methods**). **f**: Blood vessel signal relative to parenchyma, obtained by regressing away the baseline at each time point of image profile. Shown both in flat 2-d view on top and as 3-d surface below. **g**, **h**: Same, at 605 nm.

This arterial cycle was accompanied by periodic trial-linked patterns of blood oxygenation, with distinct time courses in veins, arteries and 'parenchyma' (cortical tissue other than resolvable veins or arteries). This is evident in the 605 nm image (Figure 2.13, c, d lower row and Figure 2.13, g, h; compare 'A', 'V' in 10.7-sec frame, Figure 2.13, d lower row). Here the interpretation is more complicated since lightening primarily implies decreased HbR concentration, which could be due to either increased oxygenation or to decreased blood volume. The relative contributions of these two effects can be obtained only by solving quantitatively for the concentrations of HbR and HbO [63, 64] (manuscript in preparation). Qualitatively it is clear, however, that the signal in the vein was due to changing oxygenation alone. There was no venous signal at 530 nm, i.e. no changes in the venous HbT concentration relative to parenchyma. Thus the venous signal at 605 nm reflected changes in the ratio of HbR vs. HbO, with darkening implying enrichment by HbR relative to HbO with fixed HbT (e.g. Figure 2.22, b).

The measured vascular signals, though different in artery, vein and parenchyma, were global over the entire imaged area of V1 independent of retinotopic location. In particular, the arterial contraction-dilation cycle engaged the entire arterial system over the full imaged V1 (Figure 2.14, a, b; visual eccentricity  $0.5^{\circ}$  to  $4.5^{\circ}$ , over 10 mm of cortex. The fovea, the only locus of visual stimulation, is outside the imaged area.). This homogeneity of the trial-linked signal over V1 contrasted dramatically with the sharply peaked, spatially localized image of stimulus-evoked activity over the same part of cortex (Figure 2.14, c, d).

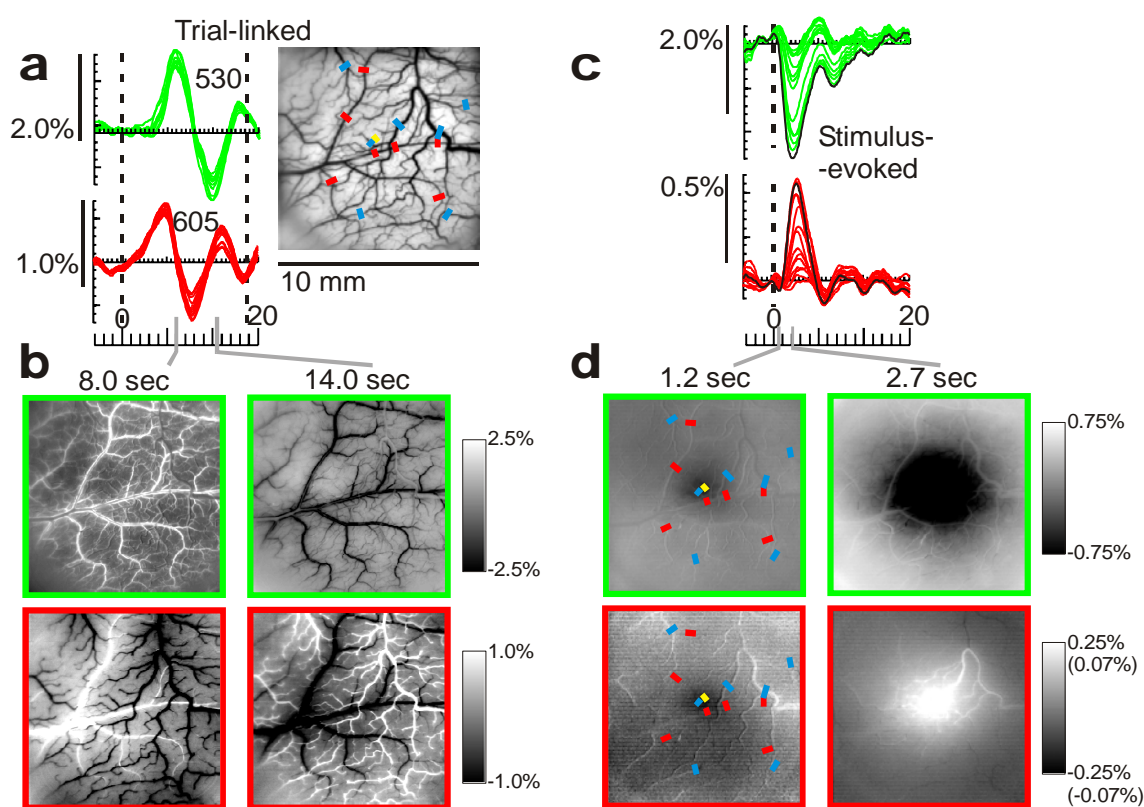


**Figure 2.14. Trial-related signals are global over V1, unlike stimulus-evoked signals.**

**a: Left:** Signals (parenchyma baseline) measured from multiple test lines distributed over V1 superimpose on each other in amplitude and time course. **Right:** Test line locations: blue: across

veins; red: across arteries. Imaged V1 area:  $\sim -0.5^\circ$  to  $-4.5^\circ$  azimuth,  $\sim -0.5^\circ$  to  $-3.5^\circ$  elevation. **b:** Image frames of trial-related signal at 2 time points. **c:** Stimulus-evoked ( $0.25^\circ$  line flashed on for 500 msec) signals measured at same test lines as in part a drop sharply in amplitude from peak at stimulus location (black line). **d:** Image frames of stimulus-evoked signal at 2 time points. Note test lines; yellow: at stimulus location. Greyscale: note 2 ranges for the two images at 605 nm: low range ( $\pm 0.07\%$ ) for 1.2 sec 'initial dip' image, & high ( $\pm 0.25\%$ ) for 2.7 sec.

We performed control experiments to verify that the observed signals were tied specifically to task-related trial onsets, independent of other timing signals and of retinal input. We confirmed that the signal periodicity was not linked to the animal either acquiring (Figure 2.23) or breaking (Figure 2.24) fixation – the two time points, during each trial, with any change in light on the retina (albeit minuscule). This also ruled out any links to extra-retinal fixation-related V1 activity [65]. We controlled for the rhythmic pupil dilations – for the possibility that cortical signals were being evoked by the accompanying pulse of extra light. Giving the animal simulated pupil dilations – a bright flash in the fixation point – evoked no cortical response (Figure 2.25). We confirmed that the cortical signals were independent of fixation cue brightness or colour (Figure 2.26); further, results with pinhole fixation cues were indistinguishable from those obtained earlier using cues  $\sim 25$ -fold larger in area ( $\sim 2.5$  mm, i.e.  $0.1^\circ$  diameter; data not shown). Finally, we confirmed that the observed signal periodicity was specifically entrained to trial onsets and not an accidental match with ongoing

activity (Figure 2.27), or present in trials where the animal was simply given juice at periodic intervals without being required to perform a fixation task (Figure 2.28). These controls were performed (and repeated) in 30 separate experiments (44 to 202 trials each) over a period of six months.

### **3.2.4. Predictive timing anticipates trial onsets; amplitude correlates with trial performance.**

The timing of the observed signals provided compelling evidence of an underlying predictive mechanism that anticipates trial onsets. Trials of fixed periodicity entrained physiological signals to the trial period, over all timing ranges tested (66 experiments, 2 monkeys: 6-sec to 30-sec trial periods; Figure 2.15, a, b; Also Figure 2.18, Figure 2.29). On switching trial timing unexpectedly after the monkey had established a rhythm of 10-20 correct trials at a given period, the measured signals – cortical signal and heart rate – continued to oscillate at the earlier period for a couple of trials before entraining to the new one (Figure 2.15, c, d). This occurred even though the animal himself picked up the new trial pace immediately, i.e. started holding and breaking fixation at the new rhythm right after the switch (i.e. clearly having noticed the new pace of fixation cues). Thus on switching from short to long trials the measured signals continued with sharp cusps at the short trial spacing even though the animal was fixating correctly at the longer period (Figure 2.15, c, d, Left). Similarly, on switching from long to short trials the cortical signal continued at its slower pace for one long period, overriding the first few short trials (Figure 2.15, c, d, Right).

This one-long-trial delay in switching was seen in all 9 experiments with switching trial periods. Tested 6-sec, 8-sec, 15-sec, 19 (~ 20)-sec, 30-sec periods; 5 experiments in monkey 'V', 4 experiments in monkey 'S').

The predictive nature of the trial-related signals was further evidenced by the way the signals stretched elastically to conform to different inter-trial intervals (Figure 2.15, a-d, caption). In particular, the HbT (530 nm) signal consistently started increasing (darkening) roughly midway in the intertrial interval – before the onset of the next trial – reaching a peak darkening close to, or following that trial onset (Figure 2.15, b). This elastic pattern of anticipatory HbT signal increase differs markedly from responses to visual stimuli of the same duration as the cued fixation, where the haemodynamic signal has an abrupt onset and fixed width following stimulus presentation independent of interstimulus interval (Figure 2.15, e). Further, the HbT signal timing was correlated specifically with trial onsets and not with reward – the peak position remained unaffected on delaying the reward associated with each trial (Figure 2.15, f).

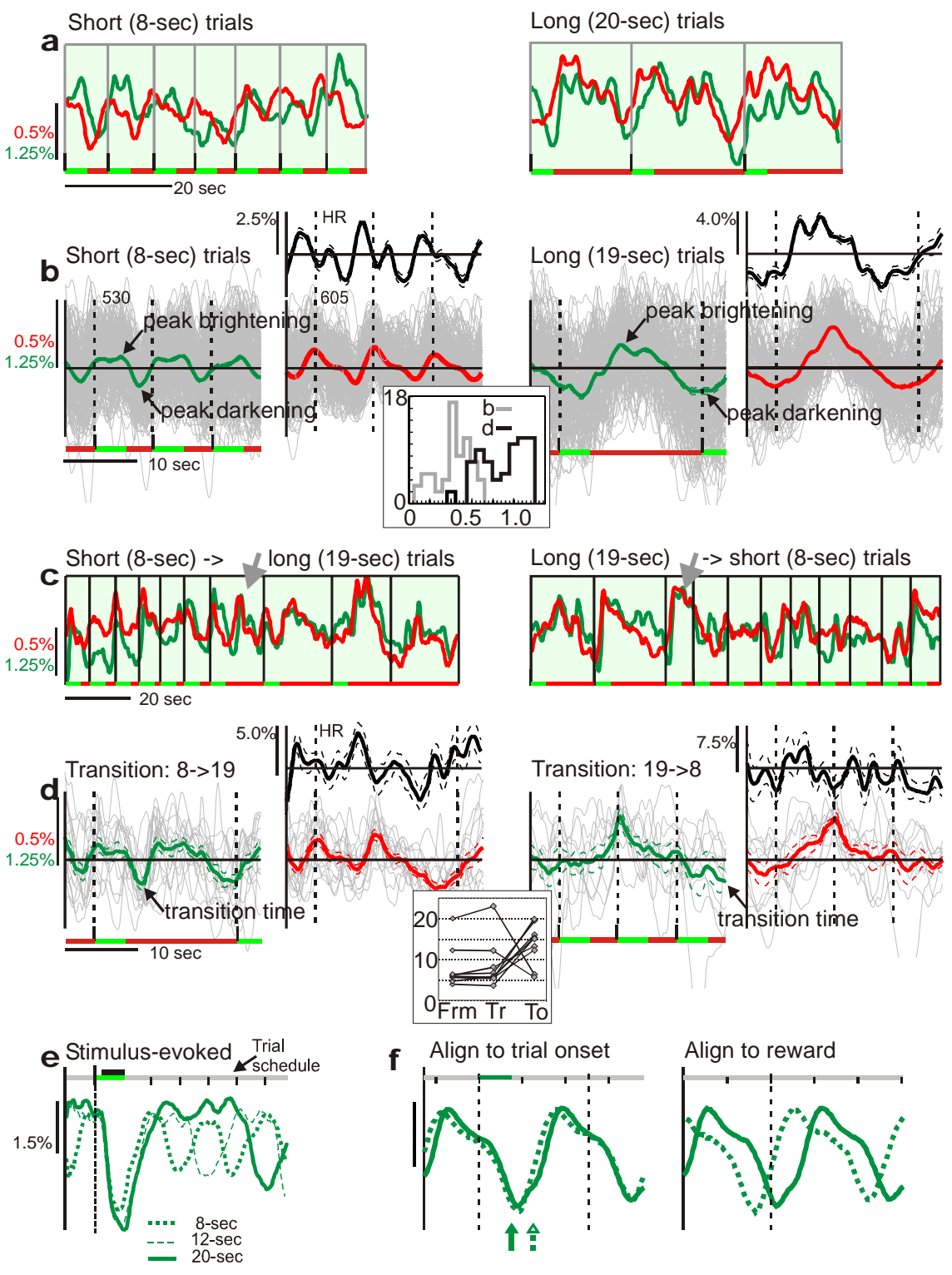


**Figure 2.15. Trial-related signal entrains to anticipated trial onsets.** Monkey was given alternating blocks of short (8-sec) and long (19-sec) trial periods: trials of fixed

duration (4 sec) but with different intertrial intervals. **a:** Within a block signal conforms to trial period: segments of continuously recorded cortical signals. **b:** Mean HR and cortical signals aligned to trial onsets. **Left:** short (n=220 trials). **Right:** long (n=172 trials). Note signal waveforms stretching elastically to fit trial period (dashed lines mark trial onsets). For 530 nm signals, peak brightening is roughly midway (3.8 sec, i.e. 0.47 in trial phase for short trials, 8.1 sec, i.e. 0.43 in trial phase for long trials), starting a slow darkening towards a peak darkening near the end of the period or into the start of the next trial (6.1 sec, i.e. 0.77 in trial phase for short trials, 19 sec., i.e. 1.0 in trial phase for long trials). **Inset:** population distribution of peak times in units of trial phase: peak brightening ('b', light gray: mean=0.43, std=0.16, N=66) and peak darkening ('d', black: mean=0.89, std=0.21, N=66). **c:** Transitions (gray arrows) between trial periods. **d:** Transition trials, aligned to trial onset. **Left:** short-to-long (n=16 transitions). Note the anticipatory short signal, including HR; 'transition time' = 6.7 sec after transition trial onset. **Right:** long-to-short (n=10 transitions); note switch after duration of one long trial giving a 'transition time' ~ 23 sec after transition trial onset. **Inset:** Population data showing transition times ('Tr') compared, in each case, to the peak darkening for trials of the pre-transition set ('From') and of the post-transition set ('To'). E.g. for the short-to-long transitions here 'From' = 6.3 sec, 'Tr' = 6.7 sec & 'To' = 19 sec. **e:** Cortical responses to visual stimuli of fixed duration but different periodicities (Stim: 100% contrast square wave gratings, 4 c/deg, stationary, 3 sec duration. Trial periodicity: 8, 12 and 20 sec). 530 nm signal for correct trials, aligned on trial onset. 'Trial schedule' shows trial timing: Green horizontal line: fixation (4 sec); black: stim on; vertical dashes: time markers showing subsequent trial onsets (all time periods). Note stereotyped stimulus-evoked response starting sharply from baseline independent of intertrial interval. **f:** Peak darkening is aligned with trial onsets rather than with reward timing. Reward was given either immediately after the end of the fixation period (**solid trace**) or 2 seconds later (**dashed trace**; timepoints 4 and 6 seconds within a 10 sec trial period). **Left:** Signals at 530 nm aligned to trial onsets for both conditions show identical phase independent of reward times (marked by

solid and empty triangles for immediate and delayed reward respectively). **Right:** The same signals aligned to reward time show phase mismatch.

The imaged arterial contraction-dilation cycle showed exactly the same anticipatory behaviour as the mean cortical signal, bringing fresh arterial blood to V1 with the same predictive timing and elastic waveform (Figure 2.16). Thus short trial periods entrained a short arterial contraction followed by a short dilation (Figure 2.16, a), while long trial periods entrained a correspondingly long contraction and dilation (Figure 2.16, c). In each case the arterial dilation tracked upcoming fixation cues, i.e. recharging cortex with fresh blood shortly preceding or leading slightly into the next trial onset. On switching unexpectedly from short to long trial periods the arterial rhythm showed one anticipatory short contraction-dilation before synchronizing to the long period (Figure 2.16, b). When switching from long to short trial periods the arterial cycle continued with one full long contraction followed by one long dilation overriding the initial set of short trials, before adjusting to the shorter periods (Figure 2.16, d). This predictive timing of the arterial cycle was seen in every experiment (n=66 experiments in 2 monkeys showing match of arterial cycle to trial period; n=9 experiments in 2 monkeys for the switch in trial periods.).

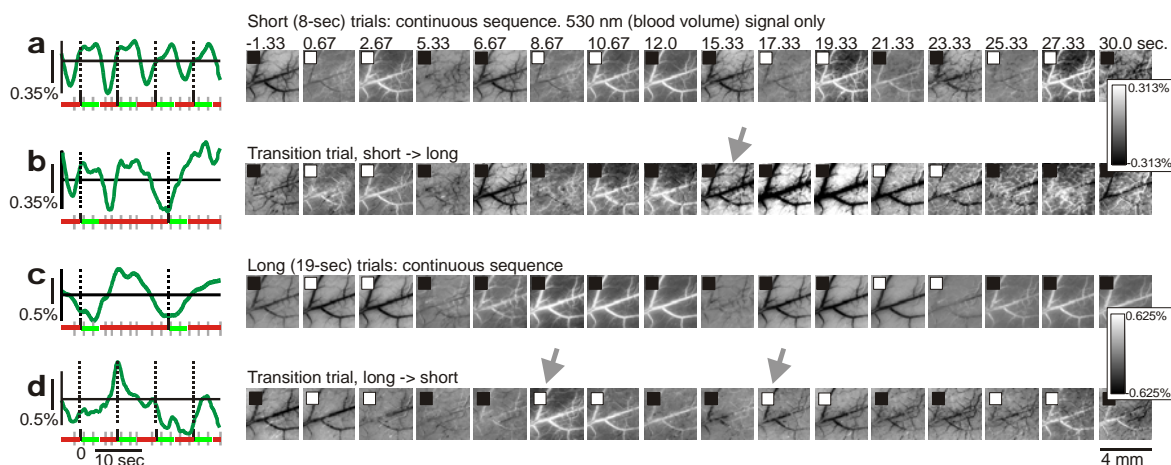


**Figure 2.16. Arterial cycle stretches to fit trial period, with maximum dilation shortly before anticipated onset of next trial.**

Same data set as in Figure 2.15. **a:** Mean signal (**left**) and image frames at selected time points (**right**; time points shown by gray vertical lines under mean signal). Note short arterial contraction-dilation cycles with dilations (darkening) shortly before upcoming trial onset (white inset square). Conventions as in Figure 2.13c,d. **b:** Same, for short-to-long transition trials. Note timing of arterial dilation during transition (gray arrow) anticipating short trial, matching 6a. Greyscale as in part a. **c:** Mean signal and individual images in a block of 19-sec trials. Note long contraction and dilation compared to a, with dilation leading trial onsets. **d:** Same, for long-to-short transition trials. Note long arterial contraction-dilation matching 6c despite animal performing short trial periods (gray arrows). Greyscale as in part c.

In a separate experiment with randomized trial periods (intervals between successive trials selected randomly from range 9 to 18 sec) the cortical response completed a full cycle at the shortest period (9 sec) followed by a relatively flat interval until the next trial onset (data not shown).

The trial-related V1 signal amplitude correlated with the animal's performance in the fixation task. Cortical signals – the mean signal and the arterial contraction-dilation cycle – were consistently strongest for trials that were part of a consecutive sequence of correct trials (Figure 2.30, a), weaker for correct trials preceded by incorrect ones (Figure 2.30, b), and weakest where the monkey broke fixation before trial end (Figure 2.30, c). The same rank ordering of response amplitude with fixation performance was seen in all experiments tested (n=35 experiments in 2 animals. Not all experiments could be tested, e.g. those with very few incorrect trials). This correlation between cortical signal strength and behaviour, independent of visual stimulation, was particularly noteworthy in the experimental session where monkey 'S' first learned the task, with a sudden emergence of trial-linked signals only when the animal started performing the task correctly (Figure 2.31; not included in the experiments tested quantitatively, due to its unique and unrepeatable nature).

### **3.2.5. General autonomic response vs. specific V1 arterial rhythm**

By testing the animal on an auditory control task we found that the observed trial-related signals had two components. The V1 arterial cycle was specific to visual tasks alone; but the simultaneous changes in heart rate, blood oxygenation and pupil dilation are likely part of a general autonomic response entraining to all periodic tasks. The auditory control task – pitch discrimination, at periodic intervals, in a dark room (Section 3.4) – also evoked a prominent periodic V1

signal at 605 nm comparable to the signal during visual tasks (Figure 2.17, a) accompanied by periodic changes in heart rate and a pupil response (two dilations per trial, once when the tone came on and again in anticipation of the tone changing pitch). The 530 nm (HbT) signal was weak, however, with no trace of any arterial contraction-dilation cycle – as can be appreciated in high-magnification image profiles (Figure 2.17, b). Even the venous signal (at 605 nm) was much weaker than the corresponding signal for visual tasks (see Figure 2.12, g, h). Simultaneous electrode recordings failed to reveal any neuronal activity either in MUA or LFP underlying the prominent BOLD-like 605 nm signal recorded during the auditory task (Figure 2.17, c). The auditory task-evoked 605 nm signal was thus likely to be a passive reflection of periodic changes in blood oxygenation due to the changing heart rate. All imaging sessions with the auditory task gave the same results (n=7 experiments in monkey 'S', periods ranging from 6 to 14 sec; unable to image monkey 'V' because of tissue overgrowth in his recording chamber after he learned the task).

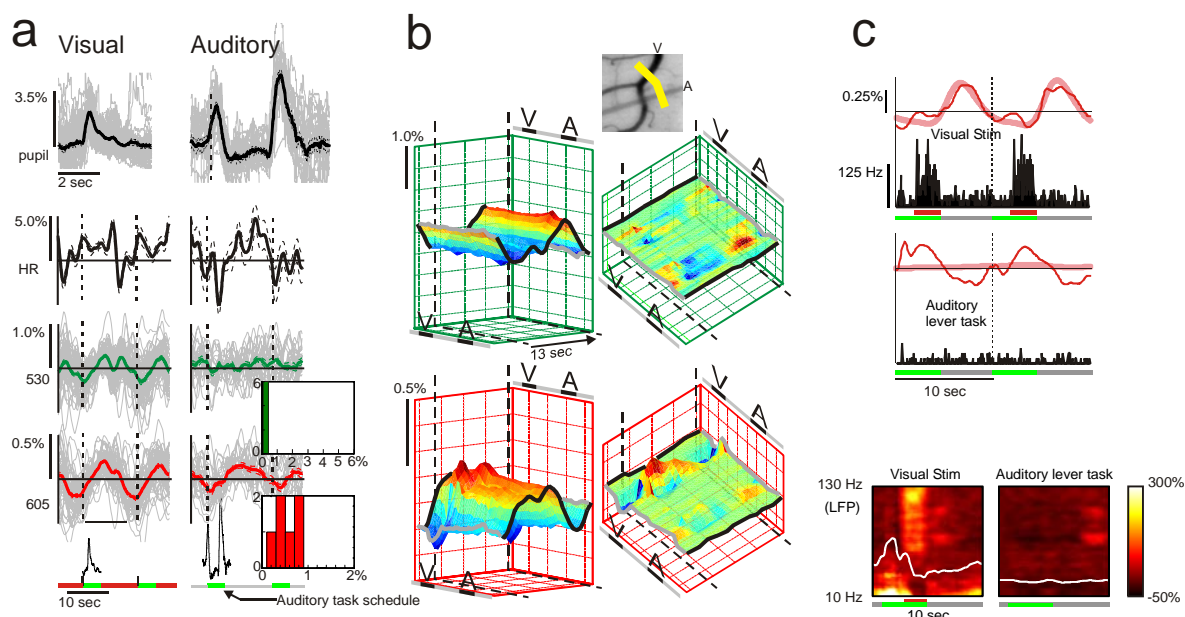


**Figure 2.17. Periodic auditory task also entrains haemodynamic signals in V1 but without any arterial contraction-dilation cycle.**

**a:** Physiological signals from alternating blocks of visual and auditory tasks. Visual: signals aligned with trial onset ( $n=55$  correct trials / 68 total). Auditory: signals aligned with tone onset ( $n=23$  correct trials / 48 total). Note pupil dilations, one at tone onset (dashed line) and again in anticipation of the change in pitch near the end of the fixed tone period. Auditory task schedule shows 'tone on' green) with aligned pupil response. Inset histograms: Mean signal amplitudes over population, shown on same scale as in Figure 2.11: 605 nm: mean=0.58%, std=0.20; N=6. 530 nm: (The 'arterial pumping' signal was less than noise. Here it is quantified by setting an upper limit, defined = std of 530 nm image at any time point): mean=0.10%, std=0.03; N=6 (2 of the total of 7 experiments were simultaneous electrophysiology + imaging, one exclusively at 605 nm, the other at 530 nm). **b:** Profile of image intensity along a test line at the same position as in Figure 2.13 (inset). Same conventions and scales as in Figure 2.13e-h (except for a shorter trial duration)  $n=85$  correct trials / 98 total. (A different day from the experiment shown in part a, with higher-magnification imaging). **c:** Simultaneous electrode recording and optical imaging, with alternate blocks of visual stimulation (grating, 100% contrast) or auditory lever task. Top: 'Visual Stim': Two cycles of recorded 630 nm signal (thin red line) and MUA (black) for visually stimulated

trials (N=33 trials). Thick pink: predictor of 630 nm signal, estimated by fitting the visually evoked MUA and haemodynamic signals, calculating the optimal kernel and then convolving the MUA with the kernel. 'Auditory lever task': same, for lever task (N=54 trials). Note the flat haemodynamic predictor, estimating by convolving the MUA with the same kernel. Bottom: Power spectral density of LFP for the same experiment, normalized to a common pre-trial baseline (auditory lever task). White trace: LFP power integrated over gamma band (10-130 Hz). Auditory task schedule showed as in part a, visual stimulation schedule as in Figure 2.12e.

### ***3.3. Discussion***

Using dual-wavelength optical imaging that we developed for alert behaving monkeys, we have discovered a novel anticipatory V1 mechanism that prepares cortex for periodic tasks by pumping in fresh arterial blood timed for task onsets. The resultant V1 haemodynamic signal – even in darkness – can be as strong as visually evoked responses ([7, 17] and Figure 2.11, Figure 2.12, Figure 2.14) and correlates with task performance. Four critical features of our imaging technique have made this finding possible. We recorded blood volume and oxygenation simultaneously (and not in separate epochs [18], which would miss the correlation with performance), in alert monkeys (critical for the behavioural insights), continuously (thus able to separate trial-related from stimulus-evoked signals) and with simultaneous electrode recordings.

Our findings challenge the generally accepted understanding of fMRI and related neuroimaging signals [55] (PET, optical imaging) by underscoring the

involvement of broader underlying neurophysiological mechanisms [5, 66]. With simultaneous electrode recording we consistently failed to observe local neuronal activity that could account for the anticipatory V1 signals – despite reliable prediction of stimulus-evoked signals at the same recording sites (Figure 2.12). Instead, the anticipatory signal appears to be driven by some mechanism distinct from the local neuronally-driven metabolic demand believed to mediate stimulus-evoked signals. This suggests that all neuroimaging signals could combine a distal predictive component with a local component that signals metabolic demand. Our findings also raise the possibility that even the ‘local’ component could signal not the actual energy consumption but a rapid local prediction of expected energy consumption based on initial changes in presynaptic and spiking neuronal activity [5, 66].

There are at least two separable components contributing to our observed anticipatory signal. The arterial pumping in anticipation of visual fixation (Figure 2.13) could reflect direct neuronal control of V1 blood flow [66, 67] specifically during visual tasks. The trial-triggered BOLD-like signals seen during auditory trials – with no arterial pumping (Figure 2.17) – likely reflect changes in blood oxygenation due to periodic changes in heart rate, where V1 is just part of the passive flow path of blood through the brain. Similar periodic oxygenation signals may be visible in all brain areas during any periodic task, along with specific arterial signals in brain areas relevant to the task modality.

### 3.3.1. Comparison with fMRI Studies of Anticipatory Signals

These findings offer potential explanations as well as caveats for earlier neuroimaging results. Several studies using fMRI have previously reported increases in BOLD signal unrelated to stimulus presentation [68-71], but correlated with the spatial location of the anticipated task. These studies demonstrated that cueing subjects to anticipate perceptual tasks at specific spatial locations triggers an anticipatory increase in BOLD activity throughout the parietal lobe. The increase in BOLD was larger at cortical locations representing the anticipated location of the perceptual task. The presence of these anticipatory BOLD signals in human V1 was very surprising because electrode recordings in macaques have reliably failed to find any anticipatory changes in firing in the V1 of macaques engaged in similar tasks [72].

Silver et. al. (2007) proposed two hypotheses explaining the observed disjunction between these BOLD effects and earlier electrophysiology. The neural hypothesis posited that anticipatory changes in BOLD reflected increases in spike rate or subthreshold activity in V1 at the cued locations<sup>5</sup> whereas the

---

<sup>5</sup> Though no anticipatory increases in monkey V1 has been documented, this does not rule out the presence of such an increase in human V1. Allocation of attention has been demonstrated to alter V1 responses to visual stimuli suggesting subthreshold influence even in the absence of changes in baseline firing rates (Motter 1993; McAdams & Maunsell 1999).

hemodynamic hypothesis proposed that the brain allocates increased blood flow to regions with anticipated increases in future metabolic demand.

By simultaneously measuring hemodynamic and neuronal changes in macaques, our findings provide significant new evidence that agree with the hemodynamic rather than the neural hypothesis. First, our observed anticipatory is generated endogenously and correlates with the animal's expectation of upcoming visual tasks rather than associated with any external cues (Figure 2.15). Second, we find no increases in any measure of neuronal activity associated with cueing and our observed signal cannot be explained based on any classic theories of neurovascular coupling (Figure 2.12). Third and last, our signal is associated with a large-scale contraction-dilation cycle of the arterial system that is specific to visual, but not auditory tasks. One prior study [68] found increases in V1 BOLD even in auditory tasks speculating that they may be due to functional connectivity between the auditory and visual cortices. While we also observe oxygenation changes associated with auditory tasks, these are not associated with any modulation of the arterial system (Figure 2.17) and suggest that the changes in V1 BOLD in auditory tasks may be due to a passive flow-through of oxygenated blood related to common vascular input rather than neuronal connectivity [73].

### **3.3.2. Comparison with Other Anticipatory Signals**

A number of features set our trial-related signal apart from other anticipatory signals reported earlier in V1 [74] or retina [75]. Thus in V1 anticipatory reward timing [74] visually-driven V1 neural activity is modulated in the period between cue onset and reward in a manner that predicts the reward. Haemodynamic responses evoked by such neural activity would have a stereotyped time course starting after cue onset and independent of inter trial intervals (Figure 2.15, e). Direct visual driving of V1 neurons plays a minor role in our observed signal. Further, it has a very different time course that starts much earlier in trial phase, peaks around the time of cue onset and adapts elastically to trial period (Figure 2.15, a, b). ‘Predictive firing’ seen in the retina [75] is very different again, a network response of the local retinal circuitry: retinal neurons, once set into oscillation using bright, full field periodic visual stimulation, continue ‘predictive’ oscillations after the stimulus is switched off. This is distinct from our observed response, which involves minimal retinal stimulation and is likely mediated by distal timing signals rather than local network oscillations in retina or V1.

### **3.3.3. Sources of Anticipatory Timing in V1**

The observed anticipatory entrainment to trial onsets is probably orchestrated by “master” timing signals from some central brain location [76]. Only a central mechanism is likely to be able to generalize over the broad range of trial triggers in our task (auditory or visual cues; cues of different sizes, colours, etc.) and to

drive the far-reaching physiological entrainment we observe, with both modality-specific (V1 arterial) and non-specific components (heart rate, pupil). This putative central mechanism would then be distinct from the sorts of mechanisms that have been proposed recently to explain timing in the brain, involving local task-specific circuits in different brain areas [77-79]. An important difference may lie in the timing intervals involved; it may be that while intervals of 10's of msec are determined in task-specific brain areas, a mechanism that measures in the seconds to 10's of seconds is more centralized, possibly involving the basal ganglia [80] or the prefrontal cortex [81].

#### **3.3.4. Possible Mechanisms Underlying Preparatory Hemodynamic Signals**

Our observation of vascular (arterial) signals in cortex in the absence of significant changes in the neuronal baseline activity suggests neuromodulatory control of the cortical vasculature, triggered by the putative central “master” timing signal. The observed heart rate modulation suggests, in addition, regulation of the sympathetic / parasympathetic balance via ACh / catecholamines respectively (both agents are vasoactive in cortex; cholinergic [82]; dopaminergic [28]).

While systemic levels of these agents are unlikely to affect brain responses directly because of the blood-brain barrier [83], they could be released in cortex via neuromodulatory nuclei such as the Locus Ceruleus (LC), the activation of

which is tightly linked with changes in psychophysical performance and behavioural responses [84]. While such a neuromodulatory mechanism will not directly drive neuronal spiking, it could multiplicatively facilitate responses to sensory inputs. The neuromodulatory response may then be a very interesting mechanism for simultaneously influencing both the local vasculature and neuronal responsiveness, something we are pursuing currently.

### **3.3.5. Functional Implications of Anticipatory Hemodynamics in Cortex**

Functionally, the observed vascular signal could pertain to the anticipatory attention signals seen in humans [69-71, 85] or could be a distinct mechanism of broader anticipatory trial-linked arousal that prepares the brain for action ahead of predictable events. The observed arterial preparation correlates with task performance (Figure 2.30), is specific to visual and not auditory tasks (Figure 2.17) and its timing correlates with trial onset and not reward (Figure 2.15, f; Figure 2.28) or other behavioural events (Figure 2.23; Figure 2.24; Figure 2.27). The interaction of our observed signal with specific visual tasks needs to be investigated. This means first, asking whether visual tasks that are spatially localized evoke correspondingly localized anticipatory signals in cortex; and second, relating the anticipatory signal strength with subsequent stimulus-evoked signal amplitude and behavioural performance [70].

Finally, our findings offer a plausible functional significance for the ongoing  $\sim 0.1$  Hz to  $\sim 0.05$  Hz (10 – 20-sec period) ‘vasomotor’ oscillations seen in functional brain imaging, whether with optical imaging [34, 52, 86-88] or fMRI [89]. This oscillatory signal is driven by underlying rhythmic vasodilation of cerebral blood vessels [90, 91] and is as strong as stimulus-evoked responses. In brain imaging, particularly with anesthetized subjects, this oscillatory signal is mostly treated as an ongoing vascular ‘artefact’ to be averaged away [34]. It is possible that this spontaneous ‘vasomotion’ reflects intrinsic nonlinear oscillatory mechanisms in the cortical vascular network that also underlie our anticipatory arterial signal. In their normal function these intrinsic oscillators could be recruited into global trial-linked oscillations over V1 (as here) or local stimulus-evoked changes [91]. This possibility further underscores the importance of studying the control of cortical blood flow for interpreting functional images.

### ***3.4. Methods:***

#### **3.4.1. Summary:**

Results were obtained using continuous, dual-wavelength intrinsic-signal optical imaging and electrode recording in two monkeys engaged in either visual fixation tasks or auditory control tasks. Standard alert-monkey optical imaging techniques [17] were used to record the intrinsic cortical signal, continuously [52], through a clear silicone artificial dura [51] and glass-fronted recording chamber implanted over the animals’ V1. The primary innovation here consisted

of our using two imaging wavelengths. Two arrays of fast, high-intensity LEDs at the two wavelengths (530 nm, 605 nm) were switched on and off alternately in synchrony with the camera, thus illuminating the brain surface alternately with each wavelength on successive camera frames (15 frames / sec). The illumination alternated much faster than typical haemodynamic signal time scales giving, in effect, simultaneous optical imaging at both wavelengths at 7.5 frames / sec (but see [92]).

All experimental procedures were performed in accordance with the NIH Guide for the Care and Use of Laboratory Animals and were approved by the Institutional Animal Care and Use Committees (IACUC) of Columbia University and the New York State Psychiatric Institute.

### **3.4.2. Tasks: Visual fixation:**

Two monkeys were trained on a variety of visual tasks on a common periodic fixation schedule cued by fixation point colour: red (or fixation point off): intertrial intervals where the animal was free to break fixation; green: 'trial on' where the animal was required to maintain fixation within a  $0.5^\circ$  radius window to get a juice reward. Timing: 'trial on': typically 4 sec. 'Intertrial intervals' typically fixed for any given experiment: 2 to 26 sec giving overall trial periods of 6 to 30 sec. For 'timing switch' experiments (Figure 2.15, c, d) the intertrial interval was switched deliberately amongst a set of 2 or 3 values. For some experiments (as noted in fig legends) an intentional timing jitter (with

homogeneous distribution of intertrial intervals around the mean) was used to test for intrinsic signal periodicity. Eye fixation and pupil diameter were recorded using an IR eye tracking system [50]. The 'dark-room' task (Figure 2.11, c) used in the experiments reported here comprised fewer than 10% of the behavioural tasks that the animals performed, with the other 90% involving visual stimuli on the same fixation schedule.

### **3.4.3. Tasks: Auditory control:**

For the auditory control (Figure 2.17), animals were trained on an auditory pitch discrimination task, in a completely dark room lacking even the fixation point. Each trial started with the animal pulling a lever. After a fixed delay (range 4 - 10 sec), a tone came on, which then changed pitch after yet another delay (4 sec, matching fixation period for visual tasks). The monkey's task was to then release the lever as rapidly as possible for a juice reward. Once the animals learned this task they performed trials in rapid succession, with a periodicity that the experimenter determined by setting the initial delay from lever pull to tone on. The monkey also typically continued looking in the general direction of the fixation point (even though none was present), allowing us to track pupil dilation with the IR camera.

### **3.4.4. Optical imaging: Surgery, recording chambers, artificial dura:**

After the monkeys were trained on visual fixation tasks, craniotomies were performed over the animals' V1 and glass-windowed stainless steel recording

chambers were implanted, under surgical anaesthesia, using standard sterile procedures [17, 93]. The exposed dura was resected and replaced with a soft, clear silicone artificial dura. After the animals had recovered from the surgery, cortical activity from their V1 was optically imaged, routinely, while the animals engaged in relevant behavioural tasks. Recording chambers and artificial dura were fabricated in our lab using published methods [51].

#### **3.4.5. Optical imaging: Hardware, electronics and imaging routines:**

All images were acquired on a Dalsa 1M30P camera (1024 x 1024 pixels, 30 frames / sec, but typically binned to 256 x 256 pixels, 15 frames / sec), through an Optical PCI Bus Digital Frame Grabber (Coreco Imaging, Boston, MA). Imaging software was developed in our lab based on a system by V. Kalatsky [52]. Illumination was provided by two arrays of high-intensity LEDs (Agilent Technologies, Purdy Technologies; Appendix I) with two different emission wavelengths: one centred at 530 nm (close to an isosbestic point for Hæmoglobin, i.e. absorbed equally in oxygenated and deoxygenated hæmoglobin) & the other at 605 nm (absorbed primarily in deoxygenated hæmoglobin) [38]. The two arrays were switched on and off alternately in synchrony with the camera, giving an effective frame rate of 7.5 frames / sec at each wavelength. The light from the LEDs was filtered through small individual interference filters (Omega Optical) mounted on each LED. A 'macroscope' of back-to-back camera lenses [53] (Nikon, assorted fixed focal lengths), focused on the cortical surface, was used

for imaging. Image acquisition was run continuously, simultaneously recording the signal from the camera, timing signals relevant to the stimuli and trials (trial onset, stimulus onset, identity and duration etc.) and behavioural data from the animal (eye position, pupil size, timing of fixation breaks, fixation acquisitions, trial outcomes). The continuous data were then reconstructed off line into sequences of successive trials, separately for each wavelength, using custom software (written using MATLAB).

#### **3.4.6. Optical imaging: Image processing:**

All images were first 'shift-corrected' to correct for any residual movement of the cortical surface that remained despite the specially designed camera mount, animal head post and overall structural framework (NOTE: most of the residual movements were due to the brain moving relative to the animal's head, when the animal shifted body position etc). This 'shift-correction' consisted of aligning each image frame to the first frame of a given experimental session, using the imaged blood vessels as references. Each image frame was cross-correlated with the reference frame, and a gradient descent method used to maximize this correlation value as a function of lateral shifts in the image position, frame by frame. These 'shift-corrected' images were then used for all subsequent processing.

For the time-varying trace of the mean signal strength (shown in the continuous traces, Figure 2.11, c) the signal for each image frame was averaged over the full

image area, and divided by the overall mean for the entire experiment – thus expressing the signal in units of % change in light reflected off the cortical surface relative to the overall mean.

To visualize the activity imaged off the cortical surface (Figure 2.13), image sequences (e.g. of 256 consecutive image frames aligned on each trial onset), were averaged, frame by frame, across a set of trials selected according to some criterion (for most tasks, the criterion was simply that the animal held fixation correctly through the trial). This gave ‘movies’ of cortical activity at the camera frame rate (7.5 frames / sec at each wavelength). Each frame in the movie was then divided, pixel by pixel, by the **trial mean** i.e. the average of the movie over one trial duration. The division was necessary to compensate both for the inhomogeneous illumination over the cortical surface, and for the different reflected intensities of light off different parts of the cortical surface (i.e. veins, arteries, parenchyma). The resulting divided image shows the fractional change in light intensity off the cortical surface, relative to the trial mean, for each frame of the trial (Figure 2.13, d). To get the image profiles (Figure 2.13, e, g), image values were read off this divided image along the vector of points defining the test line, for each time point in the trial. Points along the test line that were far from identifiable blood vessels were defined as ‘parenchyma’ and a linear regression line fitted through the corresponding image values at each time point, giving the ‘**parenchyma baseline**’ signal as a function of time, for each

wavelength. This parenchyma baseline signal was then subtracted from the full image profile to give the blood vessel signals relative to the parenchyma (Figure 2.13, f, h).

For visualizing stimulus-evoked activity (Figure 2.11, b; Figure 2.14, c, d; Figure 2.15, e) similar movies of cortical activity were obtained, aligned to stimulus onset, both for trials with stimuli present and for interspersed 'blank-screen' trials with a blank stimulus. Each movie frame was divided by a 'pre-stim' baseline of 3-5 frames immediately preceding stimulus onset to give the overall change in cortical activity post stimulus (e.g. Figure 2.11, b). Blank-screen movies were subtracted from the stimulus-evoked movies to remove the contribution of the trial-related signal to the overall cortical activity, leaving the stimulus-evoked component of the cortical signal (Figure 2.14, c, d). The resulting images were then averaged over the image area, frame by frame, to give the time course of the mean stimulus-evoked image (e.g. Figure 2.15, e). Note, in Figure 2.15e, that response peaks following the first one are generally weaker. This is because whereas the first peak came from a trial where the animal correctly maintained fixation, sequences of frames aligned on a correct trial onset included trials where the animal broke fixation.

For calculating signal power spectrum (Figure 2.29), all trials of a given period were first pooled together by cutting and pasting the relevant blocks of trials into a continuous sequence. The power spectrum was then calculated on this pooled

set, using a moving time window (200-sec window, 20-sec steps) in order to identify any changes in the power spectrum over the duration of the experiment. Mean power spectrum was then calculated by averaging over the entire duration.

#### **3.4.7. Electrophysiology: Hardware, electronics and analysis:**

All spiking and LFP data were acquired using a Plexon data acquisition system (Plexon Inc.) with either plastic coated tungsten electrodes (FHC Inc.) or, for Monkey V, homemade glass coated tungsten electrodes with impedances ranging from 300 K $\Omega$  to 800 K $\Omega$ . Penetrations were made through a small hole drilled in the glass cover of the imaging chamber allowing for simultaneous acquisition of electrophysiological and imaging data. Recordings were made sampling depths ranging from most superficial to ~1500 microns below the pial surface ('blindly' by advancing the electrode in 200 – 400 micron steps after first encountering multiunit 'hash') over multiple V1 location at an average visual eccentricity of ~2 degrees. Recording was run continuously and was aligned to the imaging data using custom software (written using MATLAB).

We contrasted the visually driven responses with dark-room responses quantitatively by comparing, in each case, the measured haemodynamic signal with a signal predicted using the corresponding MUA response. For each recording site we first fit the stimulus-driven haemodynamic response to the MUA, trial by trial, by calculating the optimal haemodynamic kernel for the pair

using a simplex-based algorithm (see later Section 3.4.9: Fitting to Haemodynamics). We then convolved the kernel with the stimulus-evoked MUA and the dark-room MUA to calculate, in each case, a “predicted” haemodynamic signal. For visually driven trials the predicted haemodynamic signal fit the measured signal very closely, trial by trial, with high values of  $R^2$ .

### 3.4.8. Electrophysiology: Data processing:

All spiking data was binned into 16 msec bins (the frame period for the imaging camera) and aligned to the haemodynamic traces using simultaneously recorded synch events. LFP data was spectrally decomposed using `mtspecgram` (Chronux Toolbox for MATLAB; sliding window of 1 sec, a step size of 250 msec, frequency range from 10 to 130 Hz) and interpolated into a continuous power spectrum aligned to the haemodynamic traces. Frequencies from 56 to 64 Hz were excluded from analysis to avoid any artefacts due to line noise.

### 3.4.9. Electrophysiology: Fitting to Haemodynamics:

For each recording site, we obtained simultaneous spiking and haemodynamic responses to trials on which a visual stimulus was presented as well as trials done in complete darkness. Correct trials were extracted from the continuous time series and concatenated into a synthetic series with only correct trials. We modelled the haemodynamic response function (HRF) with a gamma kernel of

the form:  $HRF(t, T, W, A) = A * \left(\frac{t}{T}\right)^\alpha * \exp\left(\frac{t-T}{-\beta}\right)$ ; where  $\alpha = (T/W)^2 * 8.0 * \log(2.0)$ ,

$\beta = W^2 / T / 8.0 / \log(2.0)$ , and  $K$  is the amplitude,  $T$  is the time to peak, and  $W$  is the full width and half maximum. We fit the kernel parameters using a downhill simplex algorithm (`fminsearch`, MATLAB) by comparing the actual haemodynamic response obtained during stimulated trials to that predicted from a convolution of the HRF with the corresponding spike trace. The algorithm reliably converged to similar temporal HRF parameters across all days ( $T=2.50$  (0.08) sec,  $W = 1.68$  (0.06) sec). The proportion of the variance in the haemodynamic responses explained by neuronal activity was quantified using the  $R^2$  statistic from linear regression of the predicted haemodynamic trace to the observed trace for both the stimulated and the dark room trials (Figure 2.12).

### 3.4.10. Additional Figures:

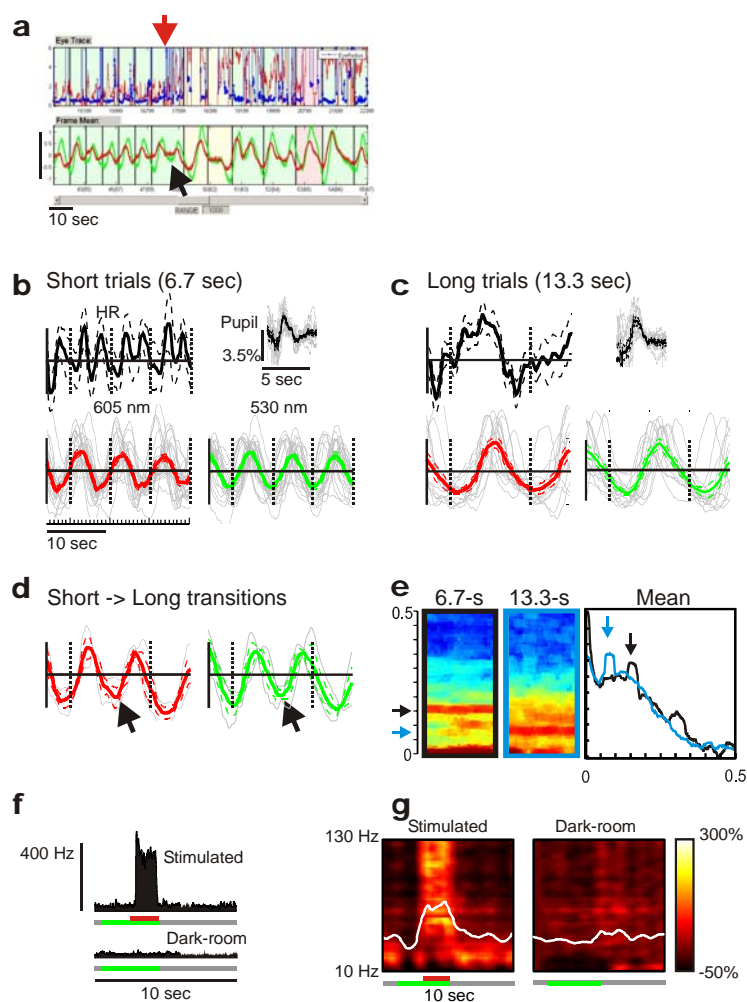


**Figure 2.18. Representative set of trial data from monkey 'V' showing broad similarity to the data from monkey 'S'.**

**a:** Continuous trace of eye data and haemodynamic signals including a short-to-long transition.

**Top:** eye position (blue) and pupil (red). Note how well monkey V has learned the task, holding fixation during the cued fixation periods and breaking only at trial end. **Bottom:** 605 nm (red) and 530 nm (green) signals. Black arrow: anticipatory short period at the transition. (Here the animal faltered after the transition and took a couple of trials to attain the right pace at the new period). **b, c:** trial-triggered traces of short and long periods for the same experiment as in a. **d:** Trial-triggered traces of short-to-long transitions (black arrow: anticipatory short response in transition). **e:** Power spectra of haemodynamic signals showing spectral peaks for the short period

(0.15 Hz: black) and long period (0.075 Hz: blue). All conventions as in Figure 2.15. **f**: MUA recorded during visually stimulated trials (**top**: 100% contrast grating, 4 cycles / deg, 2 deg diameter, drifting) or dark-room fixation trials (**bottom**) in alternating blocks, from one recording site. Similar recordings were made at 5 recording sites sampling different depths down to about 1500 microns. **g**: Power spectral density of LFP from same recording as in part f.

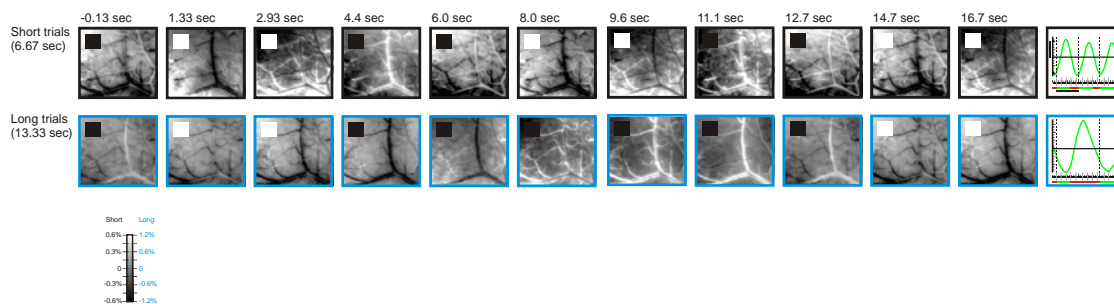


**Figure 2.19. Representative set of images from monkey 'V' showing anticipatory arterial contraction-dilation cycle as in monkey 'S':**

Single frames at indicated time points, from the "short" and "long" trial period sets shown in

Figure 2.18. Same conventions as in Figure 2.16. Note the fast arterial contraction-dilation for the

short trials, extended arterial cycle for the long trials. Scale bar in mean trace: 0.6% for short trials,

1.2% for long trials.

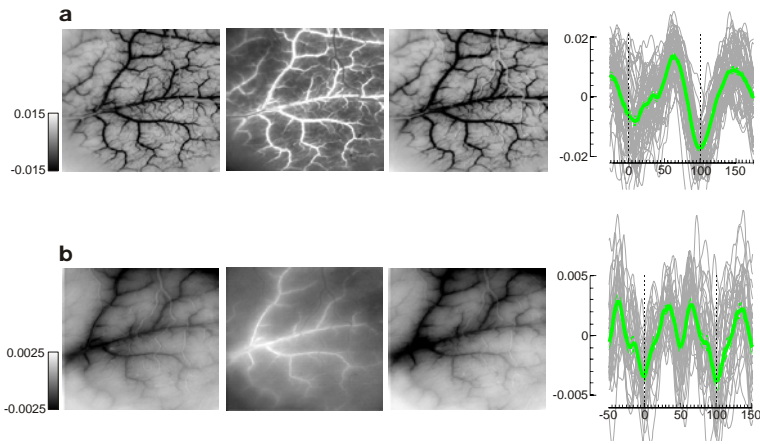


**Figure 2.20.** The day-to-day variation (particularly, low recorded amplitudes) of the 530 nm signal is likely an artifact of day-to-day variability in degree of scatter in the recording chamber medium (agar + artificial CSF).

**a:** (Left) Images from 3 trial time points (0, 60 and 100 frames, i.e. 0, 8 sec and 13.3 sec at 7.5

frames / sec) and (Right) trial-triggered mean signals, on a day with fresh medium in the

recording chamber. **b:** Images at the same time points, and corresponding mean signal on a

recording session with 3-day-old medium (same data as in 'visual' task, Figure 2.17, a). To avoid

disturbing the cortical surface, and to reduce the chance of infections, we replaced the medium

only once or twice a week. The agar turns turbid over days, reflecting more scattered light thus

reducing signal / noise, and acting as a low pass filter reducing the sharp features of the arterial

contraction / dilation pattern. Note the  $\sim 5$ -fold reduction in signal strength between 'a' and 'b'.

The arterial vasomotion pattern is unmistakably present even with the poorer image in b.

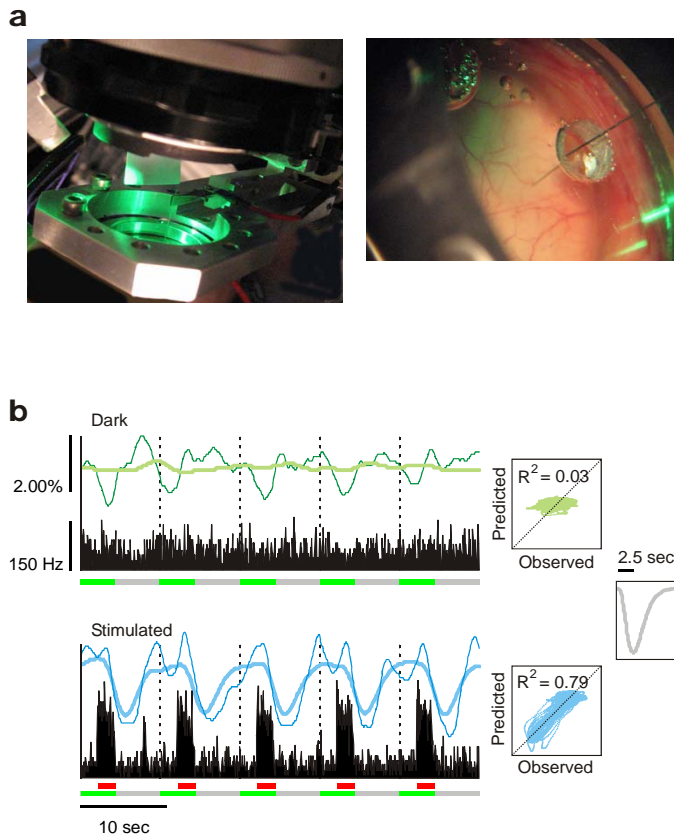


**Figure 2.21. Supplementary figures on electrode recording.**

**a: Left:** Setup for simultaneous electrophysiology and optical imaging. (Assembly is surrounded by light-proof baffles when in use). **Right:** Electrode positioned through window and artificial dura, under visual guidance using dissection microscope. (NOTE: it is now more than a year since we first implanted this chamber in monkey 'S'). **b:** Comparing measured and predicted hemodynamic signals, using kernel obtained by fitting the dark-room MUA to hemodynamics. Same recorded data as in Figure 2.12, a, b. The optimal kernel from this fit was very similar to that obtained by fitting the visually evoked MUA to hemodynamics (Figure 2.12), presumably because the fit picks out the only consistent relation between spiking and hemodynamics – even though the spike-evoked signal is a small fraction of the measured dark-room hemodynamic response. The dark-room fit gives a better prediction of the visually evoked hemodynamic signal than of the dark-room signal.

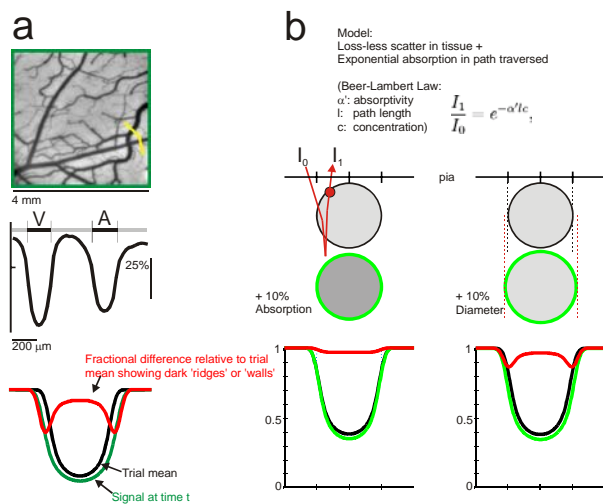


**Figure 2.22. Brightening/ darkening artery walls imply arterial contraction/ dilation.**

**a: Top, middle:** Image profile through blood vessels in trial mean image, 530 nm (same as Figure 2.12, a). **Bottom:** Schematic showing that dark “walls” of artery in the signal at a given time t (fractional change at time t relative to trial mean) implies that the image profile at t is wider than the trial mean. **b:** A model of the signal underlying intrinsic images<sup>18</sup>, generating thick “walls” in image with blood vessel dilation. Light entering the tissue scatters and reflects off multiple loss-less scattering sites (cell membranes, subcellular particles etc), without absorption, to re-emerge after having traveled some net distance through tissue. The effect of absorbers (HbR, HbO) can then be modeled as determining the probability of absorption, exponential with net distance traveled in tissue (Beer-Lambert law). This controls the fraction of the light that does re-emerge at any point on the cortical surface. A simplified simulation of such a model with a circular ‘blood vessel’ in the path of the light gives absorption profiles similar to those measured in our images. The effect of increasing the concentration of the absorbing material in the blood vessel (e.g. increasing the ratio of HbR to HbO while keeping HbT fixed) increases the depth (amplitude) of absorption without altering its width (green profile, ‘+ 10% **absorption**’) giving a net darkening of the blood vessel image (red profile, left). Increasing the blood vessel diameter, on the other hand (‘+10% **diameter**’), increases both the amplitude and the width of the absorption profile. Thus the difference image now has sharp ‘edges’ of increased darkening by the walls of the blood vessel along with a net darkening (profile in red, right). Contraction of the blood vessel will give

a net lightening with bright bounding walls.

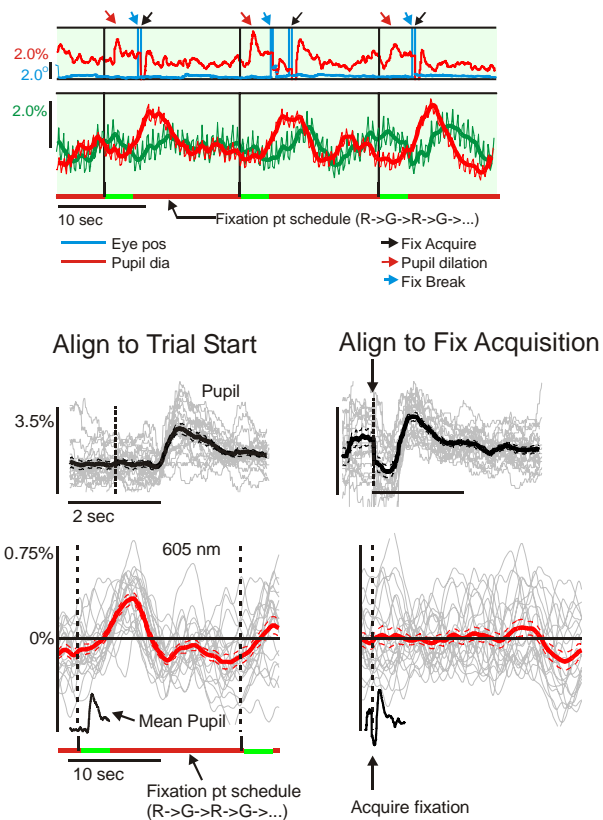


**Figure 2.23. Cortical signal does not synchronize with acquiring fixation at the start of the trial:**

**Top:** Continuous recording. **Bottom, Left:** Trial-by-trial average of pupil response and 605 nm cortical signal for correct trials (sequence of  $n=21$  correct trials), aligned to trial onsets (dashed vertical line on the left). **Right:** The same traces but now aligned to the fix acquisition for each trial (black arrows in the continuous trace, top). The pupil dilates sharply on fixation but there is no cortical signal. Figure conventions as in Figure 2.11.

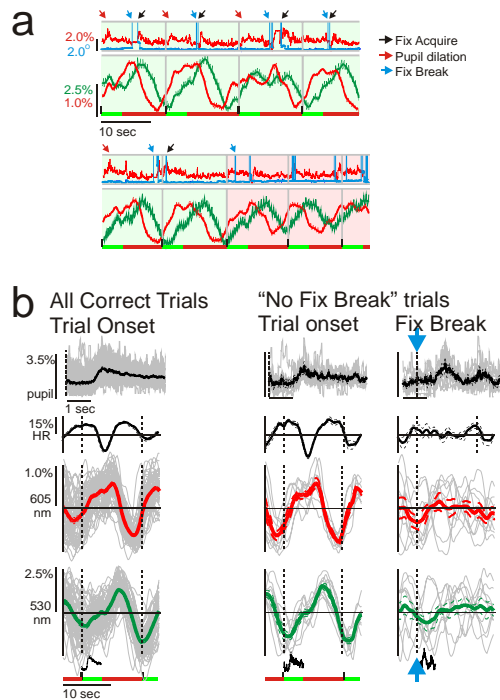


**Figure 2.24. Cortical signal does not synchronize with breaking fixation at trial end.**

It was necessary to find fixation break time points independent of trial onsets to use as our control. On most trials the animal broke fix right at trial end, at a fixed time after trial onset. But on ~ 15% of the trials he broke fix at a different time; we checked for signal timing on this subset of trials. **a: Top:** Typical sequence of trials showing pupil dilation (red arrow), fixation break at the end of each trial (blue arrow) followed by a quick fix acquisition (black arrow) as in Figure 2.11, c, d. **bottom.** Two of the minority of 9 trials (out of 56 correct trials, 127 total trials) where the animal broke fixation at a later intertrial time point. Note that even when he lost his rhythm and broke fixation during the cued fixation period, thus making an error and not getting any juice reward (pink trials), his cortical signal continued to oscillate at the trial period albeit with progressively smaller amplitude. **b: 'All Correct Trials':** All physiological responses for correct trials (n=56), aligned to trial onset. **"No Fix Break" trials':** Responses during the subset of correct trials where he held fixation at least 5.3 sec after trial end (n=9). These trials gave signals very similar to the rest of the set of correct trials when aligned on trial onset (**left**). Aligning on fixation break (blue arrow, **right**) gave no significant pattern.

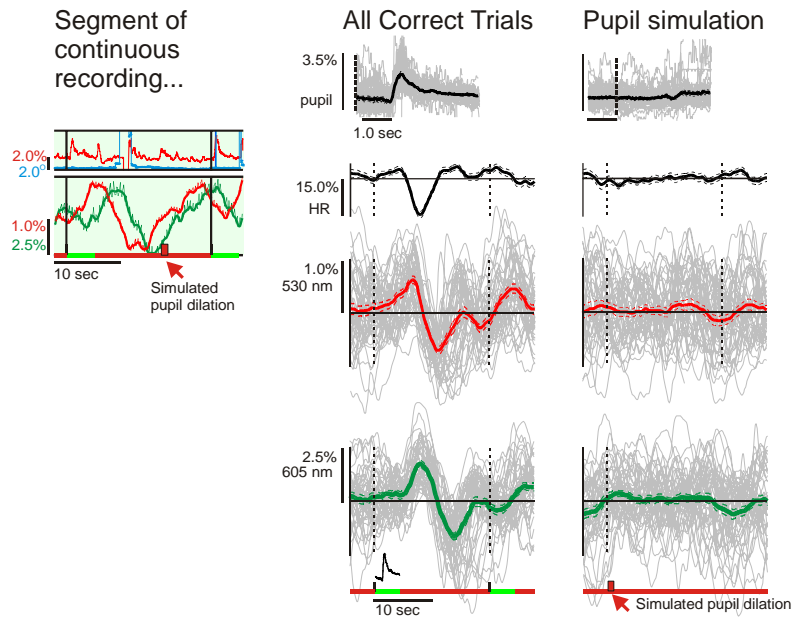


**Figure 2.25. Signal periodicity is not triggered by the flash of increased light input on pupil dilation.**

The largest pupil dilation we measured was 5% of the diameter, duration  $\sim 1$  sec, which would increase the pupil area – and light entering the eye – by 10%. This was simulated with flashes of increased fixation point brightness (30% increase, lasting 1 sec), at random times during the inter trial intervals but while the animal held good fixation – as in the **segment of continuous recording** – so that he was guaranteed to see the flash. **‘All Correct Trials’**: Same data as in Figure 2.11, c-f; **‘Pupil simulation’** Same signals but aligned to simulated pupil flash for those trials where the animal had good eye fixation starting at least 2 sec before the flash ( $n=47$ ). The same ‘simulated pupil flash’ control was repeated in a separate experiment, with identical null results ( $n=39$  simulated pupil flashes during good fixation)

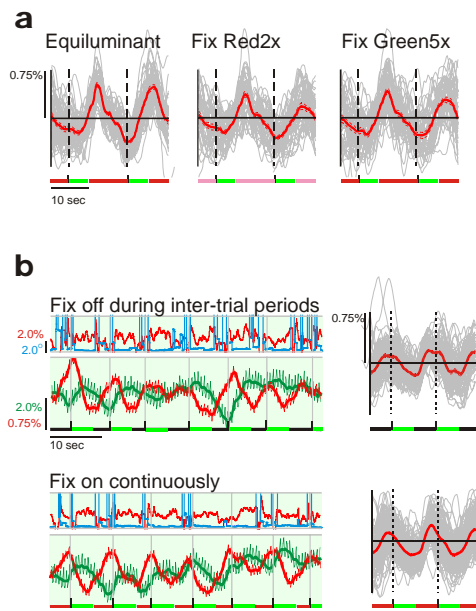


**Figure 2.26. Cortical signals are independent of the brightness of the trial onset cue:**

**a:** Bracketing around equiluminance. We controlled for the possibility that the signals were triggered by the red  $\rightarrow$  green cue not being equiluminant for the monkey. In successive blocks, the red and green colours chosen for the fixation point were made equiluminant (see Methods for details;  $n=46$  trials), or adjusted so that the red had 2x the equiluminant intensity while holding green constant ( $n=45$  trials), or so that the green had 5x the equiluminant intensity while holding the red constant ( $n=46$  trials). Cortical signal (605 nm shown here), aligned to trial onset, showed no effect of these manipulations around equiluminance. **b.** Changing the onset cue from R $\rightarrow$ G to OFF $\rightarrow$ G makes no difference to the cortical signal. In successive blocks we had two different fixation point schedules. In one schedule, the fixation point was off during intertrial intervals and on only through the trial duration (**'Fix off during inter-trial intervals'**;  $n=84$  correct trials out of 93 total); in the other, the point was on continuously and just changed colour, equiluminant red to green to cue trial onset (**'Fix on continuously'**;  $n = 135$  correct trials out of 153). Cortical signals showed no effect of this manipulation of the fixation point, whether in the raw continuous trace (left) or in the average aligned to trial onset (right). This control was performed  $\sim 1$  month after the animal had learned the task with the fixation point being on continuously.

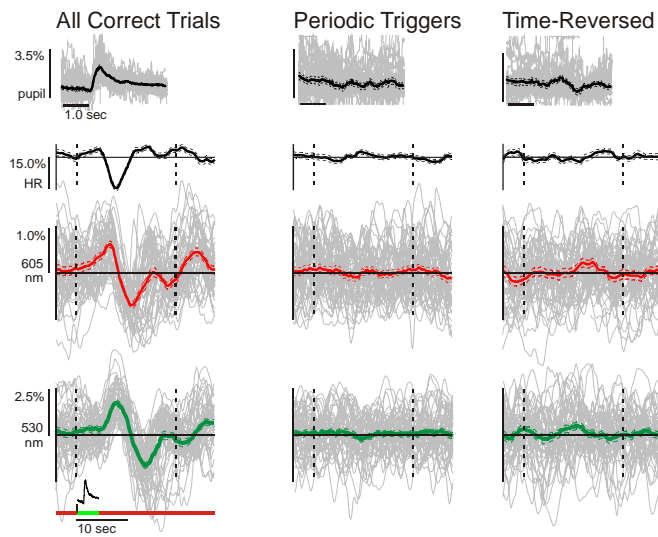


**Figure 2.27. Periodicity of trial-triggered signal is not due to the accidental entrainment of a trial-independent intrinsic periodicity.**

Same data as in Figure 2.11, c-f. In order to control for the possibility that our periodic trials were coinciding accidentally with an intrinsically periodic cortical signal, we ran a long block of trials with a small systematic jitter in trial period. Successive trial periods were selected randomly from the homogeneous distribution of values (20 sec  $\pm$  4 sec). The same data set was used in Figure 2.11, Figure 2.18. **'All Correct Trials'**: Same as Figure 2.11, e, f. **'Periodic Triggers'**: An artificial set of exactly periodic triggers was created, with spacing equal to the average trial onset period (20 sec). The measured physiological signals, when aligned to these exactly periodic triggers, showed no periodicity. **'Time-Reversed'**: All physiological signals were time-reversed (i.e. the start of each continuous trace over the 102-trial block flipped to the end and vice versa), then aligned to the actual, experimentally used trigger times for correct trials. No pattern emerges in the triggered mean. These control calculations were repeated, with similar results, for another experiment (127 trials, trial period 12 sec  $\pm$  2 sec)

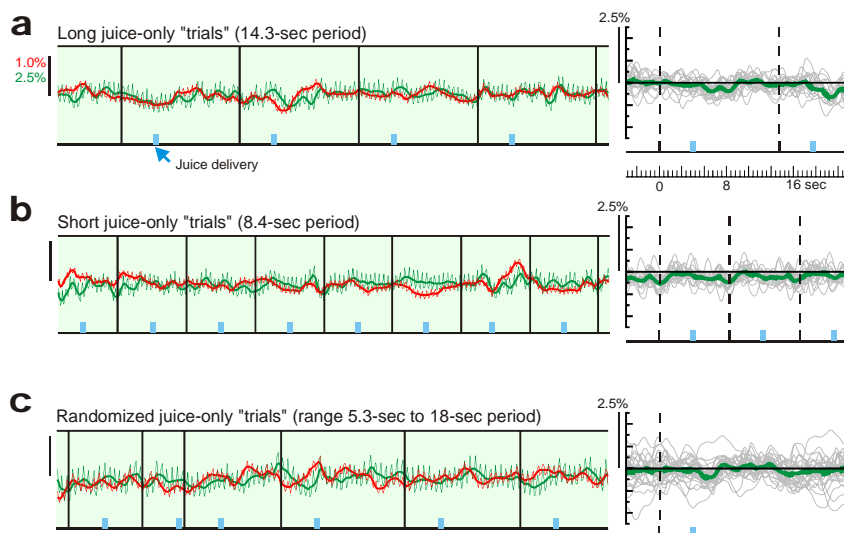


**Figure 2.28. Trial-related V1 signal is not triggered by simply giving regular juice outside the context of the fixation task.**

a. Continuous traces (left) and triggered averages (right) from “trials” where the animal was given free juice (blue ticks as shown) at regular intervals (14.3 sec) in a dark room (monitor turned off, no fixation point). To compare with regular trials, traces are shown with “trial onset” markers placed 4 sec before each juice delivery, to reproduce the usual 4-sec trial duration. Triggered averages were aligned to these “trial onsets” (N=27 trials). b: Same, for a shorter inter-“trial” interval of 8.4 sec. N=33 trials. c: Same, for randomized juice delivery times, ranging from intervals of 5.3 to 18 sec (N=44 trials). All amplitude and time scales as shown in part a.

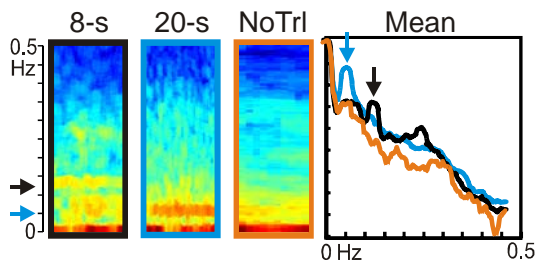


**Figure 2.29. Power spectra.**

Same data set as in Figure 2.15. **Left:** with moving window, over full sequence of 8-sec (black), 19-sec (blue) trials and 'No Trl' i.e. sitting in darkness with no trials or juice (orange). Colour-coded arrowheads, left pointing to frequency bands: 8-sec = 0.125 Hz; 19-sec = 0.05 Hz. **Right:** mean power spectrum over entire sequence, same colour code. Arrowheads show peaks for the different trial frequencies, over  $1/f$  baseline. Note hint of intrinsic periodicity<sup>44</sup> at  $\sim 0.05$  Hz in NoTrl case.

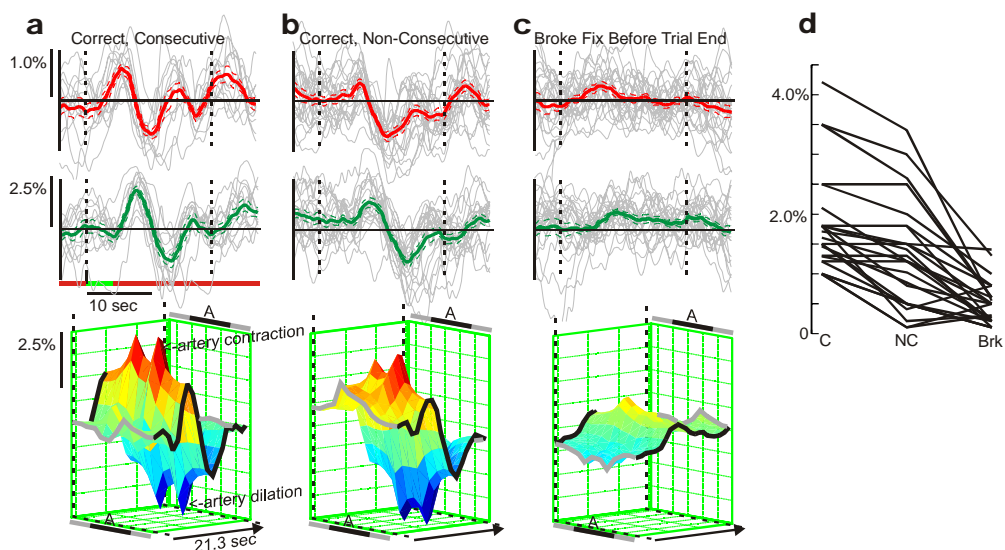


**Figure 2.30. Cortical signal amplitude correlates with performance on fixation task.**

Same experiment as in Figure 2.11 c-f. **a: 'Correct, Consecutive'**: (3 or more consecutive correct trials;  $n=13$  trials). **top, middle**: mean cortical signals. **Bottom**: time course of image profile (530 nm) under test line sampling an artery ('A') and its flanking parenchyma. Note parenchyma baseline (black outline) matching the mean signal, with a sharp arterial contraction–dilation cycle riding over it. Conventions as in Figure 2.13, e. **b: 'Correct, Non-Consecutive'**: ( $n=22$  trials). Weaker arterial cycle. **c: 'Broke Fix Before Trial End'**: (Broke fix prematurely after starting trial;  $n=25$  trials). Almost no arterial cycle. The 'Correct, Consecutive' and 'Correct, Non-Consecutive' were subsets of the 51 correct trials shown in Figure 2.11, f; 6 trials (not shown) occupying the 2<sup>nd</sup> position in consecutive sequences had intermediate amplitudes. **d**: Population distribution of mean peak-to-peak amplitudes for subsets of correct consecutive ('C'), correct non-consecutive ('NC') and premature fix break ('Brk') trials over 35 experiments.

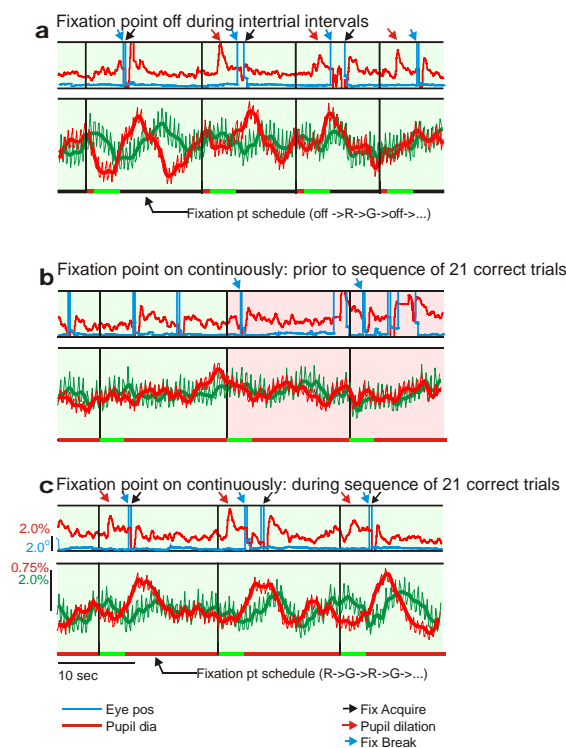


**Figure 2.31. Cortical signal and behavioural response in experiment where monkey S first learned the task.**

At this point in his training the animal had learned an earlier version of the task with fixation point turned off to cue intertrial intervals. On being presented with the new task (fixation on continuously, cueing trials by colour change) his performance was poor initially with multiple fixation breaks and few correct trials; his V1 signals and pupil dilation were weak. At one point in the experiment, he suddenly started performing correctly; there was one large pupil dilation, larger than any earlier, following which he executed a string of 21 correct trials during which we once again started seeing large trial-linked signals in his V1. **a:** Continuous recording of the animal's eye fixation and pupil trace (top) and mean V1 signals (bottom) for fixation sequence where the fixation point was off during intertrial intervals, turned on (red: 'ready') followed by green ('trial on, hold fixation'). **b:** Same day, when the animal was first exposed to the fixation schedule with fixation point on continuously. **c:** Later in the same block of trials as in part b, during the sequence of 21 consecutive correct trials.

## Chapter 4.

### COLLINEAR INTERACTIONS AND FILL-IN BETWEEN ORIENTED LINES IN PRIMARY VISUAL CORTEX

#### *4.1. Introduction to the Chapter*

Our visual system effortlessly groups together visual elements lying on common contours, an important step in segmenting complex scenes into objects. Here we show that primary visual cortex (V1) displays the long range orientation- and collinearly-tuned interactions required for such pre-attentive perceptual grouping. Using psychophysics we establish that monkeys group objects perceptually like humans. With optical imaging in the alert animals we show that individual line elements evoke co-axially elongated response basins in V1, activating collinear orientation columns. Nearby line elements interact nonlinearly across their overlapping V1 response basins, with interaction strength tuned for collinearity, proximity and relative orientation. The cortical response zones fill in the retinotopic gaps between elements when they are aligned along smooth contours. Further, this collinear cortical fill-in is amplified preferentially on extending contours by adding distal visual elements. These results demonstrate the involvement of V1 in pre-attentive processes of collinear grouping and contour integration.

## *4.2. The Anatomy and Physiology of V1 that Likely Underlie Contour Grouping*

### **4.2.1. Psychophysical Investigations of Contour Grouping**

Perceptually linking together line elements that lie on a common contour is an important first step in identifying objects[94] within complex visual scenes and plays a crucial role in the perception of their higher order properties (e.g. closure[95]; orientation in space[96]; matching features in natural scenes[97]). Many psychophysical studies have examined the nature of such perceptual linking as a parametric function of the geometrical arrangements of the line elements relative to each other.

From psychophysical observations, we know that the threshold for detecting a low-contrast line element improves if it is placed between a pair of iso-oriented collinear flanks[98, 99]. This improvement in the detection threshold decreases parametrically with increasing orientation difference, as well as with greater separations between the central element and the flankers[100]. Similarly, contours composed of line elements are most readily segmented from noisy backgrounds if the elements are closely spaced, aligned and iso-oriented[101, 102]. Segmentation performance deteriorates progressively as the contour is bent, or as its elements are misaligned or separated[103]. This perceptual salience of smoothness or collinearity appears to be automatic, 'popping out' from complex backgrounds without the need for directed attention or specific tasks[104, 105]. Both the facilitation in the detection of individual elements as

well as entire contours has been attributed to collinearly-tuned intra-cortical interactions in early visual areas.

These psychophysical results make specific requirements of any cortical machinery responsible for contour segmentation. Individual line elements must have collinearly elongated basins of interaction – ‘Association Fields’ – linking them to adjacent elements of similar orientation[103]. Further, computational models predict that these basins of interaction should chain along smooth contours, thereby amplifying the strength of association between individual elements[47, 106].

#### **4.2.2. The Architecture of V1 is Consistent with a Role in Contour Grouping**

The anatomy of V1 – with neurons connected via long-range collaterals of the appropriate spatial extent and orientation tuning – suggests an important role in collinear perceptual grouping[107-111]. However, there are key differences between the V1 of different species that make it difficult to draw generalized inferences about function on structural grounds. In new world primates (such as the tree shrew), horizontal connections are dramatically elongated along co-axial retinotopic dimensions[107]. This anatomical pattern is similar to the collinear connectivity schema proposed based on psychophysical measurements in humans. However, the visual systems of these animals are markedly different from those of old world primates, such as macaques and humans, including

having ocular dominance arranged by cortical layers rather than across the cortical surface[112]. In macaques, any anisotropy of horizontal connections is dominated by elongations across ocular dominance columns with no apparent collinear elongations[44]. Despite this lack of any clear anatomical correlate in old world primates, to the elongation of the 'association field', the presence of such a collinear connectivity schema is assumed in most models of human contour extraction[106, 113]. It is possible that the gross elongation of connections across ocular dominance columns in old world monkeys simply hides the finer-scale co-axial elongations[111], but such a hypothesis has little explicit evidence thus far.

#### **4.2.3. Physiology of V1 and Perception**

Physiologically, the role of V1 in pre-attentive perceptual grouping remains unclear. V1 neurons responding to disparate oriented lines can influence each others' firing through suppressive or facilitative geometrically tuned interactions[100, 114, 115]. Though adding collinear flanks enhances the responses of some neurons to preferred stimuli in their classical receptive fields (CRF), an almost equal number show suppression[100, 115, 116]. Further, although human psychophysics shows evidence of perceptual fill-in between collinear flanks[117], there is little physiological evidence of the same[118], possibly because the usual measuring technique (extracellular spikes) is insensitive to weak or subthreshold modulations. The few studies that have

measured subthreshold as well as spiking responses over large populations – using optical imaging, though in anesthetized animals – find extended orientation-tuned subthreshold activation[42, 93]. But these studies failed to find collinear interactions or tuned fill-in, including in the tree shrew (despite its prominent collinear anatomical connectivity in V1)[119].

#### ***4.3. Experimental Evidence for Collinear Interactions and Fill-In between Oriented Lines in Primary Visual Cortex***

We used a combination of psychophysics and optical imaging in alert monkey to explore the neural basis of collinear perceptual grouping. Using perceptual tasks based on detecting a low contrast line element embedded in flankers of various geometries, we established that monkeys had responses very similar to humans. Using optical imaging in the same monkeys, alert but engaged in passive fixation tasks rather than active detection tasks, we showed that V1 has physiological activation patterns appropriate for pre-attentive collinear perceptual grouping and contour processing.

##### **4.3.1. Psychophysics of collinear grouping is similar between monkeys and humans**

To look for evidence of perceptual collinear grouping in our monkeys we tested them on two tasks analogous to ones used in human psychophysics. Both tasks were based on measuring the effect of collinear surrounds on the ability to detect low contrast short lines; one task was structured as a 2-alternative forced choice

discrimination task while the other as a detection task. Human subjects show very different effects of collinearity in these two tasks[117]. We wanted to see if our monkeys displayed the same effects of collinearity, including the distinct responses to the two tasks. Further, most psychophysical evidence of collinear grouping in these tasks is based on foveal visual stimuli. Results from peripheral visual regions have been more variable[120, 121]. Since our optical imaging required stimuli to be at an eccentricity of a few degrees, we needed to establish that physiological measurements at this eccentricity could be compared with results from human psychophysics.

In human subjects asked to detect a low contrast line target, the presence of proximal collinear flankers robustly facilitates detection when the task is presented as a two-alternative forced-choice[98, 99]. To test whether collinear flankers improve monkeys' performance in a similar task context, we trained our animals to perform a two-alternative forced-choice discrimination task. The target stimulus – a  $0.25^\circ$  line element of variable contrast close to the threshold for detection – was shown at a visual eccentricity of  $2-3^\circ$ , on one side or the other of the display screen while the monkey held fixation. The monkeys had to report which side of the screen had the target. Adding collinear flankers to both sides of the screen significantly improved the monkeys' performance (Figure 4.1a). This improvement was larger for collinear than for orthogonal flanks (Figure

4.1a), maximal for adjacent flanks and reduced progressively with target-flank separations (data not shown).

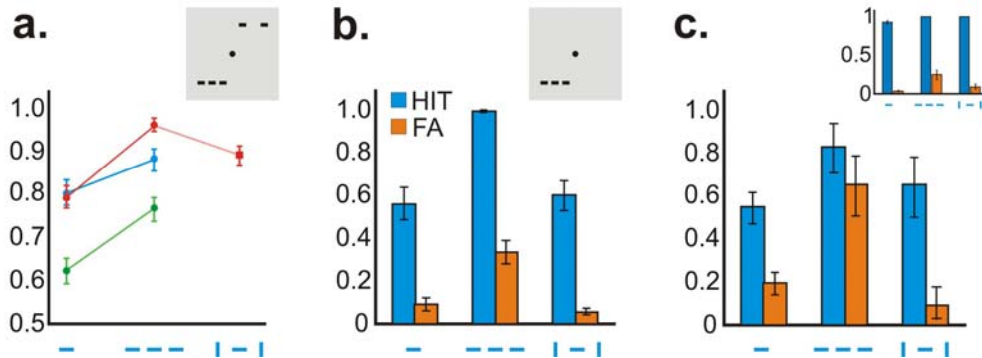


**Figure 4.1. Contour grouping is similar for monkeys and humans.**

**a.** Probability of correctly detecting a small 0.25 deg oriented line in the presence or absence of flankers of the same contrast in the spatial 2AFC task. On each trial, stimuli with and without a central line were shown in symmetric locations around the fixation point while the animal held fixation (see inset). The animal had to then indicate which side contained the central line. The colours represent different monkeys. Icons along the ordinate show the stimulus configuration tested, (i.e. single bar vs. no stimulus, or collinear triplet vs. collinear flanks, or orthogonal triplet vs. orthogonal flanks; see methods for details of stimulus contrast etc). **b-c.** Hit and false alarm (FA) rates when the same stimuli were presented in a 'yes-no' detection task at a single location. On each trial, a stimulus with or without a central line was presented while the subject (human: 1b or monkey: 1c) held fixation (see inset, b). Subject had to then indicate whether or not a central line was present. 'Hit's are correct reports of the presence of a central line; 'FA's were responses where the subject reported a central line on a trial when none was present. **c: inset:** On the same task, but with high contrast bars the monkey made very few FA errors with any stimulus configuration Error bars are SEM.

Despite the well-established facilitation of low-contrast target detection by collinear flankers in 2AFC tasks, similar flankers selectively induce a large number of errors when the detection task is structured differently. Thus, when human subjects are asked to report the presence of a low-contrast target line that always appears (or not) at a fixed location but with variable flankers from trial to trial, proximal collinear flankers induce the largest number of false alarm (FA) errors; i.e. subjects falsely report the presence of a target line on trials where none are present.[117]. This has been interpreted as a perceptual filling-in of the central element induced by the collinear flankers. To show that macaques demonstrate similar behaviour, and are thus likely to have similar functional circuitry, we measured FA rates in a single quadrant detection task. We assessed how FA rates changed for the different flank configurations. As with human observers tested on a similar task, we found a dramatic increase in FAs for collinear flank configurations, suggesting a similar underlying perceptual processing (Figure 4.1b,c). When the same detection task was presented with target and flankers at high contrast, the animal's performance pattern was very different; collinear flankers now induced the best performance and few FA errors (inset, Figure 4.1c) thus verifying that FA errors made by the animal in the low contrast detection task were not due to any confusion about the nature of the task.

Note that even though these psychophysical tests were carried out on the same two monkeys from whom we gathered physiological data (along with a third animal, as yet not imaged), all physiological measurements reported below were made before any perceptual training. This was done to ensure that the physiological results would reflect a pre-attentive baseline of cortical processing in the naïve animal.

#### **4.3.2. Responses to isolated short lines are elongated collinearly**

To look for a neural correlate of collinear perceptual grouping in the physiology of V1, we measured the spatial relations between V1 point spreads (PSs) evoked by short line elements (flashed, stationary  $0.25^\circ \times 0.04^\circ$  lines at  $\sim 3^\circ$  visual eccentricity). These line elements – singly, or in various geometric combinations – were presented to two macaque monkeys trained to maintain fixation while being shown the visual stimuli. The PS was visualized in the alert monkeys with intrinsic-signal optical imaging, known to reflect the combined spiking and subthreshold neuronal activation[93, 122]. Specifically, we imaged the absorption of light at 530 nm, a haemoglobin (Hb) isosbestic point (equal absorption coefficients in deoxygenated and oxygenated Hb), thus utilizing the blood volume (total Hb) signal. We took the percent increase in light absorption (percent increase in total Hb) over background as our measure of stimulus-triggered cortical activation. To remove any trial-linked signals we subtracted the responses to blank trials interleaved with each stimulus trial.

The PS from a single short line element ( $0.25^\circ$  long – comparable to the minimal V1 receptive field size at this eccentricity) had a number of characteristics suggesting that it reliably reflected the stimulus-evoked neuronal activation (spiking plus subthreshold) despite being an indirect measure (Figure 4.2). The PS extended about 4 mm in cortex (radius of the 10% contour line). Only the central 5% of this PS (i.e. within the 95% contour line) is likely to show spiking neuronal responses with classical high-contrast bar stimuli[93]. The overall cortical extent agrees, however with the anatomical extents of both the intrinsic long-range connections within V1 and the feedback from V2[123-125], that presumably mediate the cortical spread of stimulus-related activation. Despite the large cortical area activated, the optical signal emerged and rose to its peak intensity with a common time course over the entire extent of the PS (Figure 4.2b-e; Supplementary Movie 1). Further, though the extent of the PS corresponded to more than 2 deg of visual angle on V1, the cortical location of the PS peak

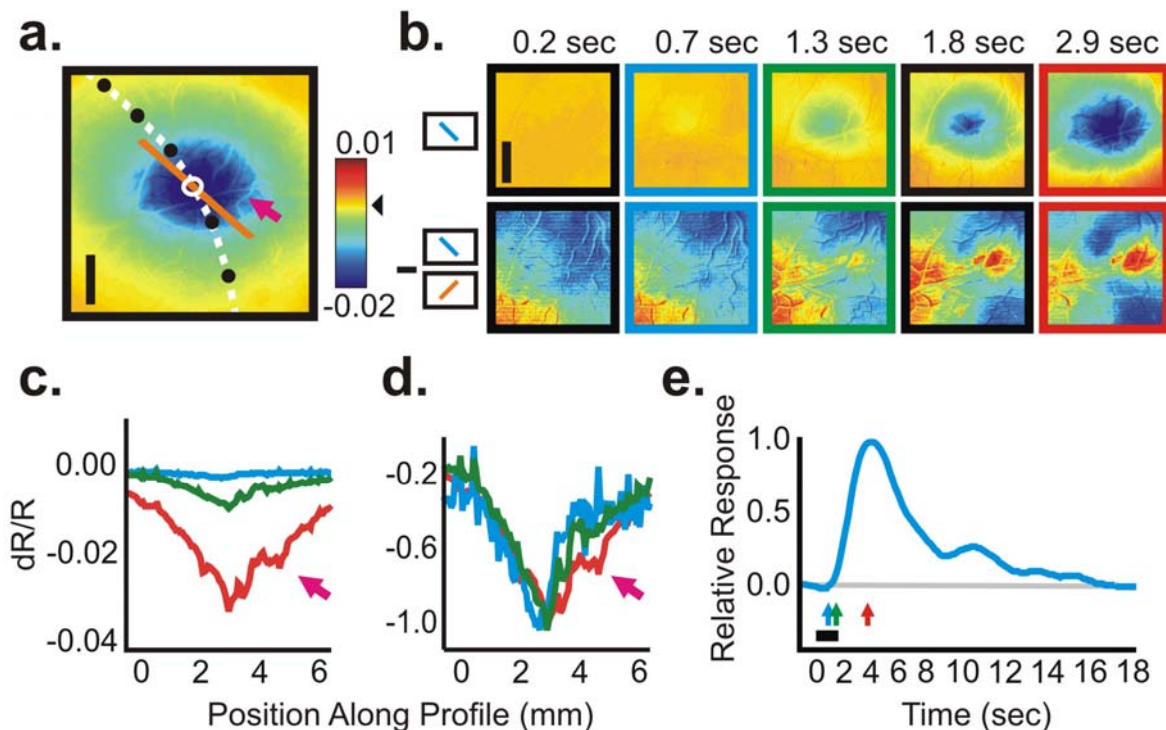


**Figure 4.2. Spatial extent and time course of the cortical pointspread (PS) in V1.**

**a.** The PS of a single 0.25 deg line, orientation 135 deg, presented for one second, colour coded by amplitude of cortical signal (fractional change in reflection off cortex; see colour bar, right). White oval contour marks the outline of the 95% response level. Orange line gives the image profile examined in **c** and **d**. Pink arrow points to a blood vessel contributing to an artefact in the profile. The white dotted line shows the 135 deg retinotopic projection axis on V1, with black circles marking centres of PS's from stimuli separated by 0.65 deg of visual angle (PS's not shown). **b.** Left to right; the temporal evolution of the signal in to a single line (top) or a difference between two orthogonal lines (bottom). **c.** Profiles of cortical signal taken at three time-points (0.7, 1.3, and 2.9 sec) colour coded with corresponding outlines in **b**. Pink arrow points to a distortion caused by a blood vessel artefact. **d.** The profiles in **c** scaled to a common amplitude. **e.** PS time course, measured by calculating the regression of the peak image (2.9 sec frame) with the signal at different time-points. Arrows mark the time-points examined in **b**, **c**, and **d**. Black line marks

stimulus ON. Scale bars are 2mm in all images.

showed fine retinotopic shifts ( $0.35^\circ$ ) matching shifts in stimulus position (Figure 4.7). The overall shape of the PS was asymmetric (ratio of major to minor axes [space constants of exponential fits]:  $2.5 \text{ mm} / 1.2 \text{ mm} = 2.03 \pm 0.05$ ,  $N=28$ , 2 monkeys<sup>6</sup>). This reflects the well known local asymmetry of cortical magnification[126] (and anatomical connection patterns), with the axis of elongation lying across the local ocular dominance pattern, independent of stimulus orientation (Figure 4.8). Note that our PSs closely matched those obtained using voltage sensitive dyes[41, 42], which image neuronal membrane depolarization (Grinvald et al. 1994: elongated PS, with an intensity distribution well fit with exponentials, of reported space constants  $2.9 \text{ mm}$  [major axis] /  $1.5 \text{ mm}$  [minor axis] , giving an anisotropy = 1.9).

Even though the overall size and extent of the cortical PS were independent of stimulus orientation, we saw, at a finer spatial resolution, a prominent collinear orientation-tuned modulation of the PS profile (Figure 4.3). This was most evident on looking at PS differences between a pair of orthogonal lines, as exemplified by the difference between a  $45^\circ$  and a  $135^\circ$  PS at the same location (Figure 4.3a). At their peaks the PSs had a similar overall magnitude, but with a patchy orientation difference pattern that closely matched, locally, the full-field

---

<sup>6</sup> Here the N refers to the number of experiments performed that showed similar results and the number of monkeys in which the tests were conducted is stated.

orientation map (Figure 4.3b). Outside this central region the PS from the  $45^\circ$  line showed an elongated ridge of higher signal extending outwards along the  $45^\circ$  retinotopic axis on cortex (at a 10% amplitude consistent with orientation mapping signals[35]). Correspondingly, the  $135^\circ$  PS showed an elongated ridge of higher signal along the  $135^\circ$  axis. Thus the difference signals at different visual locations looked like bow ties on the cortical surface, centred with fine retinotopy at the cross hairs of each orthogonal pair of lines and extending out along their respective collinear axes (Figure 4.3c. N=7, 2 monkeys). This 'bow tie' was an order of magnitude stronger and more extended than any retinotopic difference expected between the cortical activations by the two orthogonal lines (Figure 4.9). We checked whether these 'bow tie' ridges of increased signal were, in addition, biased in their orientation tuning. By superimposing the PS difference map over the V1 orientation map we found that the  $45^\circ$  ridges preferentially activated  $45^\circ$  orientation columns while  $135^\circ$  ridges preferentially activated  $135^\circ$  columns (Figure 4.3d. N=4, 1 monkey). PS regions away from these retinotopic ridges showed no bias in their orientation tuning. Finally, the 'bow tie' emerged over its entire cortical extent at a rate that matched the time course of individual line PSs, supporting our contention that it reflected neuronal responses integral to the activation evoked by oriented line elements (Figure 4.2b).

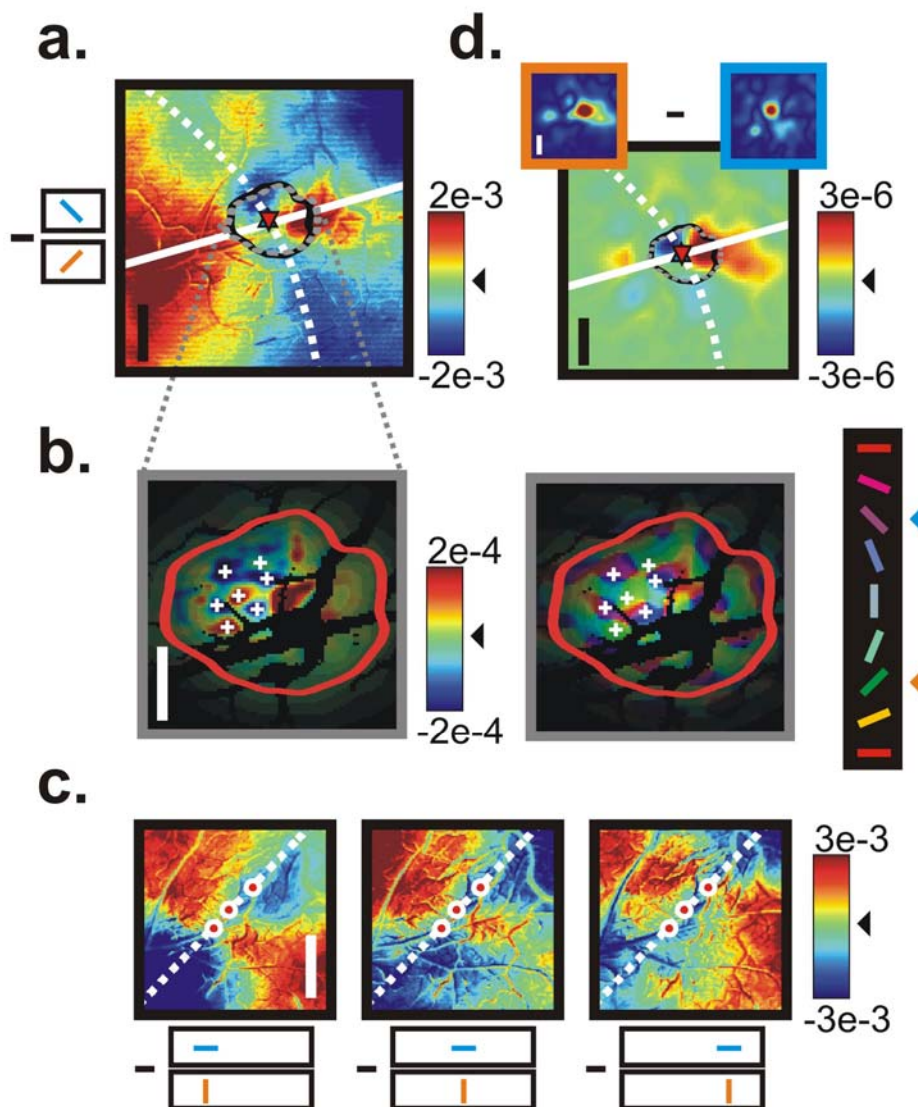


**Figure 4.3. Pointspreads of short single lines show orientation-tuned coaxial modulation.**

**a.** Cortical PS of a  $45^\circ$  line subtracted from the PS of a  $135^\circ$  line at the same location in space (see icon on left). Raw signal with no spatial filtering. Colour coded for strength of  $(45^\circ - 135^\circ)$  difference signal (red:  $45^\circ$  dominates, blue:  $135^\circ$  dominates; see colour bar). Retinotopic projection lines on cortex shown in white (solid:  $45^\circ$ ; dotted:  $135^\circ$ ). Centres (triangles) and 50% contours (solid:  $135^\circ$ , dashed gray:  $45^\circ$ ) shown for comparison. **b. Left;** enlarged view of difference image near peak of PSs, high pass filtered (Gaussian  $\sigma = 156 \mu\text{m}$ ). White crosses mark

centres of domains dominated by  $45^\circ$  (red) or  $135^\circ$  (blue; see colour bar). **Right;** Orientation map, windowed locally by intensity profile of PSs. White crosses mark the same locations as on the left. Note their match with  $45^\circ$  and  $135^\circ$  orientation columns (see orientation colour code, right). 50% outlines of PSs shown in both images, for comparison. Continuous black regions: masks covering blood vessels. **c.** Left to right: ( $45^\circ - 135^\circ$ ) PS difference images, centred at 3 locations at  $0.35^\circ$  separations. Circles mark PS centre points. White dashed line: horizontal axis on V1. **d. Top-left;** PS difference signal overlaid on  $45^\circ$  columns of orientation map (see methods). **Top-right;** same, but for  $135^\circ$  orientation columns. **Bottom;** the result of subtracting the images on the top. Red:  $45^\circ$  signal dominates, blue:  $135^\circ$  dominates (see colour bar). Scale bars are 2mm for a,c, and d; 1mm for b.

#### 4.3.3. Nonlinear interactions between lines are tuned for smooth contours

To measure collinear grouping in V1 we then investigated the effect, on the cortical response, of embedding the single central line element between a pair of collinear flank lines. The cortical response to the resulting triplet was found to be reduced dramatically relative to the sum of the individual responses to centre and flanks, in a manner that revealed strong coaxial interactions between them (Figure 4.4; N=13, 2 monkeys). Our measure of nonlinearity in the cortical response – defined as the response to the triplet minus the sum of responses to the ‘centre alone’ + ‘flanks alone’ – reduced systematically on shifting the flanks off the triplet axis (Figure 4.4a-c, g; N=4, 2 monkeys); on rotating the flanks (Figure 4.4d-f, h; N=4, 2 monkeys) while maintaining centre-to-centre separations; or on moving the flanks further apart, disappearing by  $3^\circ$  of separation from the centre bar. (Figure 4.5e; N=4, 2 monkeys).

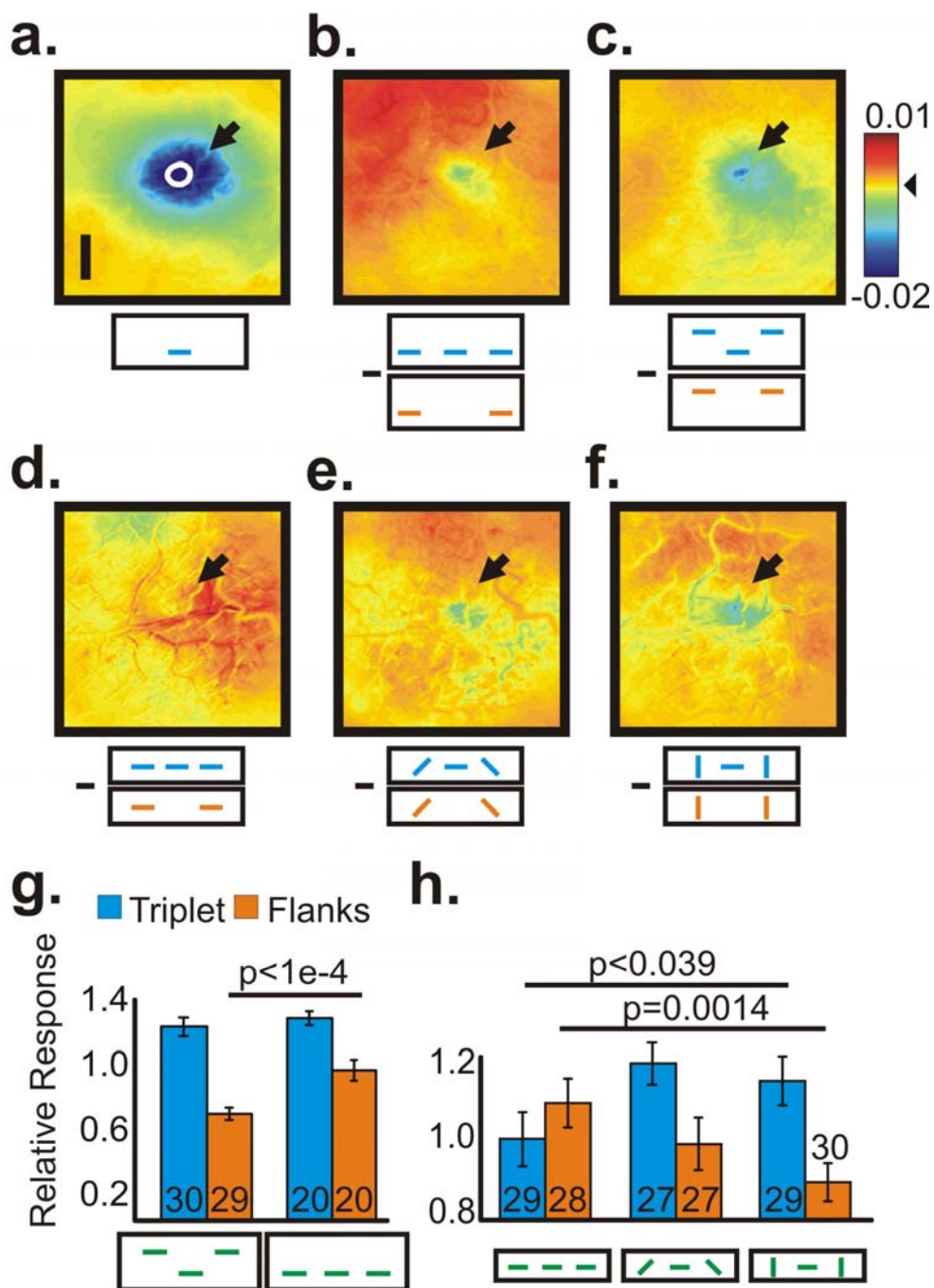


**Figure 4.4.** Nonlinear interactions between oriented lines are tuned for collinear configurations.

**a.** Cortical PS to a horizontal line presented alone ('centre'). White oval contour marks the outline

of the 95% response level taken as the retinotopic position of the centre line. All quantitative comparisons were made on signal measured in this oval test region (see g,h) **b**. The response difference between the centre line presented between two collinear flank lines (separation of 0.49°) and the flanks presented alone. Arrow: the small signal difference at the retinotopic location of the centre line. **c**. Same as b, but with the flank lines shifted off the collinear axis by 0.3 deg while maintaining centre-to-centre separation. **d-f**. Same as b, but as the flank lines are rotated off the collinear from left to right. **g**. The average cortical signal evoked within the oval test region by the triplet and flank stimuli, expressed as a fraction of the response to the centre alone. Numbers inside the bars represent the number of trials used in the calculation. **h**. Same as g, but for d-f. Scale bar is 2mm. Error bars are SEM; p-values are from Kolmogorov-Smirnov tests applied to across-trial signal distributions.

This nonlinearity reflected a neuronal interaction between centre and flanks and not a hemodynamic nonlinearity since it was evident only when centre and flanks were flashed on simultaneously (Figure 4.10). With centre and flank flashed on asynchronously with a 150 ms gap, enough to disrupt the percept of a collinear triplet but brief compared to the time scale of hemodynamic response, the nonlinearity was much reduced. Further, the observed nonlinearity could not be due to a simple neuronal saturation since it was present during the full timecourse of the response, and even for low stimulus contrasts that produced weaker cortical activation (Figure 4.11).

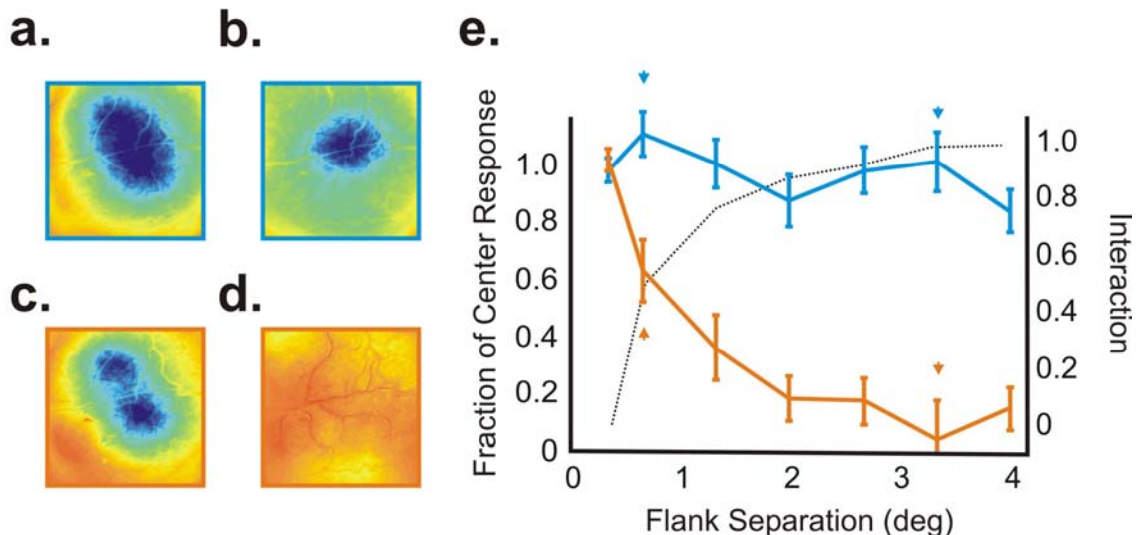


**Figure 4.5. Nonlinear interactions are tuned to nearby flank separations.**

**a-d.** Responses to triplets (top row) and flanks alone (bottom row) for a  $0.7^\circ$  (left column) and  $3.3^\circ$  (right column) flank separations. **e.** Responses at the centre location for the triplet configuration (blue) and flanks alone (orange) as a function of flank separation. Dashed line plots the difference between triplet and flank responses presented as a fraction of the centre response alone. A value of 1 indicates no interaction. Error bars are SEM.

We wondered how much of the observed ‘nonlinearity’ in the triplet was due to a (mutual) suppression between flanks and centre, and how much due to the flanks ‘filling-in’ the gap between them and thereby reducing any additional contribution of the centre to the full triplet. To identify the independent contributions from these two components we measured the signal in the gap between the flanks while varying their angular and axial arrangement. We found that the flanks alone generated a signal that reduced progressively as the flanks were rotated off collinear, or shifted off axis, suggesting a flank-induced

collinear ‘fill-in’ contribution to our observed nonlinearity (Figure 4.4g, h). Note that the ‘fill-in’ signal from collinear flanks can be larger than the signal with the centre line present (Figure 4.4h). Further, as the flankers were pulled apart, the response at the centre location in the triplet configuration did not change appreciably (Figure 4.5a,b,e) while the response in the gap with flankers alone reduced progressively with flanker separation (Figure 4.5c,d,e). The tuning of the flank signal as a function of flank orientation, offset, and separation was thus distinct from that of the triplet signal. This suggests that there could be two separable functional components to the cortical interactions amongst collinear groups of line segments: a tuned collinear fill-in, along with a mutual collinear suppression – or possibly, some form of a cortical ‘Max’ operator that always reaches the same level of total activity – each with distinct geometric tuning.

#### **4.3.4. Collinear interactions are chained along elongated contours**

Finally, we investigated whether extending the contour would enhance our observed nonlinearity selectively for collinear contours, as predicted by models of contour segmentation [106, 113]. In particular, we wondered if our observed ‘fill-in’ would strengthen in an orientation selective manner as we extended the contour by adding line elements to the distal ends. We compared the responses to a stimulus consisting of only a single pair of flanks (collinear or orthogonal to their centre-to-centre axis, separation of  $1.3^\circ$ ) with stimuli consisting of the same central pair with chains of similar lines extending out on either side (6 elements

each direction; inter-element separation of  $0.65^\circ$  Figure 4.6a, c). These large inter-element separations were chosen to avoid possible saturation of the 'fill-in' signal. The central pair of flanks alone gave a 'fill-in' that was weak and poorly tuned for flank orientation. On extending the flanks outwards with chains of distal line elements the 'fill-in' increased dramatically – but disproportionately much more for the collinear flanks, giving the 'fill-in' a prominent collinear orientation tuning (Figure 4.6b, d, e). The increased 'fill-in' observed for collinear flankers was not a linear retinotopic consequence of the relative shapes of collinear vs. orthogonal line elements (i.e. of the fact that collinear lines extend slightly further into the gap regions than orthogonal lines). Even when the two orthogonal flank chains were shifted to the innermost edges of the corresponding collinear flank lines, thus reducing the effective gap, we still observed greater 'fill-in' for the collinear configuration (Figure 4.6f).

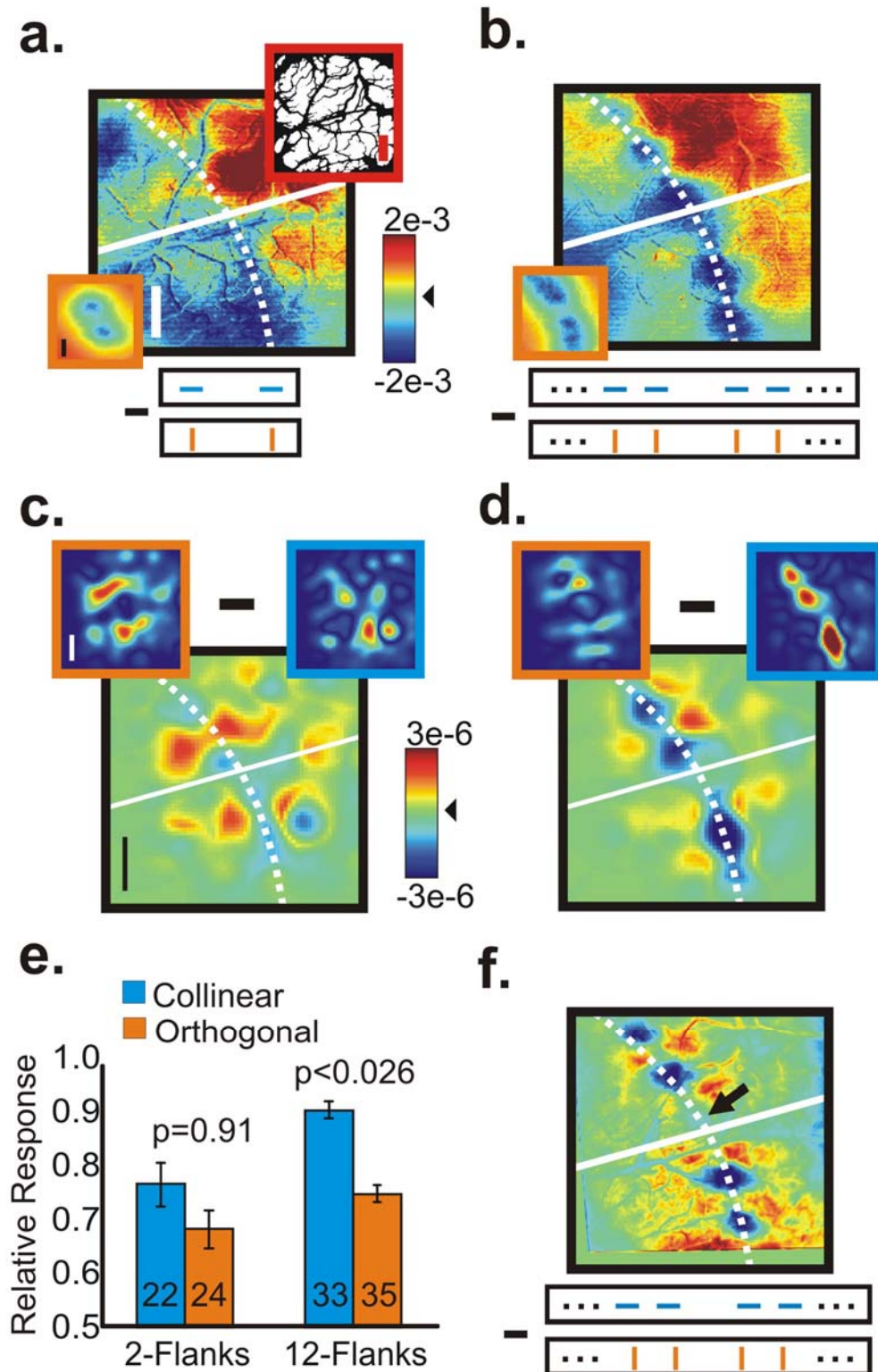


Figure 4.6. Collinear interactions are chained along smooth contours.

**a.** Difference between PSs evoked by pairs of collinear ( $135^\circ$ ) vs. orthogonal ( $45^\circ$ ) lines spaced by  $1.3^\circ$ . Blue areas: greater cortical signal for collinear, red areas: greater signal for orthogonal; see colour bar. **Inset: Bottom-Left:** the raw signal pattern evoked by the two bars (collinear: but indistinguishable, at this scale, from orthogonal). **Top-Right:** Map of the local vasculature. **b.** Same as a, but with the addition of distal flank lines. **c. Top-left;** difference signal from panel a overlaid on  $45^\circ$  columns of orientation map (see methods). **Top-right;** same, but for  $135^\circ$  orientation columns. **Bottom;** the result of subtracting the images on the top. Red:  $45^\circ$  signal dominates, blue:  $135^\circ$  dominates (see colour bar). **d.** Same as c, but for data in b. Note the overall increase in response bias toward the collinear. **e.** Fill-in, expressed as a fraction of the response to a single line for the different stimulus combinations in a and c. Numbers inside the bars represent the number of trials used in the calculation. **f.** Same as c, but with the orthogonal lines centred on the inner edge of the collinear lines. Note that fill-in is still larger for collinear bars (arrow). Data are from a different test day aligned using vasculature. All scale bars are 2mm. Error bars are SEM; p-values are from Kolmogorov-Smirnov tests applied to across-trial signal distributions.

#### **4.4. Discussion:**

Using a combination of perceptual psychophysics and intrinsic-signal optical imaging in alert behaving macaques we have compelling evidence for a number of elements proposed earlier, on theoretical grounds, as critical to contour integration[98, 101]. First, we find that monkey psychophysics closely matches human psychophysics in standard detection tasks used to demonstrate collinear grouping. With detection presented in a 2-alternative discrimination task, monkeys – like humans – show a selective benefit with close collinear flanks. But

as with humans, collinear flanks selectively induce a large incidence of false-alarm errors – i.e. a false report of the presence of a collinear target line when none was present – in monkeys engaged in a yes-no detection task. With intrinsic-signal optical imaging from the V1 of the same monkeys (but while naïve, before psychophysical testing) we find a number of physiological correlates that could account for the psychophysics of pre-attentive collinear grouping and contour integration. In the PS imaged from a single line element we find an extended ridge of interaction, tuned to the line orientation, which is remarkably similar to that line's proposed 'Association Field'[101]. Adjacent line elements show collinear interactions in their PS's, including a collinear 'fill-in' of any gaps between them; further, these pair wise interactions cascade, as predicted, selectively along smooth contours[106, 113]. It is possible that imaging in the alert monkey was critical to our being able to see these predicted elements of contour processing that had eluded earlier imaging studies in anesthetized animals [42, 119]. Parenthetically, the interactions we measure – while tuned for collinearity – show no overall collinear facilitation, appearing at first glance inconsistent with the tuned facilitation seen in spiking measurements[100, 115, 127]. But the increase in spiking observed earlier may be due to a change in the relative balance of excitation and inhibition which may not be reflected in the overall metabolic demand – and the optical imaging signal – an issue that needs to be explored.

Importantly, the present study – by using optical imaging, which measures subthreshold as well as spiking responses [93, 122] – points to the prevalence of collinear interactions across the population of V1 neurons in a manner that was not possible using earlier electrode recordings. Our recordings visualize the cortical distributions of the ‘Association Field’ and collinear fill-in. These likely reflect largely subthreshold modulatory changes in cell membrane voltage, particularly for the longer intracortical separations. Further, we show that collinear interactions characterize V1 responses to line segments over the neuronal population, even during passive fixation outside any task context. By contrast, earlier electrode recordings of collinear interactions in V1 during passive fixation found strong collinear facilitation but also almost an equally large fraction of neurons that were suppressed[100]; collinear facilitation was found to dominate V1 responses – in a manner that correlated with a contour’s perceptual saliency – only when the perception of the contour was behaviourally relevant[127].

These findings of collinear V1 interactions even during a passive fixation task indicate the presence of a ‘pre-attentive’ circuitry that operates early in the visual processing stream (V1, but possibly including feedback from higher areas) to rapidly perform collinear integration. This ‘pre-attentive’ mechanism may then form the base for the more complex neuronal responses that reflect perceptual learning[128], behavioural performance[127, 129], task context[130] or

attention[131], or the perception of complex features such illusory contours[132], contour closure[95] or extraction of foreground vs. background[133]. Our experimental technique thus opens up the rich possibility of imaging while the animals are engaged in specific perceptual discrimination tasks in order to study the role of this circuitry in these more complex perceptions.

#### 4.5. Additional Figures:

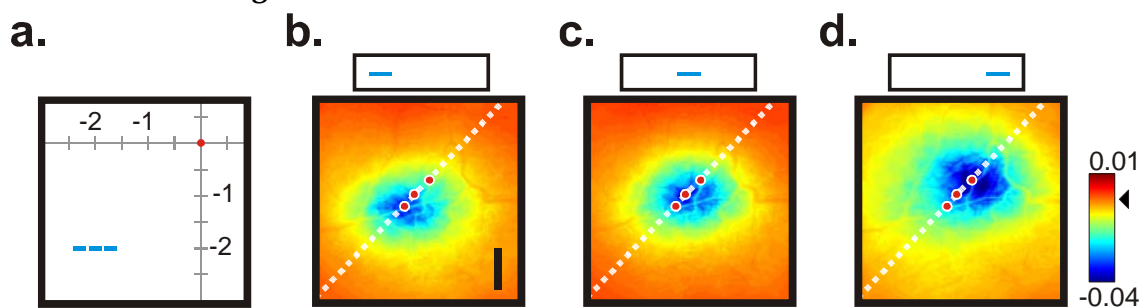


**Figure 4.7.** The pointspread to a line segment shows fine retinotopic shifts on cortex.

**a.** Schematic of the visual display, showing positions of three line stimuli, shifted along the horizontal in 0.35 deg steps toward the fovea (red dot in the upper right). **b-d.** Average PSs at three locations in **a**. Red circles mark the center points of each PS. White dashed line: horizontal axis on V1.

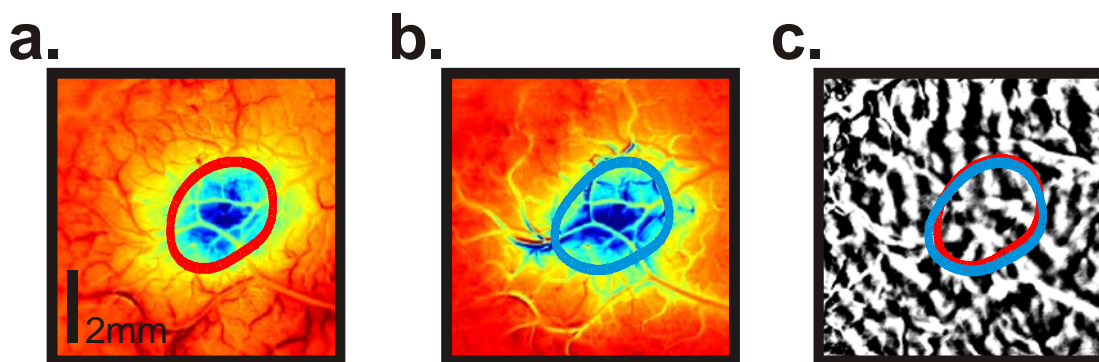


**Figure 4.8.** Pointspreads are elongated orthogonal to local ocular dominance columns, independent of line orientation, reflecting local anisotropy in cortical magnification.

**a.** The pointspread evoked by a horizontal line stimulus, and the associated 50% response contour. **b.** Same as **a**, but for a vertical line. **c.** Contours from **a** and **b** overlaid on the local ocular dominance map.

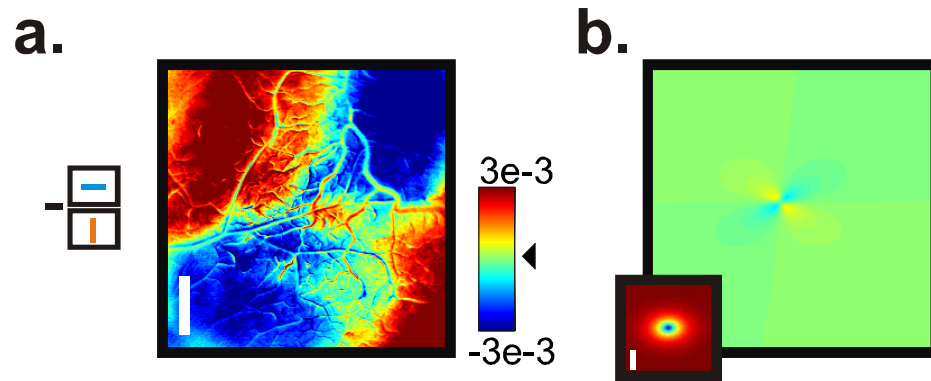


**Figure 4.9. Co-axial differences between bars are an order of magnitude larger than any expected retinotopic differences.**

**a.** Subtraction of the PS to a vertical line from that to a horizontal line. **b.** The expected retinotopic response difference arising solely from the difference in shape between the two lines. First, we calculated the projection of the lines onto the cortical surface using a local measure of cortical magnification derived from the local retinotopic map. We then fitted a 2D exponential model PS that, when convolved with the cortical projection of the lines best fit the observed response for both bars (inset). Subtracting the convolution of the PS with the vertical line projection from that with the horizontal demonstrates the entirely retinotopic response difference between the lines.

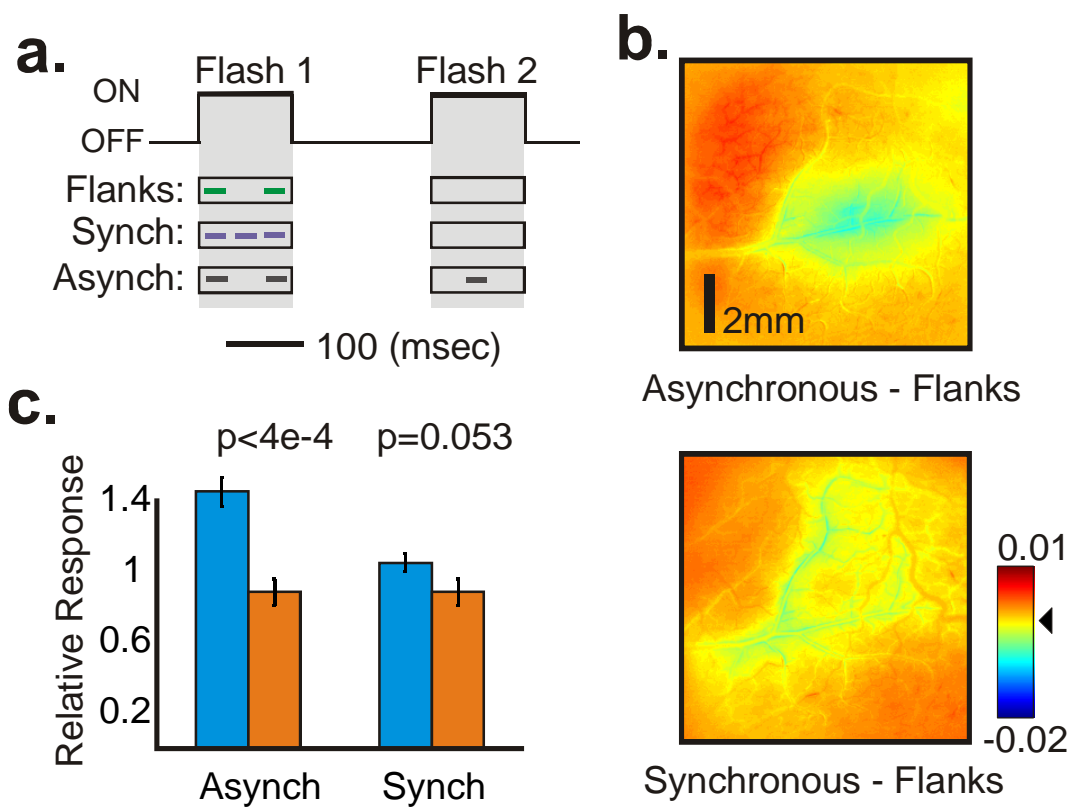


**Figure 4.10. Asynchronous presentation dramatically reduces the interaction between lines.**

**a.** Three temporal presentation sequences of the center line and the flank lines. **b.** The activity difference image between asynchronous (Asynch) line presentation and flanks alone (top) is stronger than the 'synch' and flank lines alone (bottom). **c.** Cortical signal at the center test location (see Figure 4.3g,h) evoked by synchronous and asynchronous presentation of center and flanks. The 'flank alone' value is repeated for comparison.

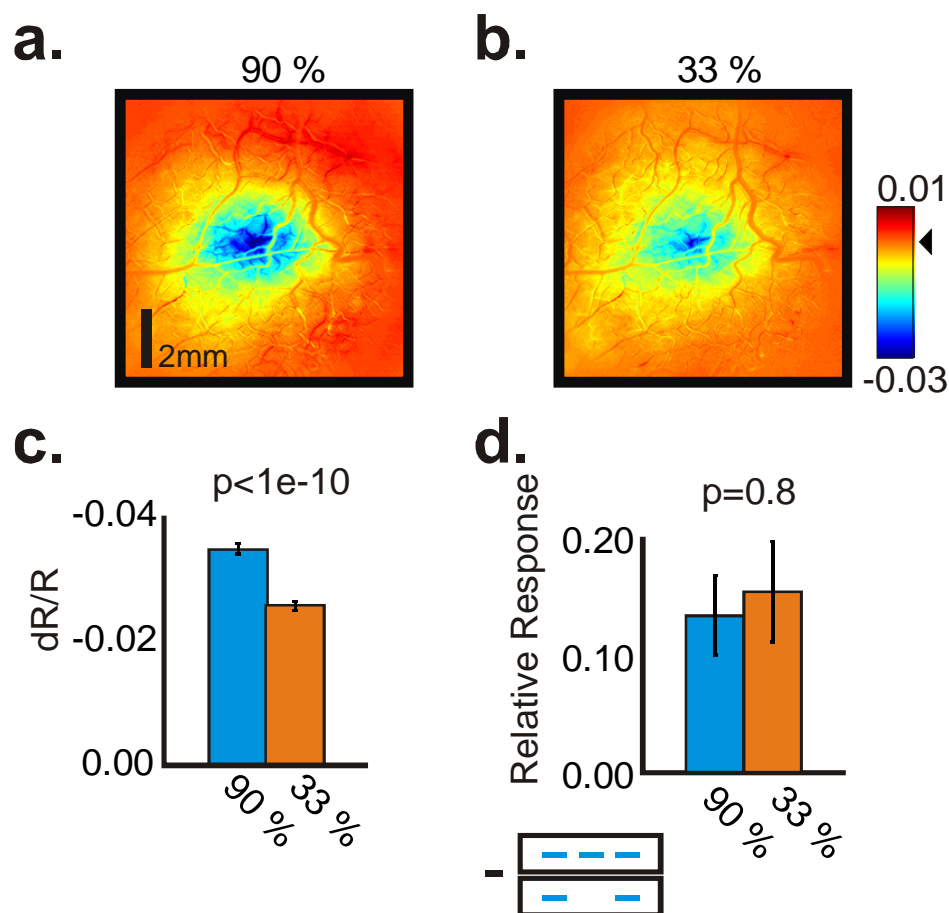


**Figure 4.11. Bar interactions are invariant across contrast.**

**a, b.** The cortical activations (PSs) observed for a 90% and 33% contrast 0.25 deg center lines respectively. **c.** The signal amplitudes (fractional change in reflection off cortex) from images in a and b. **d.** The difference in cortical signal evoked by center lines and flank lines for the two contrast levels expressed as a fraction of the center response at that contrast.

## 4.6. Methods

### 4.6.1. Psychophysics

Stimuli for imaging and psychophysics were displayed on a linearized Sony GDM-F520 monitor driven by the VSG 2/5 board from Cambridge Research Systems. Psychophysical measurements were carried out in three monkeys and in

humans. Before all experiments at low contrasts, we ensured that the monkeys learned the task by requiring near-perfect performance for full contrast configurations. Detection performance for the central element was first assessed over a range of contrasts. When assessing the effect of flank geometry, both the flanks and the centres were presented at a contrast that yielded near 75% correct performance for the 2AFC task and near 50% performance for the detection task. Because the animals' performance varied from day to day we did not always achieve the desired level of performance for the centre alone. We could assess whether collinear flankers changed performance relative to the centre alone as long as the centre detection was significantly worse than 100%.

#### **4.6.2. Stimuli (for both psychophysics and optical imaging)**

Stimuli were composed using custom software written in MATLAB (MathWorks, Natick MA) and presented using custom software (BehavCtrl; Appendix II) written for use with the VSG (Cambridge Research Systems, Kent England) graphics co-processor and an A-D board (National Instruments, Austin TX). During optical imaging, to assure that the long-lived hemodynamic response to a stimulus from the preceding trial does not interact with future responses we interjected a 6 second inter-trial interval along with blank trials (trials with no stimulus presented) between each stimulus-containing trial. During the course of any experiment, we also included additional blank trials on which a stimulus was not presented that were likewise flanked on either side by blank trials.

These were used to compensate for the overall trial-related pattern of the hemodynamic response (see below).

#### **4.6.3. Optical imaging: tasks:**

Results were obtained using continuous, intrinsic-signal optical imaging in two monkeys engaged in a visual fixation task. On each trial, the animals were simply required to hold fixation on a small fixation point (0.08-0.15 deg, fixation window 0.75 deg) over a cued duration (at least 4 sec) for a juice reward, ignoring any visual stimuli shown during the cued fixation period. Eye position was monitored with an infrared tracker[50]. Note that all the optical imaging data reported here were obtained in the naive animals, prior to psychophysical testing.

#### **4.6.4. Optical imaging: Surgery, recording chambers, artificial dura:**

After the monkeys were trained on visual fixation tasks, craniotomies were performed over the animals' V1 and glass-windowed stainless steel recording chambers were implanted, under surgical anaesthesia, using standard sterile procedures[17]. The exposed dura was resected and replaced with a soft, clear silicone artificial dura. After the animals had recovered from the surgery, cortical activity from their V1 was optically imaged through this recording window, routinely, while the animals engaged in relevant behavioural tasks. Recording chambers and artificial dura were fabricated in our lab using published methods[51].

#### **4.6.5. Optical imaging: Data acquisition**

Standard alert-monkey optical imaging techniques<sup>[17]</sup> were used. Images were acquired on a Dalsa 1M30P camera (1024 x 1024, 30 frames / sec, but typically binned to 256 x 256, 15 frames / sec), through a Optical PCI Bus Digital Frame Grabber (Coreco Imaging, Boston MA) imaging board, using software developed in our lab based on a system by V. Kalatsky[52]. Illumination was provided by high-intensity LEDs (Agilent Technologies, Purdy Electronics; Appendix I), synchronized to the camera acquisition frames. We used LEDs centred at 530 nm (close to an isosbestic point for Haemoglobin, i.e. absorbed equally in oxygenated and deoxygenated Haemoglobin) acquiring images at a frame rate of 7.5 frames / sec. The light from the LEDs was filtered through small individual interference filters (Omega Optical) mounted on each LED. A 'macroscope' of back-to-back camera lenses[53] (Nikon, assorted fixed focal lengths), focused on the cortical surface, was used for imaging. Images of the cortex were acquired at 7.5 Hz and combined into movies.

The monkeys were trained to maintain fixation for at least 4 seconds, during which, line stimuli were presented for 1-1.5 seconds at  $\sim 3^\circ$  eccentricity in the lower visual field (inter-stimulus-interval  $\geq 18$  seconds).

#### **4.6.6. Optical Imaging: General Data Analysis Steps**

The images were processed using custom software written in MATLAB (Image Processing Toolbox). All images were first 'shift-corrected' to correct for any

residual movement of the cortical surface that remained despite the specially designed camera mount, animal head post and overall structural framework. This 'shift-correction' consisted of aligning each image frame to the first frame of a given experimental session, using the imaged blood vessels as references. Each image frame was cross-correlated with the reference frame, and a gradient descent method used to maximize this correlation value as a function of lateral shifts in the image position, frame by frame. These 'shift-corrected' images were then used for all subsequent processing.

The functional data was analyzed as follows. For each stimulus condition and trial, we generated a movie of the average cortical activity changes triggered on the onset of the stimulus. The data were temporally low-pass filtered (cut-off frequency of 1Hz) to remove the pulse artefact. To compensate for the uneven illumination over cortex each image frame was divided by a spatially low-pass filtered image of the overall cortical reflectance. The pre-stimulus period was then subtracted on a trial-by-trial basis (5 frames immediately prior to stimulus onset), thus giving us a measure of percent signal change. From each stimulus-triggered movie, we subtracted the blank trial average movie to remove non-stimulus related hemodynamic patterns. To generate images of activity patterns associated with each stimulus, we averaged 10 frames around the peak of the stimulus related activity (typically 3 seconds after stimulus onset). For statistical analysis, we selected regions of interest (ROIs) and obtained trial-by-trial

measures of average activity within a given region and subtracted the mean activity across the entire region to remove trial-by-trial fluctuations in response. This greatly reduced the variability of the measured responses within the ROI. We chose the Kolmogorov-Smirnov test because the overall distribution of responses was not normal, with a fat tail toward lower responses.

*Visualizing Orientation Columns and Bias.* Because the orientation signal is such a small fraction of the overall stimulus response to a bar ( $\sim 1\%$ ), we took advantage of the fact that the overall spatial scales of the responses were different. To isolate the orientation column signal (visible near the peak of the PS: Figure 4.3b), we performed a high-pass spatial filtering (Gaussian  $\sigma = 156 \mu\text{m}$ ) and smoothing (Gaussian  $\sigma = 59 \mu\text{m}$ ) of the difference images between orthogonal bars to isolate the spatial component at the rough spatial scale of orientation columns ( $\sim 100 \mu\text{m}$ ). This was compared locally with the full V1 orientation map (obtained using standard methods: full field grating, 4 orientations; Figure 4.3b, right). To visualize the orientation bias over the entire extent of the PS we split the full orientation map into two complementary masks of orientation columns corresponding to the two orthogonal bars (i.e.  $45^\circ$  and  $135^\circ$  masks for Figure 4.3, comprising regions of  $45^\circ \pm 22.5^\circ$  and  $135^\circ \pm 22.5^\circ$  respectively). We then projected the magnitude of the orthogonal-bar difference image separately through each mask to identify the spatial distribution of orientation biases in the image. The resultant bias maps were then smoothed by convolving with a Gaussian ( $\sigma = 468$

$\mu\text{m}$ ; Figure 4.3d, insets top left, right). To avoid blood-vessel artefacts we excluded regions with large blood vessels from these calculations.

All experimental procedures were performed in accordance with the NIH Guide for the Care and Use of Laboratory Animals and were approved by the Institutional Animal Care and Use Committees (IACUC) of Columbia University and the New York State Psychiatric Institute.

## Chapter 5.

### CONCLUSION

Imaging of intrinsic signals correlated with neuronal activity is the most commonly used method to study patterns of network activity in the brain. However, despite the prominence of these signals in the literature, relatively few studies focus on understanding the relationship of these signals to neuronal activity [134]. Many imaging studies work around our lack of understanding with clever experimental techniques expected to specifically modulate neuronal activity. However, our poor understanding of cerebral hemodynamics confounds investigations focusing on a finer spatial scale (e.g. [23, 135]). This chapter summarizes the specific contributions of this thesis to both our understanding of cerebral hemodynamics and fine-scale activity patterns associated with contour extraction in V1. The chapter concludes by discussing future research directions.

#### *5.1. The Scientific Contributions of this Thesis*

The aim of this thesis was to study population level activity in V1 associated with contour extraction. However, prior imaging work did not provide sufficient evidence for the appropriate intrinsic signal to study responses to spatially localized stimuli in V1 of alert monkeys. Previous studies in monkeys used only full-field stimuli and work using rodents was inadequate because of differences

in anesthesia, system (barrel or somatosensory cortex), stimulus delivery method (electrical shocks or whisker deflections), and species. Furthermore, even in the studied systems, the relationship between neuronal activity and hemodynamics remains poorly understood [5, 10, 43]. Therefore, the first part of this thesis laid the experimental foundation for discriminating between and choosing the appropriate intrinsic signal for studying patterns of activity across V1. Chapter 2 demonstrates that changes in cerebral blood volume are a superior assay of such activity patterns because they are more reliable and interpretable than oxymetric changes, which result from competing influences of blood volume, oxygenation, and flow (each of which have different spatial structures).

Another challenge in interpreting intrinsic signals from alert animals is our poor understanding of cerebral hemodynamics associated with behavior, which is largely because most prior work used anesthetized preparations. Using simultaneous electrophysiology and optical imaging in awake macaques, this thesis demonstrates the presence of large hemodynamic fluctuations independent of any sensory stimulation that appear to be a hereto unknown process of anticipatory resource allocation in the brain. Similar signals have been observed using fMRI in humans; however, without the ability to simultaneously record neuronal activity, it was impossible to determine whether any signals observed result from local neuronal activity (via classical mechanisms) or remote modulation of cortical vasculature. This anticipatory

signal confounded the spatial activity profiles of any measured visual response. Experiments presented in Chapter 3 characterize this anticipatory signal in detail, show that it is independent of visual stimulation and neuronal firing, and that it is separable from any classical stimulus-driven responses.

This thesis culminates with the application of the new understanding of cerebral hemodynamics described in Chapters 2 and 3 to studying patterns of neuronal activity in V1 associated with smooth contours (Chapter 4). The apparent optimization of the visual system for segmenting complex natural scenes into discrete objects (or 'Gestalten') has long been noted and 'Gestalt' psychologists supposed that such computations take place soon after the relay of information from the LGN [136]. Indeed, as reviewed in Chapter 4, the primary visual cortex appears to have the necessary architecture to support the process of contour extraction, the putative first stage of object extraction.

However, detection of contours in natural scenes is a complex process. Contours in natural scenes are seldom continuous, with many interruptions and occlusions [97]. Because of this, the assignment of individual elements of complex scenes to specific contours often does not have unique solutions and any given contour element may have several contours to which it can be assigned. This means that the visual system must calculate some likelihood of connection between segments before picking a specific grouping. This process is generally thought to

involve long-range synaptic communication between neurons across the cortical sheet. However, capturing the nature of these communication patterns has so-far proved difficult and few studies have addressed the question directly [100, 115, 119, 127, 129, 137, 138]. The typical technique used in prior studies was single unit electrophysiology, which only measures supra-threshold changes in neuronal output (but see Chisum). Because of this limitation, it has been impossible to determine the effect of stimulus geometry on the entire neural population and observe synaptic communication across the cortical sheet proposed, on theoretical grounds, to underlie grouping.

This thesis adds to our understanding of contour grouping by presenting the first evidence of the cortical extent of responses to small contour elements along with their tuning for orientation and co-axial elongation. Further, Chapter 4 shows how these, likely subthreshold, response elongations bridge any gaps between elements making up contours and alter responses to simultaneous feedforward input from the LGN in a manner consistent with the process of extracting smooth contours.

## *5.2. Future Directions*

This thesis is a step along the way to developing better techniques of assaying neural activity patterns in alert animals and improving our understanding of

cortical function and organization. The data presented in this thesis open the door to a number of future studies.

The properties of the hemodynamic pointspread discussed in Chapters 2 and 4 raise a number of interesting questions about the relationship between stimulus-driven neuronal activity and the hemodynamic response. The large spread of the hemodynamic signal across ocular dominance columns suggests an active neuronal process. However, the spread of the hemodynamic response to small stimuli (covering nearly 10 mm of V1; Figure 2.4) is much larger than the expected extent of spiking activity [93]. Together with the comparable activity spreads observed using voltage sensitive dyes, these data suggest that the hemodynamic spread is likely subthreshold in nature. However, the source of the subthreshold spread could be either from local horizontal connections in V1 or from feedback from V2 [124]. Knowing the sources that contribute to specific components of the activity spread in V1 can specifically establish whether any response interactions between multiple elements (Chapter 4) are due to intrinsic processing within V1 or result from feedback from higher areas. Determining the influence of selective inactivations of V2 and other higher areas on the pointspread and inter-stimulus interactions observed in V1 could help answer this important question.

Chapter 4 demonstrated orientation tuned co-axial activity fill-in between collinear lines in V1 and their role in nonlinear interactions between stimulus responses across V1. These observations may be evidence for a general active process by which neurons share information about stimulus features across visual space to extract salient visual objects. To investigate this hypothesis further, future work can focus on other perceptual phenomena that involve active computations in V1, such as extraction of illusory contours and detection of texture boundaries.

In addition, the active fill-in of activity observed for specific stimulus geometries may be correlated with perception (Figure 4.1; [139, 140]). Chapter 4 demonstrates that both monkeys and humans are likely to generate false alarms when detecting a short line if that line is flanked by two collinear lines. This perceptual behavior is remarkably similar to the activity fill-in observed between responses to collinear flank lines in V1 (Figure 4.4) and highlights the intriguing possibility of a causal relationship between this activity modulation and the generation of false alarms. This relationship could be tested by performing simultaneous imaging and psychophysics and trial-by-trial comparisons between the degree of fill-in observed using imaging and the probability of false alarm generation.

Any future investigations relating responses to behavior must carefully consider the role of anticipatory signals (Chapter 3), which could confound the interpretation of any results obtained. The experiments carried out in Chapter 4 were done prior to the animal learning any psychophysical tasks and while they were actively discouraged from attending to the peripherally presented stimuli. Under these conditions, the trial-related signals appear to be similar from trial-to-trial and can be removed by a simple subtraction. However, trial related signals are modulated by the subjects' arousal and attention (Figure 2.31; [68-71]), which makes a simple subtraction of the average trial-related response an inadequate control. Trials corresponding to poor behavioral performance may correspond to periods of lower arousal or ineffective allocation of attention linked to lower preparatory activity in V1. Therefore, to interpret relationships between stimulus responses and perception, it is first necessary to characterize and account for any relationship between stimulus responses and the preparatory signals.

In addition to understanding the links of preparatory signals with behavior, the source of these signals should also be investigated. As discussed in Chapter 3, these signals are likely generated by a central mechanism and relayed to V1 by neuromodulatory input. To test this hypothesis, local pharmacological manipulations that selectively enhance or inactivate specific neuromodulatory systems (esp. cholinergic and catecholaminergic) should be conducted. The

effects of these manipulations on the preparatory signal should provide valuable insight into any neuromodulatory systems involved in its generation.

In summary, future studies should focus on understanding the source of the hemodynamic activity patterns characterized in this thesis and their relationship with behavior and perception. Relating the activity patterns observed in V1 and perception could give important insight into the role of V1 in object extraction. However, any future work in alert animals would greatly benefit from a detailed understanding of the intrinsically generated hemodynamic responses, which remain largely unexplored due to a focus on anesthetized preparations.

## Appendix I.

### DETAILS OF THE SPECTROSCOPIC ILLUMINATOR CIRCUIT

In order to effectively separate intrinsic signals into separate components due to oxygenation and volume, it is necessary to simultaneously acquire signals at several wavelengths. In order to achieve this goal, I designed a novel LED based illumination system allowing rapid switching between several illumination wavelengths in synch with the imaging camera. This appendix describes the details of this illuminator, which was used to gather the data presented in this thesis.

#### *A. The Physics of Measuring Intrinsic Signals*

When analyzing intrinsic signal optical imaging data, the measured quantity is the change in the amount of light reflected by the cortex towards the camera. Changes in the amount of light reflected toward the camera are largely determined by changes in the concentration of hemoglobin in the tissue according to the Beer-Lambert law:

$$I_R = I_O e^{-alc} \quad (1)$$

Where  $a$  is the absorptivity of the cortex,  $l$  is the length of the path traveled through the medium, and  $c$  is the concentration of the absorptive chromophore. In the simplifying case where hemoglobin and deoxyhemoglobin are the only chromophores undergoing change at wavelength  $\lambda$  we can write:

$$I_R = I_O e^{-\alpha_\lambda^{HbO} l_\lambda c_\lambda^{HbO}} e^{-\alpha_\lambda^{HbR} l_\lambda c_\lambda^{HbR}} \quad (2)$$

Because of this relationship, the amount of light absorbed and thus the amount of light being reflected is proportional to the amount of incident light at the surface. Thus, the optical signal is typically expressed as percent signal change from some starting value:

$$\ln\left(\frac{I_R^2}{I_R^1}\right) = \Delta \ln(I_R) = -\alpha_\lambda^{HbO} l_\lambda \Delta c_\lambda^{HbO} - \alpha_\lambda^{HbR} l_\lambda \Delta c_\lambda^{HbR} \quad (3)$$

Under such conditions, in order to measure signals most reliably, it is desirable to maximize  $I_O$  and thus maximize the signal change.

### ***B. Illuminating the Cortex Homogeneously***

The delivery of light into the optical imaging chamber is, however, problematic. Most implementations use one or two light sources positioned around the chamber and pointing toward the center. This produces a highly inhomogeneous distribution of light and narrows the region from which reliable signals can be measured. In order to overcome such limitations, I designed an LED based illuminator geometry that produces a homogeneous illumination profile across the imaged region, thus maximizing the signal-giving area.

The illuminator can be simultaneously loaded with two garlands LED garlands with different wavelengths. To acquire signals at both wavelengths

simultaneously, I designed a circuit that strobes the two LED garlands across alternate frames of the imaging camera (Figure I.1).

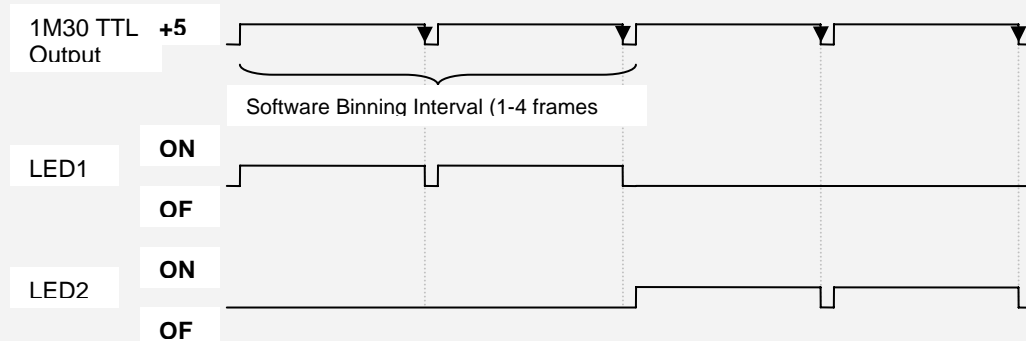
### Figure I.1: LED CIRCUIT FOR REAL-TIME SPECTROSCOPY AND STROBING

**Purpose:** To change the wavelength of light on each binned camera frame and turn off the light during frame readout. This circuit works for switching two wavelengths, but should be expandable.

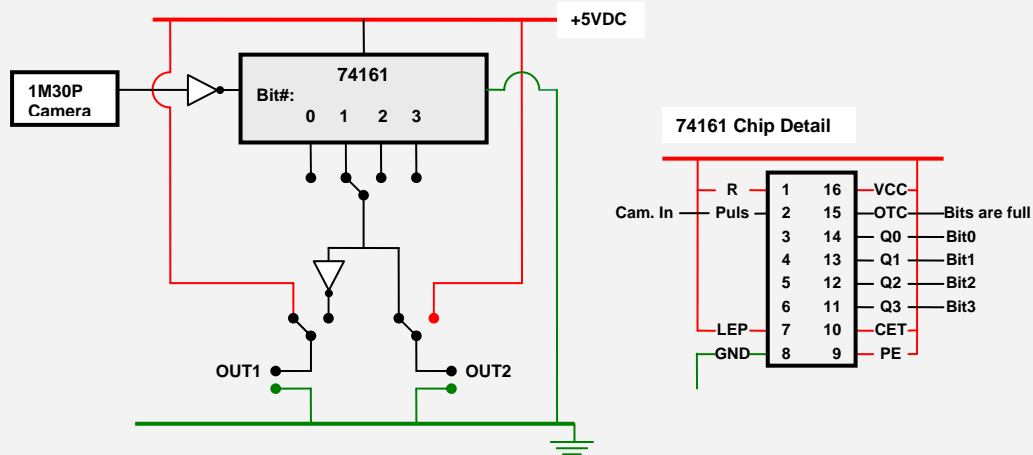
The DALSA 1M30 puts out a TTL pulse (via SMA connector on the chassis) that is HIGH when the camera is integrating and LOW when it is in readout mode (~1msec). The software may be set to bin every one, two, or more frames together, thus it is important to have the hardware match the software settings and switch the light every appropriate number of frames.

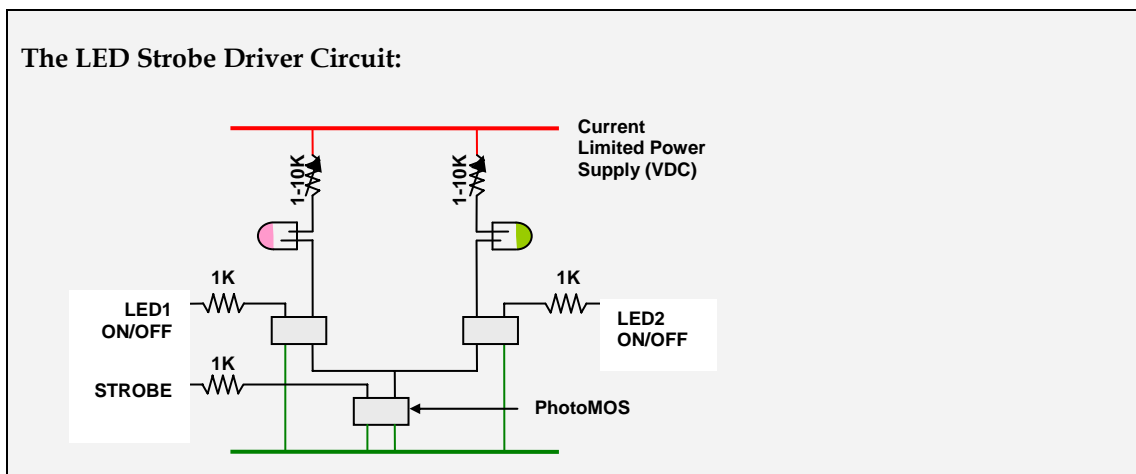
#### Parts:

1. LS74161 counter chip to track the rising incoming TTLs
2. LS7404 TTL inverter chip (for flipping camera's TTL polarity so that the counter tracks the falling edges)
3. RF PhotoMOS (AQY221N3V) from Panasonic to switch the LEDs on and off without leakage current
4. 2x 1-10k Variable Potentiometers for controlling LED brightness



#### The Counter Circuit:





This enables virtually simultaneous acquisition of both wavelengths with relatively homogeneous illumination profiles. The illuminator is attached to ports embedded in the acrylic around the imaging chamber and aligned with the top of the chamber during the implantation. After adjusting the height of the illuminator for the chamber, there is no further need to adjust light geometry, which saves valuable set-up time for experiments. To better control the wavelength emitted by the LEDs, each LED can be fitted with a small interference filter. In principle, this method can be extended to use more wavelengths with additional LED garlands added to the illuminator.

### *C. Important Details of Illuminator Design*

I faced several challenges in designing and implementing the illuminator circuit. In the first iteration of the circuit, I used transistors to gate the LEDs. However, transistors are highly sensitive to any current delivered to the base and, even with appropriate shunting to ground, some LEDs emitted a faint, but perceptible,

amount of light even in the off position. Replacing the transistors with optoisolators (Panasonic PhotoMOSFET) cured this problem by isolating the transistor from any gating current and essentially making it a voltage, instead of a current, gate.

The other major challenge was in synchronizing the LED circuit to the image acquisition software running on a computer. In order to display images of cortical activity online, the imaging software must know the wavelength identity of each incoming frame. In order to do this, the LED circuit has a digital wavelength output connected to the PC running the imaging software and the software polls this input upon acquisition of each imaging frame. Unfortunately, the imaging camera used (Dalsa 1M30P), does not have an onboard digital input that can be acquired in synchrony with each frame. This means that if the computer takes too much time in acquiring a given frame (frames are not acquired in real-time), the LED status may have already changed and an incorrect wavelength assigned to the acquired frame. The software, therefore, implements status checks to detect and correct for such inconsistencies. Running the camera at 15Hz with an appropriately fast hard drive, however, gives ample time for the PC to keep up with image acquisition in real-time. With future improvements in processing speed or with cameras allowing synchronized digital inputs, synchronization of the imaging software with the LEDs should not be a problem.

## Appendix II.

### BEHAVCTRL - AN INTEGRATED SYSTEM FOR BEHAVIOR CONTROL AND STIMULUS PRESENTATION

All of the data presented in this thesis was acquired using a custom-made data acquisition and behavioral control system developed by me in the lab. The goal of the system was to effectively control animal behavior by imposing trial structure, presenting a wide variety of visual stimuli, and gathering and synchronizing several physiological signals (including eye position, cortical absorption at several wavelengths, and electrophysiology). One of the challenges in designing a system for simultaneous data acquisition and stimulus presentation is the fact that typically used operating systems (OS; e.g. MS Windows), though multitasking, are not real-time. Thus, specific execution times of individual lines of code are at the discretion of the operating system and not the programmer (the OS scheduler must assign different concurrently running processes shared blocks of time on a single CPU). However, with the advent of multi-processor systems (esp. multi-core processors) it became possible to simultaneously evaluate several code statements concurrently, thus dramatically increasing the performance of programs that take advantage of this feature (i.e. multithreaded programs and parallelized code). This appendix describes my implementation of a multithreaded stimulus presentation and data acquisition system (BehavCtrl).

### *A. The threads and their functionality*

Any system for behavioral control, stimulation, and data acquisition must execute three fundamental functions: behavioral state and physiological signals must be monitored and recorded continuously, salient behavioral events and some physiological signals (e.g. lever pulls, eye position) must be displayed for the experimenter, and the system must react to behavioral events with appropriate responses (e.g. stimulus presentation upon fixation or reward delivery upon trial completion). In general these three functions are largely independent of each other and can be separated into individual processes to simplify code and make it easier to troubleshoot the application. For this reason, BehavCtrl is separated into three main threads: the main input/output (I/O) thread, the experiment thread, and the graphic user interface (GUI) thread.

#### **1. Main Thread - I/O, Timing**

At its core, BehavCtrl is a data acquisition system. The most critical function in BehavCtrl is the reliable acquisition of analog and digital data, which requires the use of an analog-to-digital (AD) board. In this case, the program runs with an AD board from Measurement Computing (PCI-DAS 1002). Because MS Windows is not a real-time system, it is difficult to ensure data acquisition at a given rate. Windows, however, allows the programmer to set aside locked memory pages with direct read/write access granted to specific attached devices. The PCI-DAS 1002 board takes advantage of this feature and presents and

interface for setting up and retrieving a handle to this locked memory (cbw32.lib).

The main data acquisition thread is created or destroyed from within the GUI thread when the user pushes the appropriate buttons. This allows modification of data acquisition parameters without requiring a restart of the entire program. The thread is basically a continuous loop that checks this memory at each cycle for new information and assigns it a timestamp based on the system time (Windows Multimedia Timer; 1 msec precision).<sup>7</sup> Because it is undesirable to access locked memory pages assigned to the AD board multiple times within a single cycle of the main thread (due to their volatility; i.e. the data is modified in real-time by the AD board), the main thread polls this memory only once and performs all subsequent operations on a local copy.

The main thread is responsible for determining whether the acquired behavioral data meets the criteria of specified behavioral events (e.g. the monkey pulled on a lever). If any events have been detected, the main thread posts a message to the appropriate other threads (see below) with the description of the behavioral event taken and its timestamp. Thus, after the main thread, it is no longer necessary to check for the presence of behavioral events from the raw data. The

---

<sup>7</sup> It would be ideal for the AD board to come with an on-board timer, however, the PCI-DAS-1002 board does not and it is therefore necessary to use timing information from the motherboard to timestamp incoming data. This means that several data-points may have share the timestamp of the last acquired point.

final function of the main thread is to inform the GUI thread that new data has been acquired so that any data displays for the experimenter could be refreshed.

## **2. Experiment Thread - Experiment Specifics (Object Based)**

The experiment thread is the simplest of the threads. It is created from the GUI thread whenever a new experiment is initialized and destroyed whenever the experiment is completed. The function of this thread is to wait for the occurrence of behavioral events (detected in the main thread), and to then execute an experiment-specific response to those events (e.g. pulling the lever turns on a fixation point). These experiment specific events are not hard-coded into the experiment thread. Instead, it uses a simple interface common to all experiment objects (described below). The experiment thread initializes with a pointer to any one of a number of experiment objects (i.e. different objects for different types of behavioral experiments). The experiment object is then initialized with some set of starting parameters (passed to the experiment thread). The thread waits in sleep mode for behavioral event messages from the main thread upon receipt, passes this event to the experiment object, which then executes a set of reactions to those events (i.e. turning a fixation point on or off).

Despite doing relatively little, the experiment thread performs a major function in BehavCtrl. By acting as a mediator between the behavioral events detected in the main thread and the experiment object, it abstracts any specifics of event

detection into a simple interface. This enables the experiment designer to come up with ever more complex paradigms by simply making classes that inherit the experiment interface and adding functionality without changing the underlying framework. Furthermore, this interface also controls access to variables shared across the three threads (see below) and prevents any deadlocks or state inconsistencies. Thus, once written, multiple experiments can be easily selected and executed within BehavCtrl without any modification of the underlying multithreaded code.

### **3. GUI Thread – User Interface, Stimulus Presentation and Configuration, Manual Controls, Data Recording**

The graphical user interface thread controls the rest and the bulk of the functions in BehavCtrl. This is the only thread that starts when BehavCtrl initializes and it is responsible for configuring all program settings, launching all other threads, displaying behavioral data to the experimenter, presenting stimuli to the experimental subject, and saving behavioral and physiological data to the hard drive for later analysis. In this appendix, however, I will focus only on features critical for stimulus presentation and the flow of information between the threads and to the hard disk.

The GUI thread interacts with both the main thread and the experiment thread. When the main thread runs, on every cycle, it posts a message to the GUI thread asking it to update the state of the application with the latest behavioral data.

Upon receipt of this message, the GUI thread copies the data buffer from the main thread to a local buffer and checks for any changes in relevant behavioral variables (i.e. the status of eye fixation). These updates are then displayed appropriately for the experimenter and, if an experiment is in progress, saved to the hard disk (the \*.eye file).

From the experiment thread executing a particular experiment object, the main thread receives requests to perform particular actions (i.e. reward delivery) and executes those actions. The experiment thread also informs the GUI thread upon the initialization or completion of individual trials and their outcome (correct, incorrect etc.). Additionally, this thread tracks the behavioral performance of the animal online and maintains statistics on how well the animal performs individual trials and, during a psychophysics experiment, how well the animal performs for any given stimulus presented. The information received from and actions requested by the experiment thread are all time-stamped based on the current system time (determined by the main thread) and saved in a separate file from data obtained directly from the main thread (the \*.bhv file). This file maintains an entry for each behavioral trial the animal performed, any behavioral events that have occurred during this trial, and the trial's outcome. Placing this data into a file separate from the continuous AD traces makes it possible to quickly analyze the animal's behavior without having to more slowly parse the larger \*.eye files.

Because training experimental subjects requires manual experimenter intervention, the GUI thread puts common actions (e.g. fixation point or stimulus on/off) requested by the experiment thread under the experimenter's control with both 'hotkeys' and on-screen buttons. The experimenter can also manually specify the stimulus to be presented to the animal on any given trial and change the behavioral events required for the animal to obtain a reward (e.g. making a saccade to a given fixation point).

BehavCtrl separates stimulus presentation from all other aspects of the experiment. Whereas timing and the general structure of the behavioral task is governed by the experiment thread, the cycling and drawing of stimuli is done in the GUI thread. This allows arbitrary match of stimulus to trial structure. The GUI thread has a comprehensive stimulus configuration utility powered by an object oriented interface that I developed for driving the VSG2/5 board from Cambridge Research<sup>8</sup> and the details of the implementation of this system are described later. The user can select the appropriate stimulus set to be presented to the animal during a given experiment and BehavCtrl cycles through the stimuli in the order desired by the experimenter. Whenever the subject correctly completes a trial with a given stimulus, BehavCtrl prepares for the next trial by

---

<sup>8</sup> Though this system is now relatively obsolete, because of the object oriented nature of the interface, it is possible to make the same system work with other graphics hardware by writing an appropriate library.

drawing the next stimulus. All drawing is done during the inter-trial interval and the actual presentation of the stimulus simply involves displaying the appropriate graphics memory page, thus minimizing delays.

The GUI thread has access to all the relevant information about the behavioral state of the animal and stimulus presentation. In addition to managing this information internally, BehavCtrl implements external communication with other components of the data acquisition system (the electrophysiology computer and the imaging computer). It does so by implementing both TCP/IP communications (ContImage software and FHC amplifier) as well as digital outputs (Plexon amplifier). These features allow BehavCtrl to synchronize and share data with any number of other systems.

For troubleshooting and reconstructing the time-course of events during a given experimental session, the GUI thread maintains an event log (saved to disk) which receives status messages from all three threads. This log contains time-stamped information about the details of the actions taken by the individual threads as well as the user and is valuable for evaluating the source and nature of any problems when they arise.

### ***B. BehavCtrl Objects***

In addition to taking advantage of parallel processing whenever possible, to make the code more modular and easily upgraded, I adopted a general object oriented framework for managing most program functions within BehavCtrl.

### *C. C++ wrappers for VSG graphics objects*

The VSG2/5 comes with an extremely basic driver library designed to be used in short standalone stimulus-specific programs. In order to usefully implement this system within a complete application such as BehavCtrl, I had to write a comprehensive object-oriented abstraction wrapper around the basic functions provided by Cambridge Research.

#### **1. CVSG**

CVSG is an object that encapsulates the VSG2/5 library and manages all interactions between BehavCtrl and the VSG board. It is the main VSG object and must be created prior to using the VSG board. Because multiple program threads may make drawing requests from the VSG board simultaneously, the CVSG object implements a critical section based locking scheme to ensure that only one request is processed at a time. Therefore, all drawing requests are routed through the CVSG object instead of being directly passed to the VSG library.

In addition to simply passing existing VSG library functions, the CVSG object has custom functions that simplify the operation of the VSG board and new

functionality can be added either by making classes that inherit from CVSG or by adding functions to the CVSG class.

As described in detail below, to simplify coding of novel stimuli and stimulus presentation, my implementation treats all stimuli as objects with specific drawing instructions. To keep track of any created graphics objects and make sure they are properly deleted upon program shutdown, CVSG keeps a list of all created objects and assigns them unique identifiers. Consequently, this allows other routines to obtain pointers to any existing graphics objects from CVSG.

## 2. VsgScene

Drawing graphics using the VSG board can be classified into two general operations. The step first involves setting up the appropriate drawing environment (i.e. memory page, background color, any overlays, etc) and the second involves the actual drawing instructions (draw oval, grating, animate palette, etc). The first set of instructions are quite general and do not tend to differ between different objects. Thus, to set up the VSG for drawing operations, I created the VsgScene object class.

Any drawing routine must first create a VsgScene and then add any number of drawing objects to it (described below; e.g. gratings). The VsgScene implements two important functions: **Draw** and **Show**. The **Draw** function cycles through all drawing objects added to VsgScene and executes their specific drawing instructions. VsgScene manages the memory pages on which the objects are

drawn and drawing is done on hidden pages prior to stimulus display. Once the stimuli have been drawn in off-screen memory, they can be displayed by calling the **Show** function which copies these memory pages to the screen as well as send out synchronization signals (via the AD board) and performing stimulus specific instructions (such as turning on palette animation for drifting gratings). To again hide the stimuli, show can be called with a 'false' flag. VsgScene can synchronize stimulus presentation with other computers, by sending either an IP command or a TTL pulse. For an IP command the function **SetIPMessage** can be used to set a specific stimulus ID sent when the stimulus is presented.

Different experiments demand different classes of visual stimuli and scene configurations (images, gratings, movies, etc.). To easily switch between setups, VsgScene objects can be quickly destroyed and new ones created in their place. Destroying the VsgScene also destroys any associated objects. Multiple VsgScenes can be active at once if they are instructed to draw on different pages within VSG memory.

### **3. VsgObject**

The VsgObject is a generic class from which all specific stimulus objects inherit. It is designed to specifically be used with the VsgScene and should be constructed with a pointer to the parent scene. The VsgObject class is paired with an VsgObjectSet. The VsgObjectSet is a class that summarizes the basic properties shared by all VsgObjects (e.g. position, color, contrast). The main

function of the `VsgObject` class is **Draw**. The **Draw** function is composed of three sub-functions: **DrawStart**, **DrawObject**, and **DrawEnd**. Of these, only **DrawObject** typically needs to be changed in classes that inherit from **VsgObject**. **DrawStart** sets the memory page on which the object will be drawn and sets up the VSG board based on properties specified in the **VsgObjectSet**.

## BIBLIOGRAPHY

1. Felleman, D.J. and D.C. Van Essen, *Distributed hierarchical processing in the primate cerebral cortex*. *Cereb Cortex*, 1991. **1**(1): p. 1-47.
2. Grinvald, A. and R. Hildesheim, *VSDI: a new era in functional imaging of cortical dynamics*. *Nat Rev Neurosci*, 2004. **5**(11): p. 874-85.
3. Waggoner, A.S., *Dye indicators of membrane potential*. *Annu Rev Biophys Bioeng*, 1979. **8**: p. 47-68.
4. Grinvald, A., et al., *Real-time optical mapping of neuronal activity in vertebrate CNS in vitro and in vivo*. *Soc Gen Physiol Ser*, 1986. **40**: p. 165-97.
5. Logothetis, N.K. and B.A. Wandell, *Interpreting the BOLD signal*. *Annu Rev Physiol*, 2004. **66**: p. 735-69.
6. Iadecola, C. and M. Nedergaard, *Glial regulation of the cerebral microvasculature*. *Nat Neurosci*, 2007. **10**(11): p. 1369-76.
7. Malonek, D. and A. Grinvald, *Interactions between electrical activity and cortical microcirculation revealed by imaging spectroscopy: implications for functional brain mapping*. *Science*, 1996. **272**(5261): p. 551-4.
8. Thompson, J.K., M.R. Peterson, and R.D. Freeman, *Single-neuron activity and tissue oxygenation in the cerebral cortex*. *Science*, 2003. **299**(5609): p. 1070-2.
9. Laughlin, S.B., R.R. de Ruyter van Steveninck, and J.C. Anderson, *The metabolic cost of neural information*. *Nat Neurosci*, 1998. **1**(1): p. 36-41.
10. Lauritzen, M., *Reading vascular changes in brain imaging: is dendritic calcium the key?* *Nat Rev Neurosci*, 2005. **6**(1): p. 77-85.
11. Fox, P.T., et al., *Nonoxidative glucose consumption during focal physiologic neural activity*. *Science*, 1988. **241**(4864): p. 462-4.
12. Fox, P.T. and M.E. Raichle, *Focal physiological uncoupling of cerebral blood flow and oxidative metabolism during somatosensory stimulation in human subjects*. *Proc Natl Acad Sci U S A*, 1986. **83**(4): p. 1140-4.
13. Raichle, M.E. and M.A. Mintun, *Brain work and brain imaging*. *Annu Rev Neurosci*, 2006. **29**: p. 449-76.
14. Sheth, S.A., et al., *Linear and nonlinear relationships between neuronal activity, oxygen metabolism, and hemodynamic responses*. *Neuron*, 2004. **42**(2): p. 347-55.
15. Malonek, D., et al., *Vascular imprints of neuronal activity: relationships between the dynamics of cortical blood flow, oxygenation, and volume changes following sensory stimulation*. *Proc Natl Acad Sci U S A*, 1997. **94**(26): p. 14826-31.
16. Sheth, S.A., et al., *Columnar specificity of microvascular oxygenation and volume responses: implications for functional brain mapping*. *J Neurosci*, 2004. **24**(3): p. 634-41.

17. Shtoyerman, E., et al., *Long-term optical imaging and spectroscopy reveal mechanisms underlying the intrinsic signal and stability of cortical maps in V1 of behaving monkeys*. J Neurosci, 2000. **20**(21): p. 8111-21.
18. Vanzetta, I., R. Hildesheim, and A. Grinvald, *Compartment-resolved imaging of activity-dependent dynamics of cortical blood volume and oximetry*. J Neurosci, 2005. **25**(9): p. 2233-44.
19. Madsen, P.L. and N.H. Secher, *Near-infrared oximetry of the brain*. Prog Neurobiol, 1999. **58**(6): p. 541-60.
20. Vovenko, E.P. and I.B. Sokolova, [*Oxygen tension in the brain cortex arterioles during spontaneous respiration with the hypoxic gas mixture in rats*]. Ross Fiziol Zh Im I M Sechenova, 1998. **84**(5-6): p. 527-35.
21. Sheth, S., et al., *Evaluation of coupling between optical intrinsic signals and neuronal activity in rat somatosensory cortex*. Neuroimage, 2003. **19**(3): p. 884-94.
22. Sheth, S.A., et al., *Spatiotemporal evolution of functional hemodynamic changes and their relationship to neuronal activity*. J Cereb Blood Flow Metab, 2005. **25**(7): p. 830-41.
23. Moon, C.H., et al., *Neural interpretation of blood oxygenation level-dependent fMRI maps at submillimeter columnar resolution*. J Neurosci, 2007. **27**(26): p. 6892-902.
24. Nemoto, M., et al., *Functional signal- and paradigm-dependent linear relationships between synaptic activity and hemodynamic responses in rat somatosensory cortex*. J Neurosci, 2004. **24**(15): p. 3850-61.
25. Vanzetta, I., et al., *Columnar resolution of blood volume and oximetry functional maps in the behaving monkey; implications for FMRI*. Neuron, 2004. **42**(5): p. 843-54.
26. Iadecola, C., *Neurovascular regulation in the normal brain and in Alzheimer's disease*. Nat Rev Neurosci, 2004. **5**(5): p. 347-60.
27. Peppiatt, C.M., et al., *Bidirectional control of CNS capillary diameter by pericytes*. Nature, 2006. **443**(7112): p. 700-4.
28. Krimer, L.S., et al., *Dopaminergic regulation of cerebral cortical microcirculation*. Nat Neurosci, 1998. **1**(4): p. 286-9.
29. Mathiesen, C., et al., *Modification of activity-dependent increases of cerebral blood flow by excitatory synaptic activity and spikes in rat cerebellar cortex*. J Physiol, 1998. **512** ( Pt 2): p. 555-66.
30. Berwick, J., et al., *Fine detail of neurovascular coupling revealed by spatiotemporal analysis of the hemodynamic response to single whisker stimulation in rat barrel cortex*. J Neurophysiol, 2008. **99**(2): p. 787-98.
31. Devor, A., et al., *Suppressed neuronal activity and concurrent arteriolar vasoconstriction may explain negative blood oxygenation level-dependent signal*. J Neurosci, 2007. **27**(16): p. 4452-9.

32. Devor, A., et al., *Coupling of the cortical hemodynamic response to cortical and thalamic neuronal activity*. Proc Natl Acad Sci U S A, 2005. **102**(10): p. 3822-7.
33. Hillman, E.M., et al., *Depth-resolved optical imaging and microscopy of vascular compartment dynamics during somatosensory stimulation*. Neuroimage, 2007. **35**(1): p. 89-104.
34. Mayhew, J.E., et al., *Cerebral vasomotion: a 0.1-Hz oscillation in reflected light imaging of neural activity*. Neuroimage, 1996. **4**(3 Pt 1): p. 183-93.
35. Frostig, R.D., et al., *Cortical functional architecture and local coupling between neuronal activity and the microcirculation revealed by in vivo high-resolution optical imaging of intrinsic signals*. Proc Natl Acad Sci U S A, 1990. **87**(16): p. 6082-6.
36. Malonek, D. and A. Grinvald, *Vascular regulation at sub millimeter range. Sources of intrinsic signals for high resolution optical imaging*. Adv Exp Med Biol, 1997. **413**: p. 215-20.
37. Buxton, R.B., *The elusive initial dip*. Neuroimage, 2001. **13**(6 Pt 1): p. 953-8.
38. Prahl, S., *Tabulated Molar Extinction Coefficient for Hemoglobin in Water*. 2008.
39. Vanzetta, I. and A. Grinvald, *Increased cortical oxidative metabolism due to sensory stimulation: implications for functional brain imaging*. Science, 1999. **286**(5444): p. 1555-8.
40. Vanzetta, I. and A. Grinvald, *Evidence and lack of evidence for the initial dip in the anesthetized rat: implications for human functional brain imaging*. Neuroimage, 2001. **13**(6 Pt 1): p. 959-67.
41. Chen, Y., W.S. Geisler, and E. Seidemann, *Optimal decoding of correlated neural population responses in the primate visual cortex*. Nat Neurosci, 2006. **9**(11): p. 1412-20.
42. Grinvald, A., et al., *Cortical point-spread function and long-range lateral interactions revealed by real-time optical imaging of macaque monkey primary visual cortex*. J Neurosci, 1994. **14**(5 Pt 1): p. 2545-68.
43. Drake, C.T. and C. Iadecola, *The role of neuronal signaling in controlling cerebral blood flow*. Brain Lang, 2007. **102**(2): p. 141-52.
44. Yoshioka, T., et al., *Relation between patterns of intrinsic lateral connectivity, ocular dominance, and cytochrome oxidase-reactive regions in macaque monkey striate cortex*. Cereb Cortex, 1996. **6**(2): p. 297-310.
45. Ogawa, S., et al., *Brain magnetic resonance imaging with contrast dependent on blood oxygenation*. Proc Natl Acad Sci U S A, 1990. **87**(24): p. 9868-72.
46. Chen-Bee, C.H., et al., *The triphasic intrinsic signal: implications for functional imaging*. J Neurosci, 2007. **27**(17): p. 4572-86.
47. Buxton, R.B., E.C. Wong, and L.R. Frank, *Dynamics of blood flow and oxygenation changes during brain activation: the balloon model*. Magn Reson Med, 1998. **39**(6): p. 855-64.

48. Frahm, J., et al., *The post-stimulation undershoot in BOLD fMRI of human brain is not caused by elevated cerebral blood volume*. Neuroimage, 2008. **40**(2): p. 473-81.
49. Fagrell, B., M. Intaglietta, and J. Ostergren, *Relative hematocrit in human skin capillaries and its relation to capillary blood flow velocity*. Microvasc Res, 1980. **20**(3): p. 327-35.
50. Matsuda, K., Nagami, T., Kawano, K., Yamame, S., *A new system for measuring eye position on a personal computer.*, in Society for Neuroscience. 2000, Society for Neuroscience, Washington DC.: New Orleans.
51. Arieli, A., A. Grinvald, and H. Slovin, *Dural substitute for long-term imaging of cortical activity in behaving monkeys and its clinical implications*. J Neurosci Methods, 2002. **114**(2): p. 119-33.
52. Kalatsky, V.A. and M.P. Stryker, *New paradigm for optical imaging: temporally encoded maps of intrinsic signal*. Neuron, 2003. **38**(4): p. 529-45.
53. Ratzlaff, E.H. and A. Grinvald, *A tandem-lens epifluorescence microscope: hundred-fold brightness advantage for wide-field imaging*. J Neurosci Methods, 1991. **36**(2-3): p. 127-37.
54. Logothetis, N.K., et al., *Neurophysiological investigation of the basis of the fMRI signal*. Nature, 2001. **412**(6843): p. 150-7.
55. Shulman, R.G., et al., *Energetic basis of brain activity: implications for neuroimaging*. Trends Neurosci, 2004. **27**(8): p. 489-95.
56. Ugurbil, K., L. Toth, and D.S. Kim, *How accurate is magnetic resonance imaging of brain function?* Trends Neurosci, 2003. **26**(2): p. 108-14.
57. Devor, A., et al., *Coupling of total hemoglobin concentration, oxygenation, and neural activity in rat somatosensory cortex*. Neuron, 2003. **39**(2): p. 353-9.
58. Ogawa, S., et al., *Intrinsic signal changes accompanying sensory stimulation: functional brain mapping with magnetic resonance imaging*. Proc Natl Acad Sci U S A, 1992. **89**(13): p. 5951-5.
59. Grinvald, A., et al., *Functional architecture of cortex revealed by optical imaging of intrinsic signals*. Nature, 1986. **324**(6095): p. 361-4.
60. Kim, D.S., T.Q. Duong, and S.G. Kim, *High-resolution mapping of iso-orientation columns by fMRI*. Nat Neurosci, 2000. **3**(2): p. 164-9.
61. Beatty, J., *Task-evoked pupillary responses, processing load, and the structure of processing resources*. Psychol Bull, 1982. **91**(2): p. 276-92.
62. Niessing, J., et al., *Hemodynamic signals correlate tightly with synchronized gamma oscillations*. Science, 2005. **309**(5736): p. 948-51.
63. Hillman, E.M., *Optical brain imaging in vivo: techniques and applications from animal to man*. J Biomed Opt, 2007. **12**(5): p. 051402.
64. Kohl, M., et al., *Physical model for the spectroscopic analysis of cortical intrinsic optical signals*. Phys Med Biol, 2000. **45**(12): p. 3749-64.
65. Rajkai, C., et al., *Transient cortical excitation at the onset of visual fixation*. Cereb Cortex, 2008. **18**(1): p. 200-9.

66. Attwell, D. and C. Iadecola, *The neural basis of functional brain imaging signals*. Trends Neurosci, 2002. **25**(12): p. 621-5.
67. Moore, C.I. and R. Cao, *The hemo-neural hypothesis: on the role of blood flow in information processing*. J Neurophysiol, 2008. **99**(5): p. 2035-47.
68. Jack, A.I., et al., *Separate modulations of human V1 associated with spatial attention and task structure*. Neuron, 2006. **51**(1): p. 135-47.
69. Kastner, S., et al., *Topographic maps in human frontal cortex revealed in memory-guided saccade and spatial working-memory tasks*. J Neurophysiol, 2007. **97**(5): p. 3494-507.
70. Ress, D., B.T. Backus, and D.J. Heeger, *Activity in primary visual cortex predicts performance in a visual detection task*. Nat Neurosci, 2000. **3**(9): p. 940-5.
71. Silver, M.A., D. Ress, and D.J. Heeger, *Neural correlates of sustained spatial attention in human early visual cortex*. J Neurophysiol, 2007. **97**(1): p. 229-37.
72. Luck, S.J., et al., *Neural mechanisms of spatial selective attention in areas V1, V2, and V4 of macaque visual cortex*. J Neurophysiol, 1997. **77**(1): p. 24-42.
73. Fox, M.D., et al., *The human brain is intrinsically organized into dynamic, anticorrelated functional networks*. Proc Natl Acad Sci U S A, 2005. **102**(27): p. 9673-8.
74. Shuler, M.G. and M.F. Bear, *Reward timing in the primary visual cortex*. Science, 2006. **311**(5767): p. 1606-9.
75. Schwartz, G., et al., *Detection and prediction of periodic patterns by the retina*. Nat Neurosci, 2007. **10**(5): p. 552-4.
76. Treisman, M., *Temporal discrimination and the indifference interval. Implications for a model of the "internal clock"*. Psychol Monogr, 1963. **77**(13): p. 1-31.
77. Burr, D., A. Tozzi, and M.C. Morrone, *Neural mechanisms for timing visual events are spatially selective in real-world coordinates*. Nat Neurosci, 2007. **10**(4): p. 423-5.
78. Janssen, P. and M.N. Shadlen, *A representation of the hazard rate of elapsed time in macaque area LIP*. Nat Neurosci, 2005. **8**(2): p. 234-41.
79. Mauk, M.D. and D.V. Buonomano, *The neural basis of temporal processing*. Annu Rev Neurosci, 2004. **27**: p. 307-40.
80. Rao, S.M., A.R. Mayer, and D.L. Harrington, *The evolution of brain activation during temporal processing*. Nat Neurosci, 2001. **4**(3): p. 317-23.
81. Brody, C.D., et al., *Timing and neural encoding of somatosensory parametric working memory in macaque prefrontal cortex*. Cereb Cortex, 2003. **13**(11): p. 1196-207.
82. Sato, A., Y. Sato, and S. Uchida, *Activation of the intracerebral cholinergic nerve fibers originating in the basal forebrain increases regional cerebral blood flow in the rat's cortex and hippocampus*. Neurosci Lett, 2004. **361**(1-3): p. 90-3.

83. Pardridge, W.M., *Neuropeptides and the blood-brain barrier*. *Annu Rev Physiol*, 1983. **45**: p. 73-82.
84. Berridge, C.W. and B.D. Waterhouse, *The locus coeruleus-noradrenergic system: modulation of behavioral state and state-dependent cognitive processes*. *Brain Res Brain Res Rev*, 2003. **42**(1): p. 33-84.
85. Ruff, C.C. and J. Driver, *Attentional preparation for a lateralized visual distractor: behavioral and fMRI evidence*. *J Cogn Neurosci*, 2006. **18**(4): p. 522-38.
86. Meister, M. and T. Bonhoeffer, *Tuning and topography in an odor map on the rat olfactory bulb*. *J Neurosci*, 2001. **21**(4): p. 1351-60.
87. Shoham, D. and A. Grinvald, *The cortical representation of the hand in macaque and human area S-I: high resolution optical imaging*. *J Neurosci*, 2001. **21**(17): p. 6820-35.
88. Versnel, H., et al., *Optical imaging of intrinsic signals in ferret auditory cortex: responses to narrowband sound stimuli*. *J Neurophysiol*, 2002. **88**(3): p. 1545-58.
89. Mitra, P.P., et al., *The nature of spatiotemporal changes in cerebral hemodynamics as manifested in functional magnetic resonance imaging*. *Magn Reson Med*, 1997. **37**(4): p. 511-8.
90. Filosa, J.A., et al., *Local potassium signaling couples neuronal activity to vasodilation in the brain*. *Nat Neurosci*, 2006. **9**(11): p. 1397-1403.
91. Kleinfeld, D., et al., *Fluctuations and stimulus-induced changes in blood flow observed in individual capillaries in layers 2 through 4 of rat neocortex*. *Proc Natl Acad Sci U S A*, 1998. **95**(26): p. 15741-6.
92. Norup Nielsen, A. and M. Lauritzen, *Coupling and uncoupling of activity-dependent increases of neuronal activity and blood flow in rat somatosensory cortex*. *J Physiol*, 2001. **533**(Pt 3): p. 773-85.
93. Das, A. and C.D. Gilbert, *Long-range horizontal connections and their role in cortical reorganization revealed by optical recording of cat primary visual cortex*. *Nature*, 1995. **375**(6534): p. 780-4.
94. Saarinen, J., D.M. Levi, and B. Shen, *Integration of local pattern elements into a global shape in human vision*. *Proc Natl Acad Sci U S A*, 1997. **94**(15): p. 8267-71.
95. Kovacs, I. and B. Julesz, *A closed curve is much more than an incomplete one: effect of closure in figure-ground segmentation*. *Proc Natl Acad Sci U S A*, 1993. **90**(16): p. 7495-7.
96. Saarinen, J. and D.M. Levi, *Integration of local features into a global shape*. *Vision Res*, 2001. **41**(14): p. 1785-90.
97. Geisler, W.S., *Visual Perception and the Statistical Properties of Natural Scenes*. *Annu Rev Psychol*, 2007.
98. Polat, U. and D. Sagi, *Lateral interactions between spatial channels: suppression and facilitation revealed by lateral masking experiments*. *Vision Res*, 1993. **33**(7): p. 993-9.

99. Polat, U. and D. Sagi, *The architecture of perceptual spatial interactions*. Vision Res, 1994. **34**(1): p. 73-8.
100. Kapadia, M.K., et al., *Improvement in visual sensitivity by changes in local context: parallel studies in human observers and in V1 of alert monkeys*. Neuron, 1995. **15**(4): p. 843-56.
101. Field, D.J., A. Hayes, and R.F. Hess, *Contour integration by the human visual system: evidence for a local "association field"*. Vision Res, 1993. **33**(2): p. 173-93.
102. Wertheimer, M., *Laws of Organization in Perceptual Forms*. 1938, London: Harcourt, Brace and Jovanovich.
103. Hess, R. and D. Field, *Integration of contours: new insights*. Trends Cogn Sci, 1999. **3**(12): p. 480-486.
104. Peters, R.J., et al., *Components of bottom-up gaze allocation in natural images*. Vision Res, 2005. **45**(18): p. 2397-416.
105. Mandon, S. and A.K. Kreiter, *Rapid contour integration in macaque monkeys*. Vision Res, 2005. **45**(3): p. 291-300.
106. Yen, S.C. and L.H. Finkel, *Extraction of perceptually salient contours by striate cortical networks*. Vision Res, 1998. **38**(5): p. 719-41.
107. Bosking, W.H., et al., *Orientation selectivity and the arrangement of horizontal connections in tree shrew striate cortex*. J Neurosci, 1997. **17**(6): p. 2112-27.
108. Gilbert, C.D. and T.N. Wiesel, *Columnar specificity of intrinsic horizontal and corticocortical connections in cat visual cortex*. J Neurosci, 1989. **9**(7): p. 2432-42.
109. Rockland, K.S., J.S. Lund, and A.L. Humphrey, *Anatomical binding of intrinsic connections in striate cortex of tree shrews (Tupaia glis)*. J Comp Neurol, 1982. **209**(1): p. 41-58.
110. Schmidt, K.E., et al., *The perceptual grouping criterion of colinearity is reflected by anisotropies of connections in the primary visual cortex*. Eur J Neurosci, 1997. **9**(5): p. 1083-9.
111. Sincich, L.C. and G.G. Blasdel, *Oriented axon projections in primary visual cortex of the monkey*. J Neurosci, 2001. **21**(12): p. 4416-26.
112. Fitzpatrick, D., *The functional organization of local circuits in visual cortex: insights from the study of tree shrew striate cortex*. Cereb Cortex, 1996. **6**(3): p. 329-41.
113. Li, Z., *A neural model of contour integration in the primary visual cortex*. Neural Comput, 1998. **10**(4): p. 903-40.
114. Das, A. and C.D. Gilbert, *Topography of contextual modulations mediated by short-range interactions in primary visual cortex*. Nature, 1999. **399**(6737): p. 655-61.
115. Polat, U., et al., *Collinear stimuli regulate visual responses depending on cell's contrast threshold*. Nature, 1998. **391**(6667): p. 580-4.

116. Crook, J.M., R. Engelmann, and S. Lowel, *GABA-inactivation attenuates colinear facilitation in cat primary visual cortex*. *Exp Brain Res*, 2002. **143**(3): p. 295-302.
117. Polat, U. and D. Sagi, *The relationship between the subjective and objective aspects of visual filling-in*. *Vision Res*, 2007. **47**(18): p. 2473-81.
118. Peterhans, E. and R. von der Heydt, *Mechanisms of contour perception in monkey visual cortex. II. Contours bridging gaps*. *J Neurosci*, 1989. **9**(5): p. 1749-63.
119. Chisum, H.J., F. Mooser, and D. Fitzpatrick, *Emergent properties of layer 2/3 neurons reflect the collinear arrangement of horizontal connections in tree shrew visual cortex*. *J Neurosci*, 2003. **23**(7): p. 2947-60.
120. Giorgi, R.G., et al., *Facilitation of contrast detection in near-peripheral vision*. *Vision Res*, 2004. **44**(27): p. 3193-202.
121. Shani, R. and D. Sagi, *Eccentricity effects on lateral interactions*. *Vision Res*, 2005. **45**(15): p. 2009-24.
122. Toth, L.J., et al., *Subthreshold facilitation and suppression in primary visual cortex revealed by intrinsic signal imaging*. *Proc Natl Acad Sci U S A*, 1996. **93**(18): p. 9869-74.
123. Angelucci, A., et al., *Circuits for local and global signal integration in primary visual cortex*. *J Neurosci*, 2002. **22**(19): p. 8633-46.
124. Shmuel, A., et al., *Retinotopic axis specificity and selective clustering of feedback projections from V2 to V1 in the owl monkey*. *J Neurosci*, 2005. **25**(8): p. 2117-31.
125. Stettler, D.D., et al., *Lateral connectivity and contextual interactions in macaque primary visual cortex*. *Neuron*, 2002. **36**(4): p. 739-50.
126. Tootell, R.B., et al., *Functional anatomy of macaque striate cortex. V. Spatial frequency*. *J Neurosci*, 1988. **8**(5): p. 1610-24.
127. Li, W., V. Piech, and C.D. Gilbert, *Contour saliency in primary visual cortex*. *Neuron*, 2006. **50**(6): p. 951-62.
128. Sigman, M., et al., *Top-down reorganization of activity in the visual pathway after learning a shape identification task*. *Neuron*, 2005. **46**(5): p. 823-35.
129. Bauer, R. and S. Heinze, *Contour integration in striate cortex. Classic cell responses or cooperative selection?* *Exp Brain Res*, 2002. **147**(2): p. 145-52.
130. Li, W., V. Piech, and C.D. Gilbert, *Perceptual learning and top-down influences in primary visual cortex*. *Nat Neurosci*, 2004. **7**(6): p. 651-7.
131. Freeman, E., et al., *Top-down modulation of lateral interactions in early vision: does attention affect integration of the whole or just perception of the parts?* *Curr Biol*, 2003. **13**(11): p. 985-9.
132. Ringach, D.L. and R. Shapley, *Spatial and temporal properties of illusory contours and amodal boundary completion*. *Vision Res*, 1996. **36**(19): p. 3037-50.
133. Lamme, V.A., *The neurophysiology of figure-ground segregation in primary visual cortex*. *J Neurosci*, 1995. **15**(2): p. 1605-15.

134. Logothetis, N.K., *What we can do and what we cannot do with fMRI*. *Nature*, 2008. **453**(7197): p. 869-78.
135. Gardner, J.L., et al., *High spatial resolution fMRI reveals orientation specific responses in large draining veins.*, in *Gordon Research Conference: Brain Energy Metabolism and Blood Flow*. 2006: Magdalen College, Oxford UK.
136. Köhler, W., *Gestalt psychology: An introduction to new concepts in modern psychology*. 1992, New York: Liveright. 369.
137. Mizobe, K., et al., *Facilitation and suppression of single striate-cell activity by spatially discrete pattern stimuli presented beyond the receptive field*. *Vis Neurosci*, 2001. **18**(3): p. 377-91.
138. Roelfsema, P.R., V.A. Lamme, and H. Spekreijse, *Object-based attention in the primary visual cortex of the macaque monkey*. *Nature*, 1998. **395**(6700): p. 376-81.
139. Mendola, J.D., et al., *fMRI Measures of perceptual filling-in in the human visual cortex*. *J Cogn Neurosci*, 2006. **18**(3): p. 363-75.
140. Meng, M., D.A. Remus, and F. Tong, *Filling-in of visual phantoms in the human brain*. *Nat Neurosci*, 2005. **8**(9): p. 1248-54.